2019

Neuronal population and network analysis tools for large-scale calcium imaging datasets

https://hdl.handle.net/2144/36160

Boston University

BOSTON UNIVERSITY

COLLEGE OF ENGINEERING

Dissertation

NEURONAL POPULATION AND NETWORK ANALYSIS TOOLS FOR LARGE-SCALE CALCIUM IMAGING DATASETS

by

KYLE ROLLINS HANSEN

B.S., University of Utah, 2014
M.S., Boston University, 2017

Submitted in partial fulfillment of the

requirements for the degree of

Doctor of Philosophy

2019

Approved by

First Reader
Xue Han, Ph.D.
Associate Professor of Biomedical Engineering

Second Reader
Bobak Nazer, Ph.D.
Associate Professor of Electrical and Computer Engineering
Associate Professor of Systems Engineering

Third Reader
David A. Boas, Ph.D.
Professor of Biomedical Engineering
Professor of Electrical and Computer Engineering

Fourth Reader
Michael E. Hasselmo, D.Phil.
Professor of Psychological and Brain Sciences

Fifth Reader
John A. White, Ph.D.
Professor and Chair of Biomedical Engineering

“Progress is made by trial and failure;

the failures are generally a hundred times more numerous than the successes;

yet they are usually left unchronicled”

- *Sir William Ramsay*

DEDICATION

I dedicate this work to my wife Kennedy, and my sons Christian, Thomas and Oliver –

Your love, support, and excitement for life helped me enjoy this process.

ACKNOWLEDGMENTS

I would like to thank my Heavenly Father for my health, blessings, and opportunities that have enabled me to learn and grow to be able to do this work. I am extremely grateful for my wife, Kennedy Hansen, and thank her for her constant love, support, and sacrifices that have made graduate school possible for me. I love her more than anything, and could not have completed this work without the mental and emotional support she continually provided. I'd like to thank my sons, Christian, Thomas, and Oliver who have made coming home from the lab a joy every day and reminded me that "scientists make mistakes." I'm grateful for my parents, Wayne and Trudy Hansen, and want to thank them for teaching me that I can accomplish anything I set my mind to and have enabled me to pursue my interests throughout my life, even if that means taking their grandkids across the country for graduate school. I'm grateful for my sisters Erika, Alyssa, and Amanda and want to thank them for helping me grow as an individual throughout my life and teaching me I don't have all the answers. I also want to thank my in-laws, Pat and Suzan Gerber for their support of both myself and my family during the process of graduate school. I'd also like to thank the many individuals I've been able to serve with in the Church of Jesus Christ of Latter Day Saints, both throughout my life and in Boston specifically, as their varied perspectives, insights, and mentorship has greatly influenced my way of thinking and approach to problem solving.

There have been many teachers throughout my life that have helped me develop into a scientist. I'd like to thank Ms. Peggy Hyde and Ms. Linda Porter, who in 4th and 5th grade helped me fall in love with neuroscience by handling sheep brains and gave me

additional math work that encouraged me to become a self-taught learner. I'm grateful for both Ms. Susan Callister and Ms. Nancee Ott for pressuring me to take AP Chemistry, even though I'd already written off chemistry and biology as interesting fields for a career. I'd like to thank Dr. David Shprecher and Dr. Richard King for giving me my first taste of research and helping me see how translational research works best when designed with the patient in mind. I'm extremely grateful for Dr. Robert Hitchcock, and want to thank him for being the first to encourage me to consider how pursuing a Ph.D. would help me accomplish my career goals. I'd also like to thank Dr. Matt Wachowiak and Dr. Michael Economo for helping me learn the day-to-day efforts that produce quality science while working with them to help publish my first scientific papers.

I am grateful for and would like to thank the many members of the Han Lab I have worked with during graduate school (in no particular order): Richie Kohman, Krishnakanth Kondubolu, Ali Mohammed, Nicholas James, Angela Nocera, Hua-an Tseng, Howard Gritton, Marianna Keaveney, Mark Bucklin, Susie Cha, Seth Bensussen, Mike Romano, Dana Zemel, Sanaya Shroff, Andrew Martin, Rebecca Mount, Robb Kessel, Moona Abdulkerim, Dyllon Carlson, and Tiffany Wu. You have each helped me in many ways, ranging from learning to clone DNA, helping me build microscopes and custom computers, performing animal surgeries and histology, providing feedback on writing and presenting my research, and helping me enjoy the scientific rigor working in the lab. Thank you to my collaborators in other laboratories, including Gloria DeWalt and Dr. William Eldred. Additionally, I'd like to thank the other students in my graduate school cohort for their friendship and discussions during this process.

I would like to thank the Boston University Department of Biomedical Engineering faculty and administrative staff for what I have learned in classes and for the guidance they've provided in navigating graduate school. I would also like to thank the sources of support that have made this work possible, including the National Institutes of Health (NIH) Training Program in Quantitative Biology & Physiology at BU (5T32GM008764-17), a National Science Foundation Graduate Research Fellowship under Grant No. DGE-1247312, and an NIH F31 Fellowship from the National Institute of Neurological Disorders and Stroke (1F31NS105420-01). I would like to thank Dr. Venkatesh Saligrama who was a co-sponsor for my F31 fellowship and provided guidance on that work. I also want to thank Dr. John White, Dr. David Boas, and Dr. Michael Hasselmo for serving on my dissertation committee and providing feedback throughout the process. I'd like thank Dr. Bobak Nazer who was my co-advisor for the computational and network side of my thesis work and helped me have confidence in the quality of my work. Lastly, I'd especially like to thank Dr. Xue Han as my primary research advisor and mentor for teaching me so much about science, writing, communication, and continually finding joy and excitement while conducting high-quality research.

NEURONAL POPULATION AND NETWORK ANALYSIS TOOLS FOR LARGE-SCALE CALCIUM IMAGING DATASETS

KYLE ROLLINS HANSEN

Boston University College of Engineering, 2019

Major Professor: Xue Han, Ph.D., Associate Professor of Biomedical Engineering

ABSTRACT

Recently developed large scale calcium imaging techniques allow functional analysis of hundreds to thousands of simultaneously recorded individual neurons, resulting in exceedingly large datasets. Conventional analysis methods are not scalable for large imaging datasets collected at high speed and high pixel resolution. The efforts described in this dissertation focus on the development of analysis methods designed for large datasets, along with the application of these analytic methods to derive novel conceptual insights into how neuronal circuits function in both healthy and diseased brains.

First, an image processing pipeline and a segmentation toolbox were developed and shared as an open-source software. The processing pipeline is a parallelized version of a recently published motion correction algorithm, but which improved processing speed by 10%. The segmentation toolbox is semi-automated and provides high confidence in the spatial extent of segmented cells, with the option to integrate temporal information for the segmentation.

Next, these and additionally developed methods were used to study the effect of mild traumatic brain injury (mTBI) on neuronal circuits over consecutive days. Using a newly developed signal normalization technique, we found that immediately following a blast injury event, neurons exhibited two types of changes in intracellular calcium dynamics at different time scales. One was a reduction in basal intracellular calcium levels on a time scale of minutes. The second was a reduction in the rate of transient calcium fluctuations at the sub-second time scale. Both changes recovered one hour post blast injury, suggesting different types of neuronal damage from mTBI.

Lastly, we developed a method that allowed us to observe network differences on a trial-by-trial basis with a limited number of data points. We utilized these analysis tools to study hippocampal network responses during two learning processes, trace conditioning and extinction learning. We found a similar pattern of neuronal dynamics for both learning processes, however the single-neuron identities for each process was unique.

Overall, this dissertation describes a set of image processing, segmentation, and network analysis tools for large scale calcium imaging datasets, which were applied to analyze network changes during learning and externally induced by mTBI.

TABLE OF CONTENTS

LIST OF FIGURES

LIST OF ABBREVIATIONS

AAV9	adeno-associated virus serotype 9
AChR	acetylcholine receptors
AMPA	α-amino-3-hydroxy-5-methyl-4-isoxazolepropionic acid
AP	anterior-posterior
approx	approximately
A.U.	arbitrary units
Ca/Ca^{2+}	calcium
CA1/CA3	Cornu Ammonis area 1/Cornu Ammonis area 3
CMOS/sCMOS	(scientific) complementary metal-oxide-semiconductor
cm	centimeter
COBIA	cranium only blast injury apparatus
CR	conditioned response
CS	conditioned stimulus
DAPI	nuclear DNA stain: 4’,6-Diamidino-2-Phenylindole
DV	dorsoventral
EEG	electroencephalography
EX	extinction
fMRI	functional magnetic resonance imaging
fNIRS	functional near-infrared spectroscopy
GABA	gamma-aminobutyric acid
GB	gigabyte

GCaMP/GCaMP6f	calcium sensor: GFP, calmodulin, M13 peptide (6-fast)
GFAP	glial fibrillary acidic protein
Glu/GluR	glutamate (receptor)
GPU	graphics processing unit
h/hr	hour
H.M.	Henry Molaison
Hz/kHz	(kilo)Hertz
Iba1	ionized calcium-binding adapter molecule 1
ID	inner diameter
I/O	input/output
IR	infrared
ISODATA	iterative self-organizing data analysis technique
LED	light emitting diode
M	Molar
MEG	magnetoencephalography
min	minute
µm	micrometer/micron
ML	mediolateral
mm	millimeter
msec/ms	millisecond
nL/nl	nanoliter
NMDA	N-methyl-D-aspartic acid

OD	outer diameter
Pa/kPa	(kilo)Pascal
PB	phosphate buffer
PBTx	phosphate buffer containing 0.3% TritonX 100
PCA	principal component analysis
PDE	probability density estimate
pERK	phosphorylated extracellular signal-regulated kinase
ptmc	Python tiff motion correction
PFC	prefrontal cortex
psi	pounds per square inch
PTSD	post-traumatic stress disorder
RGB	red green blue
ROI(s)	Region(s) of Interest
SD/s.d.	standard deviation
sec	second
SM	stratum moleculare
SO	stratum oriens
SP	stratum pyramidale
SV40	simian vacuolating virus 40
Syn	synapsin
TB	terabyte
TBI/mTBI	(mild) traumatic brain injury

TTL	transistor-transistor logic
US	unconditioned stimulus
USB	universal serial bus
UV	ultraviolet
WPRE	woodchuck hepatitis virus posttranscriptional regulatory element sequence

CHAPTER 1 – INTRODUCTION

The brain is a complex organ, driving the somatic and autonomic processes that enable healthy bodies to function, in addition to providing each individual with a sense of selfhood. However, there is still much to be learned about how the brain carries out its diverse and important functions. Understanding brain function in both health and disease is increasingly important as both the financial and societal burden of neurological disorders continues to grow in the United States and throughout the world [1]–[3]. For both healthy and diseased brains, neurons are fundamental functional units of communication within the brain and communicate using a variety of electrical and chemical signals [4]. These signals differentially impact how the brain functions across both spatial and temporal scales. To understand and integrate the data at these different scales, robust and scalable analysis methods are required. The work of this dissertation is to develop analysis methods for large scale calcium imaging data, a powerful optical microscopy technique that provides single-cell resolution across millimeters of tissue while concurrently monitoring hundreds to thousands of neurons simultaneously in awake, behaving animals.

1.1 The Brain as a Network

Our current understanding about brain function suggests that the neurons function as networks across multiple spatial scales, from the macro- (whole brain) to micro- (single cell) scales. Information about network function needs to be integrated across these spatial scales to effectively understand brain function and treat neurological diseases.

Microscale anatomical study of the brain began in the late 19th century with the use of Golgi staining by Ramon y Cajal [5] to observe the intricate processes of individual neurons and their spatial relationship to one another (Figure 1A). These early studies focused on how the anatomy of neurons form networks with their axons and dendrites, and subsequent anatomical studies have shown how wide-spread these networks can reach throughout the brain on a single-cell level [6], [7]. In addition to these methods for studying the anatomical networks in the brain, techniques have been developed to study the functional neuronal network behavior that rely on these microscale anatomical connections. These functional network measurements include patch clamping [8], [9], multichannel electrode arrays [10]–[12], local field potentials [13]–[15], and voltage [16], [17] and calcium imaging [18]–[20], all of which can be utilized in cell cultures, brain slices, or living animals. These techniques provide measurements of functional brain networks at a spatial resolution of single cells, on a scale ranging from microns to millimeters while simultaneously recording tens to thousands of cells.

Macroscale study of brain regions also began in the late 19th century while being pioneered by anatomists. Scientists such as Paul Broca showed that specific aphasias were linked to lesions in a localized part of the brain [21] which is now known as Broca's area. Similarly, Carl Wernicke showed there was a localized spatial constraint for another type of aphasia in an area of cortex now known as Wernicke's area [22], while his advisor Theodor Meynert also made important contributions to the concept of functionally localized brain regions at a macroscale [23]. These studies lead to Korbinian Brodmann defining the Brodmann areas of the brain [24], 52 brain areas grouped into 11 histological areas that are still covered in neuroanatomy books today [4]. Similar to the evolution of the microscale study of the brain, modern techniques now also include functional read-outs to study how whole brain regions interact in different contexts. These techniques include electroencephalography (EEG) [10], [25], [26] and magnetoencephalography (MEG) [25], [26], which record the electric fields or magnetic fields respectively that rise from the electrical dipoles that arise from bulk brain activity in a specific region. Additional techniques such as functional near-infrared spectroscopy (fNIRS) [27]–[29], and functional magnetic resonance imaging (fMRI) [30], [31] measure blood flow to different brain regions in different contexts, which is tied to the functional activity of neurons in that area. Ultimately, all of these methods provide functional brain readouts that allow for studies of networks with spatial resolution at the brain region level, on the order of cubic millimeters (Figure 1B).

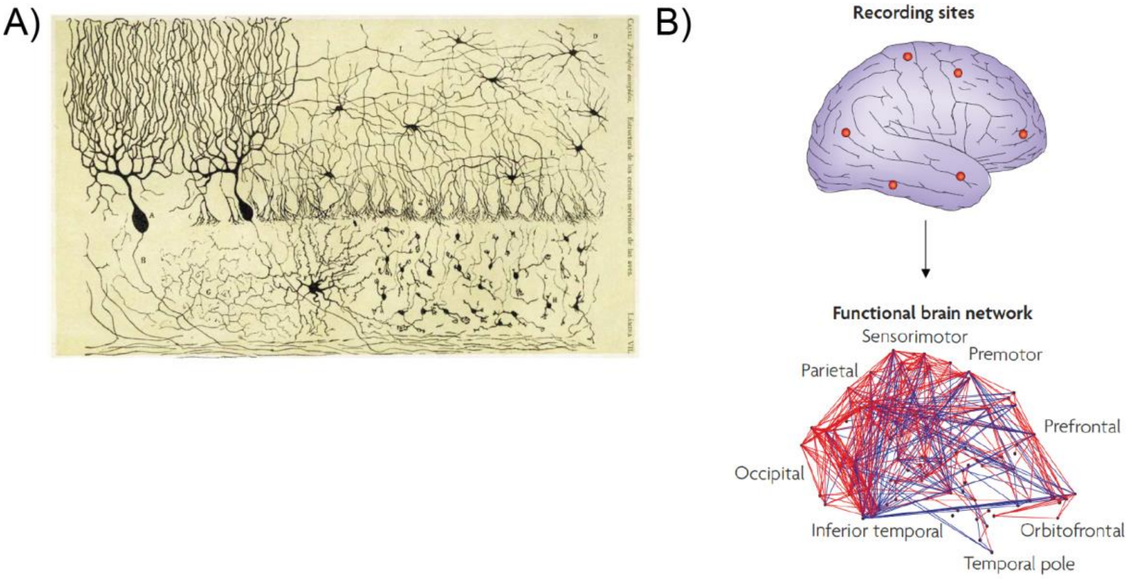

Figure 1. Microscale and Macroscale Networks in the Brain

(A) The intricate details of neuronal processes highlight the network structure of cells at the microscale as seen in this drawing of neurons in a chick cerebellum from Ramon y Cajal's publication in 1905. Image from [5]. **(B)** Schematic of the functional macroscale network generated from EEG data. Pairwise associations of nodes are used to draw edges between brain regions within the network. Image from [25].

Network analysis is commonly performed for both the macro- and micro-scales of the brain, though each scale is typically studied in isolation. At the macro-scale, nodes of the network often correspond to brain regions [25]–[27], [29]–[31], while individual neurons or small groups of neurons typically represent network nodes at the microscale [18], [32]. In recent years, wide-field calcium imaging methods allow us to record the functional output of 100s to 1000s of individual neurons simultaneously in awake, behaving animals [20] (see "1.4 Analysis Tools for Large Scale Neuronal Calcium Imaging"). Data collection at this scale has the potential to bridge our understanding of brain networks between the micro- and macro- scales by providing single-cell resolution in millimeters of brain tissue, theoretically allowing the recording of all the nodes of a network at the micro-scale while measuring a single node of the macro-scale network.

1.2 The Hippocampus

The hippocampus is a sub-cortical brain region that is critical for learning and memory formation. The classical example of how the hippocampus is tied to learning and memory was a man named Henry Molaison, commonly known as H.M. in the research literature. In 1953, the surgeon William Scoville removed H.M.'s hippocampus as a treatment for epilepsy. While the surgery helped treat the epilepsy, it resulted in "a very grave, recent memory loss" immediately after the surgery [33] with an inability to learn new tasks as "once he had turned to a new task the nature of the preceding one could no longer be recalled." [34] Additionally, a large body of research has shown that hippocampal atrophy is related to many diseases related to memory loss and difficulty learning, such as Alzheimer's disease, various dementias, and Parkinson's disease when connected to mild cognitive impairment [35]–[39]. For this dissertation, the hippocampus is the primary brain region of study because of its role in traumatic brain injury (TBI) and for learning and memory.

Blast-induced TBI is an important public health concern, especially in military settings [40], [41], and is tied to pathologies of the hippocampus. Blast related injuries are connected with an increased likelihood of developing seizures [42], as well as memory and learning deficits [43], both of which are known to be related to hippocampal function [44], [45]. Additionally, blast injuries lead to various anatomical and structural changes, a loss of inhibitory interneurons, and a reduction of long-term potentiation within the hippocampus [46]–[48]. These pathologies have been reported across many regions of the hippocampus, including Cornu Ammonis 1 (CA1), the primary anatomical focus of this work.

The hippocampus also plays an important role in two specific types of learning: trace conditioning and extinction learning. Trace conditioning is a specific learning process that has been shown to be dependent on the hippocampus [49]–[51]. For trace conditioned learning, an association is learned between a conditioned stimulus (CS) and an unconditioned stimulus (US) that are separated by a very short time period, called a trace interval. For animal studies, this takes the common form of trace eye-blink conditioning, where a tone is played as the CS, followed by a short trace interval a few hundred milliseconds long, followed by a puff of air to the animal's eye as the US [20], [50], [51]. Over time, animals will learn to associate the tone with the puff [52]–[56]. Extinction learning is the process of learning that a specific CS is no longer associated with the US to which it was previously connected. In the case of eye-blink trace conditioning, the puff can be removed and animals will learn that a specific tone is no longer connected to receiving a puff. Previous studies have shown that lesioning CA1 in the hippocampus alters the ability for animals to learn in the extinction context [50], [57]. This dissertation contains a study of the dynamic role of the hippocampus in each of these learning contexts.

Because the hippocampus is a local brain region tied to specific brain functions in certain contexts, it makes it an attractive area to understand how the single cell function in a micro-network relates to the function of a single node of the macro-network. Additionally, the cells in CA1 of the hippocampus are arranged in a monolayer, which is a beneficial anatomical feature for single-photon calcium imaging at high resolution (see “1.4 Analysis Tools for Large Scale Neuronal Calcium Imaging).

1.3 Neuroscience in the Age of Big Data and Open Science

Neuroscience has been thrust into the age of big data. One of the priority research areas established by the United States BRAIN Initiative [58] is “developing and applying improved methods for large-scale monitoring of neural activity.” As this work is currently underway with many new technologies and techniques being developed to record more and more neurons simultaneously, the size of datasets in neuroscience is growing at a rapid pace. For example, one 20 minute recording of a calcium imaging dataset at 20 Hz in our laboratory takes up about 45 Gigabytes (GB) of data to store. For the trace conditioning learning task presented in Chapter 4 of this dissertation, animals were recorded for about 2 sessions per day, across 5 days, yielding about 450 GB of data for 1 mouse for 1 experiment. For this specific study, there are 5 mice that we used, yielding 2.25 Terabytes (TB) of data. After motion correcting the videos and taking into account storing both the original data and motion corrected files for further extraction and analysis, the storage for this experiment doubles to 4.5 TB from only a couple weeks of data collection. Spread across additional experiments and research personnel, it is no wonder that the Han Lab now requires close to 200 TB of storage to house the data from our experiments. With the development of newer methods such as voltage imaging [17], [59] to collect more data at a higher temporal resolution (1 kHz) or light sheet microscopy for neuronal volumetric imaging [60]–[62], storing and accessing large datasets has become the new normal for neuroscience.

For the field of neuroscience to move forward and keep up with these large datasets, open science is required for effective sharing of tools and techniques. This has previously been suggested by thought leaders in the field [62] and led to the development of cloud-based platforms for computational reproducibility, such as Code Ocean [63]. Unfortunately, due to the limitations of academic research funding as a platform for software maintenance, one of the primary frameworks developed to unify neuronal data analysis in a scalable and open manner [64] is no longer actively being maintained, nor are the open data repositories SpikeFinder [65] and NeuroFinder [66] for calcium deconvolution and calcium image segmentation. Nevertheless, the same principles of open science are crucial for the field of neuroscience to move forward in the age of big data.

The principles of open science and transparency with data, code and analyses are important and conscious design elements for the work of this dissertation. The tools and methods herein are all shared publicly as hosted by the Han Lab GitHub organization (github.com/HanLabBU). This has been established with the primary goal of helping neuroscience advance more quickly by enabling other researchers to use these tools in making their own discoveries.

1.4 Analysis Tools for Large Scale Neuronal Calcium Imaging

Calcium imaging is a tool with many attractive features that can bridge our understanding of neuronal function across scales. First, many cells can be recorded simultaneously while maintaining the spatial information and relationship between individual cells, enabling high-throughput recordings with single-cell resolution [20], [67]. This is a distinct advantage over electrode recording techniques, where precise spatial information at a single-cell level is not maintained. Recordings can be performed in awake, behaving animals, avoiding potential confounds related to how anesthesia impacts neuronal function [68]–[70]. Additionally, genetically encoded calcium sensors such as GCaMP6 [71], can be targeted to specific neuronal subtypes to give additional insight about how different types of neurons work together within a brain region [72]. These are all features that can help understand how many individual neurons within a network to give rise to the function of a brain region.

Large scale, wide-field calcium imaging has several distinct advantages and challenges when compared to other common microscopy modalities for calcium imaging. One of the most common techniques for calcium imaging is using a 2-photon microscope which is a scanning microscope method that greatly reduces scattering. However, the scanning nature of this method strongly couples the imaging speed to the extent of the field of view. Thus, if one wants to collect calcium imaging data at 20 Hz, which is close to the temporal resolution of GCaMP6f, spatial video recordings are typically limited to 256x256 or 512x512 pixels and tens to a few hundred cells at most simultaneously [67], [73]–[75]. Micro-endoscopes are another common method to record calcium imaging data, though their image size is also limited to this smaller field of view because the microscope hardware is mounted to the head of the animal [76]–[78]. In contrast, wide-field imaging can allow much larger fields of view to be recorded at high spatial (1024x1024 pixels) and temporal (20-100 Hz) resolutions. Working with over 1 million pixels per frame requires unique image processing and trace extraction methods when compared to the standard techniques developed for just over 260,000 pixels per frame [79]–[82]. Some of the analysis methods developed in this dissertation are aimed to address the challenge of having high resolution microscopy videos with high pixel counts in each frame.

After extracting temporal calcium traces, population and network analysis methods are required to interpret how the network behavior gives rise to brain function. Exciting computational methods using dimensionally reduction techniques have recently been developed to understand neuronal networks and have typically been applied to discrete spiking data [18], [83], [84]. Using these techniques, temporal traces of neuronal data are projected into an abstract dimensional space, allowing the observation of features that seem to be important for the network. While informative, such dimensionality techniques produce abstract features, which cannot be easily projected back to specific dynamic patterns or connections of individual neurons. Ideally, one would like to detect network features that are more directly related to individual neuronal functions. Thus, one design constraint for this dissertation was to develop analyses techniques to understand changes in neuronal networks that can be more directly connected to individual neuronal function in a very quantitative fashion, in hopes that results from these analyses will be more interpretable.

Additionally, while such dimensionally analysis techniques can extract abstract spiking features about a neuronal network, their adaptation to calcium imaging data is not straightforward. One solution to this concern has been to develop deconvolution algorithms to convert calcium traces into spiking traces [18], [79], [85] so that the same dimensionality reduction techniques can be used. However, the relationship between spiking and calcium dynamics is nonlinear, poorly understood, and it is unknown whether or not the calcium dynamics in all cell types follow spiking in the same manner. These additional concerns and manipulations of the calcium data increase the probability of introducing additional confounding factors into the network analyses.

The most direct manner to understand calcium imaging data is to analyze the calcium traces directly, as calcium imaging provides additional unique prospects for neuronal network analyses. While calcium signals indirectly relate to neuronal spiking activities [71], [74], [86], calcium dynamics have additional physiological roles in neurons beyond serving as a temporally filtered surrogate for spiking. For example, intracellular calcium dynamics are critically involved in network plasticity [87] and cell survival [88], [89].

With the remarkable sensitivity of calcium sensors, calcium imaging in neuronal networks is increasingly used communication within networks of neurons. To date, however, there have been no scalable computational analysis methods applied for calcium neuronal networks of hundreds to thousands of cells to understand how the inherent calcium signals behave at a network level. This dissertation describes efforts to develop such analysis methods.

CHAPTER 2 – MOTION CORRECTION PIPELINE AND IMAGE SEGMENTATION TOOLBOX DEVELOPED FOR LARGE SCALE CALCIUM IMAGING DATA

2.1 Abstract

Conventional analysis methods for calcium imaging data are designed for small scale 2-photon and microendoscope data. These methods are not scalable for large imaging datasets collected at high speed and high pixel resolution, which necessitates the development of additional tools for these methods. To this end, we developed a parallel motion correction pipeline and semi-automated segmentation toolbox to be shared as open-source software.

The processing pipeline developed is a parallelized version of a recently published motion correction algorithm, but which improved processing speed by 10%. This was accomplished by generating a single reference frame that could be sent out with each individual frame to be processed in parallel. This method is scalable for further parallelization in a cluster environment.

The segmentation toolbox is semi-automated and provides high confidence in the spatial extent of segmented cells. Additionally, users have the option to integrate temporal information for the segmentation using either pixel-wise cross-correlation or principal component analysis.

Together, these methods provide an important step for streamlining the preprocessing of large scale calcium imaging datasets, and enable other researchers to more effectively adopt this microscopy method.

2.2 Introduction

Preprocessing of calcium image data is a critical step prior to any successful analyses. The quality of the preprocessing will greatly impact what inferences can be drawn from the data and whether or not they are truly reflected in the data. The preprocessing steps for data analysis can also take an extensive amount of time. In light of these considerations, many efforts have been devised to both automate and speed up the preprocessing of calcium image data [79]–[82]. While these efforts have been shown to be effective for smaller scale 2-photon and microendoscope calcium imaging datasets, they either take an unrealistic amount of computational time or simply do not work on large scale calcium imaging datasets.

The primary reason these methods are ineffectual for large scale datasets is the number of pixels per video frame. Datasets from 2-photon and microendoscope microscopes tend to have anywhere from 65,636 to 262,144 pixels per frame (256x256 to 512x512 pixels), while the large scale wide-field calcium datasets contain 1,048,576 pixels per frame (1024x1024 pixels). This 4-16 fold increase in the number of pixels per frame causes an immense slowdown for any sort of pixel-wise comparisons or large tensor decompositions across the video. Additionally, 2-photon and microendoscope datasets are qualitatively different from large scale wide-field datasets, with 2-photon data having little to no background scattering, and microendoscope datasets having a very high level of scattering, with the large scale wide-field datasets falling somewhere in between. These challenges suggest that unique methods need to be developed to handle these large scale datasets.

Our lab had previously developed a preprocessing pipeline to efficiently handle these datasets for both motion correction and image segmentation [20]. While effective, it was designed with the intent to scale to real-time processing of data as it was being collected, which required processing the frames in serial fashion for motion correction. The automated segmentation developed in this pipeline was also performed in a serial manner with cellular regions of interest (ROIs) being merged across frames. After examining this framework with different design constraints, we decided to further develop these methods. First, we created a motion correction pipeline that processed the video frames in parallel, resulting in a 10% decrease in processing time over the serial method. Additionally, we created an image segmentation toolbox that functioned in a semi-automated fashion to allow the user a high level of confidence in the extent of their segmented cells. These tools provided a basis for the work in the remainder of this dissertation, as well as other published work [90].

2.3 Parallel Motion Correction Pipeline

Converting a serial processing code to a parallel processing code requires breaking the code into discrete steps that can be sent out to parallel processes or threads, computed individually, and then aggregated back together after each process is completed. For the previously developed motion correction method [20], each frame had the same process performed on it (Figure 2). First, a frame was spatially median filtered, with a filter size of 3 pixels to decrease pixel noise. Next, the frame was spatially homomorphic filtered to remove low frequency spatial components, flatten the background intensity, and highlight edges that exist in each frame, such as the boundaries of each cell. A sigma value of 7 was used for the homomorphic filtering. Homomorphic filtered frames were then cross-correlated with a reference frame to determine how much the frame needed to shift to correct for any motion artifact. Lastly, both the raw frame and filtered frame was shifted by the calculated amount to remove the rigid motion artifact in the video. This general process can be broken up and sent out to parallel processes to speed up the motion correction.

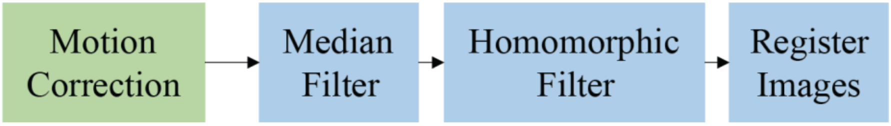

Figure 2. Motion Correction Process for Each Frame

Schematic shows the process for motion correction of each individual frame. First, each frame is median filtered to remove noise, followed by a homomorphic filter to remove spatial low frequencies and enhance edges. Lastly, each image is registered to a reference image using frame-wise cross-correlation.

Before implementing this process in parallel, one key difference needed to be developed. The reference frame in the real-time processing version was constantly changing as an aggregated average frame of all previous frames in the video. To motion correct in parallel, this could not be used as the reference frame as each process would require input from every other process to generate the reference, and thus could not be computed independently. To address this, the parallel motion correction pipeline performed a motion correction of a fixed number of beginning frames, typically one multipage tiff or 2047 frames. It used a noisy mean projection across the whole image as the initial reference frame. After motion correction to this noisy reference, a new motion corrected reference was generated from this sub-selection of motion corrected video frames. This reference frame was sent to each individual process for the correction of every other individual frame.

Once the reference frame was generated, motion correction of the remaining frames could be performed in parallel (Figure 3). Each individual frame of the remaining videos could be sent to a process individually with a copy of the reference frame, have each filtering and cross-correlation step performed, and the corrected frame with the x and y shift values returned to the central process to aggregate the corrected videos. Calculated x and y shift values were also outputted and saved in the event videos need to be re-motion corrected at some point due to file corruption. This can allow for the videos to not have to be fully re-processed as the shifts can be applied to each frame directly. Additionally, the frames used to generate the reference are also re-corrected to the new reference for consistency, though being able to do the full process in parallel overcomes any lost time from re-correcting those individual frames. To process one full dataset in a serial fashion took 4712 seconds (1 hour 18 minutes and 30 seconds) while processing the same dataset in a parallel fashion took 4231 seconds (1 hour 10 minutes and 30 seconds) using 32 cores, a decrease of 10% of the processing time.

In addition to building upon the previously published pipeline, this version of the pipeline was written with the intent to be open-sourced and user friendly. To this end, the pipeline was written in Python, a freely available coding language. Each component of the pipeline was also modularized for others to use as fits their specific needs. The initially published version of code was used for preprocessing of the calcium imaging data in Chapter 3, but this version was used for the data in Chapter 4. The code for this pipeline is called “Python Tif Motion Correction (PTMC)” and is available on the Han Lab GitHub Organization site (github.com/HanLabBU/ptmc).

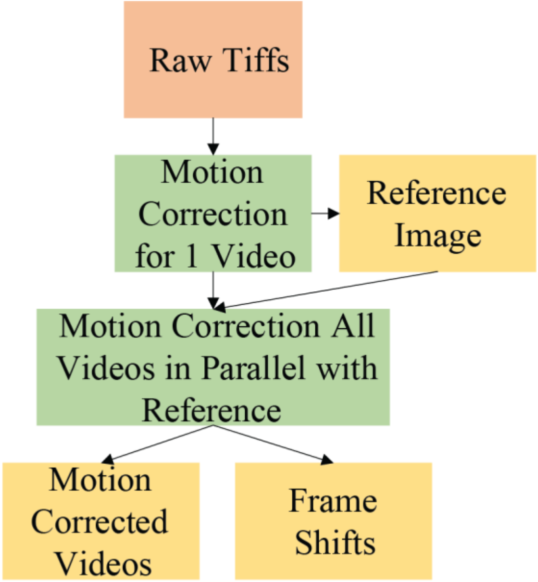

Figure 3. Schematic of Parallel Motion Correction Pipeline

Outline of motion correction as implemented in parallel. Orange boxes represent inputs, yellow boxes represent outputs, and green boxes represent the process of motion correction outlined in Figure 2. First, one single video was motion corrected to an average projection of itself to generate a reference image. That reference image is then sent to multiple parallel processes with individual frames to correct each frame in parallel. The motion corrected images are then aggregated after parallel processing and saved as output, along with the x and y directional shifts of each individual frame.

2.4 Semi-automated Image Segmentation Toolbox

After motion correction of calcium imaging data, individual neurons need to be segmented to extract temporal traces. Without clean and effective segmentation, researchers cannot have confidence in the downstream conclusions they arrive at with their data. While automated segmentation methods have many advantages over semi-automated methods, though one major limitation of currently published automated methods is that the quality of ROIs selected can be highly variable from dataset to dataset [20], [79]–[82]. To address this, some methods include a semi-automated “clean-up” method to inspect each ROI and temporal trace and exclude any that the user does not want to include in their dataset [79], [81]. However, this process can still be time consuming and it is difficult to simply alter or adjust the ROI if it is clearly including a combination of cells. Some of these limitations led to the development of a fully semi-automated image segmentation toolbox to enable the selection of ROIs with high confidence in their quality.

The image segmentation toolbox was developed to allow the user flexibility in selecting how to segment ROIs from their videos. Input types allow for either a single projection image produced from the motion corrected video or a three-dimensional tensor including video frames over time. Typical projection images include a maximum projection image with either a minimum projection or mean projection subtracted from it to increase the signal to noise ratio for each pixel. Video inputs as tensors can either include the full video extent or a temporally sub-sampled tensor for quicker calculations.

After loading the input data of choice, spatial segmentations of neurons can be done as either a circle of fixed radius, or segmentation of the full extent of the cells. To select circles of a fixed radius, the user simply needs to click once in the center of each cell they would like to segment (Figure 4A). The advantage of fixed circle size is it can provide segmentation of the dataset much more quickly, though you cannot compare the spatial footprint of different cells as the selected ROIs are all the same size, and you have a slightly lower signal to noise ratio for each cell. To segment the full extent of the cell, a large ROI that encompasses the full cell is selected, and a user-controlled dynamic thresholding method is used to refine the ROI within that larger boundary. This process is then repeated for the selection of each ROI. While more time intensive, the dynamic thresholding method provides more detailed spatial information about segmented cells (Figure 4B).

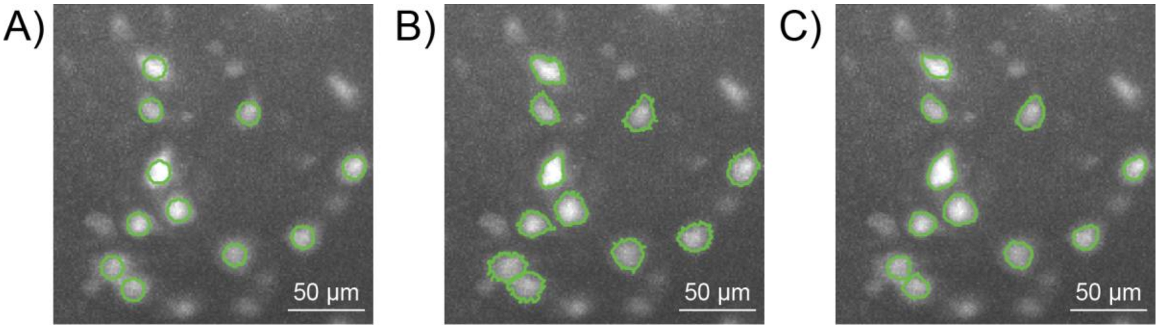

Figure 4. Examples of User Segmentation Options

(A) Circle of fixed radius selection overlaid on a projection image. **(B)** Full extent ROIs selected using the user controlled dynamic thresholding method on the raw input map. **(C)** Full extent ROIs selected from a cross-correlation map. Selection using temporal information tends to lead to smoother ROI boundaries than segmentation on the raw input map.

Additional contrast can be obtained in segmentation images by using the temporal information across the video. In addition to segmentation on the static projection image (Figure 5A), temporal cross-correlation or principal component analysis (PCA) can be performed to project the temporal information into the static projection. Segmentation using temporal composite images typically results in smoother boundaries around each ROI (Figure 4C). A cross-correlation map measures the pixel-wise cross correlation and represents it as an intensity value in the image. Pixels that are correlated with one another will have a higher correlation value, making it easier to segment single cells (Figure 5B). The PCA method calculates the first three principle components across each time series and represents each one as a red-green-blue (RGB) value for every pixel. These principle components are then represented as an RGB image for segmentation (Figure 5C). This method is most useful when cells are very densely labelled, as it can help distinguish nearby cells with different temporal traces from one another. These methods are possible on large scale datasets because pixels in a field of view are spatially subsampled based on user input. To generate any of these measures on the full dataset is too time intensive to be practical.

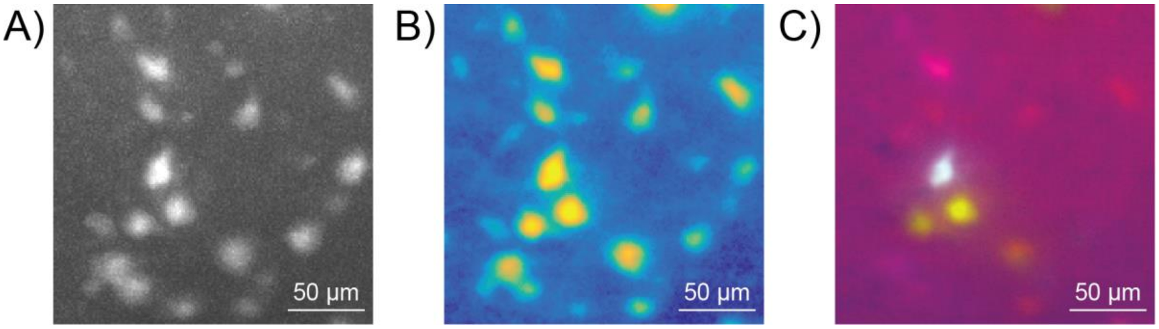

Figure 5. Segmentation Images Generated from Temporal Information

(A) Raw input image of maximum-minimum projection for segmentation. (B) Pixel-wise cross-correlation map of user-defined inset. Higher intensities represent higher correlation values between neighboring pixels, which makes cells easier to distinguish. (C) First 3 principal components from time series represented as RGB values for field of view.

After segmentation of the video from user selected input, the spatial location of each ROI corresponding to a cell is saved. Pixel values from the segmentation are then used to extract temporal time traces from the full motion corrected video datasets.

This segmentation toolbox was designed to be user-friendly and allow researchers to have high confidence in the segmentation of their datasets. To this end, this toolbox is still used by several non-computationally focused collaborators, as well as the fact that this toolbox was used to segment the “ground-truth” datasets for an automated segmentation paper previously published [90]. For generating such ground-truth datasets, high confidence in the segmented ROIs was extremely important for benchmarking the effectiveness of the automated methods. It is also important to note that many of the design elements of the software, such as using cross-correlation and PCA projection images, are not unique to this toolbox. Similar methods are used in many commercial software, as well as a toolbox developed by Dr. Michael Economo for in-house analyses in the Wachowiak lab [75]. The main advantage of this work was that it implemented these tools in a Matlab toolbox that was provided in an open-source repository for others to use. Similar to the motion correction pipeline, this toolbox is called “SemiSeg” and is available on the Han Lab GitHub Organization site (github.com/HanLabBU/SemiSeg)

2.5 Future Directions

The motion correction pipeline and image segmentation toolbox described herein provide useful tools for large scale calcium imaging datasets. These methods can continue to be improved in various ways to further improve the preprocessing steps for large scale calcium imaging datasets.

For the motion correction pipeline, two main sources of improvement would include adding graphics processing unit (GPU) acceleration and further parallelization in a cluster environment. As motion correction is primarily a graphics-based process, GPUs are highly optimized to perform the associated computations in a quick and efficient manner. Integrating that with this parallel toolbox can further improve the processing speed of these large datasets. Additionally, one of the major bottlenecks in processing these videos is in loading the video frames into memory. Once a reference image is generated for a dataset, each individual multipage tiff could be sent out in parallel to an individual node in a cluster computing environment. For these datasets, that would decrease the runtime of motion correction by roughly a factor of 13-20, depending on the number of files for each recording, which would represent a huge performance boost.

One improvement of interest for the image segmentation toolbox would be to develop a Python version. Python is an open-source language and more easily accessed without the paywall restrictions of Matlab. Additionally, Matlab occasionally implements upgrades that fundamentally changes core components of their code, which often breaks older versions of code. With Python, you can always install an older version of the code-base, which is not an option with a paid software like Matlab. These are some of the aspects that are attractive for developing a truly open-source tool for researchers to use for large scale calcium imaging.

In conclusion, we developed a motion correction pipeline and image segmentation toolbox designed for large scale calcium imaging datasets that improved over previously published and utilized methods. These methods were used during the further scientific discovery process and method development described in this dissertation.

CHAPTER 3 – MILD BLAST INJURY PRODUCES ACUTE CHANGES IN BASAL INTRACELLULAR CALCIUM LEVELS AND ACTIVITY PATTERNS IN MOUSE HIPPOCAMPAL NEURONS

3.1 Abstract

Mild traumatic brain injury (mTBI) represents a serious public health concern. Although much is understood about long- term changes in cell signaling and anatomical pathologies associated with mTBI, little is known about acute changes in neuronal function. Using large scale Ca^{2+} imaging in vivo, we characterized the intracellular Ca^{2+} dynamics in thousands of individual hippocampal neurons using a repetitive mild blast injury model in which blasts were directed onto the cranium of unanesthetized mice on two consecutive days. Immediately following each blast event, neurons exhibited two types of changes in Ca^{2+} dynamics at different time scales. One was a reduction in slow Ca^{2+} dynamics that corresponded to shifts in basal intracellular Ca^{2+} levels at a time scale of minutes, suggesting a disruption of biochemical signaling. The second was a reduction in the rates of fast transient Ca^{2+} fluctuations at the sub-second time scale, which are known to be closely linked to neural activity. Interestingly, the blast-induced changes in basal Ca^{2+} levels were independent of the changes in the rates of fast Ca^{2+} transients, suggesting that blasts had heterogeneous effects on different cell populations. Both types of changes recovered after ~1 h. Together, our results demonstrate that mTBI induced acute, heterogeneous changes in neuronal function, altering intracellular Ca^{2+} dynamics across different time scales, which may contribute to the initiation of longer-term pathologies.

3.2 Introduction

Traumatic brain injury (TBI) due to blast represents a serious public health concern, particularly in military settings [40], [41]. Four categories of blast injury have been established. Primary injury results directly from exposure to the blast wave, whereas secondary, tertiary and quaternary blast injuries are associated with collisions with projectiles set in motion by the blast, hitting other nearby objects, or from being exposed to the heat and noxious chemicals accompanying the blast, respectively [91]–[95]. Of the different types of blasted related injuries, primary injury is the most complex and remains the least understood, as there is often clear functional deficit in the absence of anatomical pathology [46], [96].

The pathophysiology of TBI can vary depending on the nature and severity of the injury. Although moderate and severe TBI receive considerable attention, mild TBI (mTBI) accounts for approximately 75% of injuries [46], [97]. Damages from mild injury can result in a broad spectrum of neurological deficits. For example, repeated mTBI has been associated with memory impairment, increased susceptibility to temporal lobe epilepsy, post-traumatic stress disorder (PTSD), and neurodegeneration, as observed in chronic traumatic encephalopathy [40], [42]–[45], [93], [98], [99]. Blast-related impairments in learning and memory [43], as well as increased susceptibility to seizures [42], have motivated studies focused on the hippocampus due to its integral role in learning and memory and its contribution to temporal lobe seizures in humans [44], [45]. Several studies have reported that blast reduces hippocampal long term potentiation, and leads to the loss of GABAergic interneurons and other anatomical structural changes [46]–[48].

These pathologies have been linked to a number of biochemical and synaptic changes, involving various neurotransmitters and intracellular signaling pathways across all hippocampal sub-regions, including the dentate gyrus, CA1 and CA3.

Over the years, several animal models of blast injury have been developed using devices such as shock tubes, blast tubes, and detonation of explosives in open-fields, to study blast injury [98], [100], [101]. To understand the acute effects of mTBI on neuronal function, we here used a previously published cranium only blast injury model [101], to determine the feasibility of using wide-field imaging to examine Ca^{2+} changes in large numbers of individual CA1 neurons. This model has the advantage that the blast is confined to the cranium, and because no surgery is required, mice can be blasted in the absence of any anesthetics, allowing us to perform real time analysis in mice with full head mobility.

Recent developments in scientific CMOS cameras and high performance genetically encoded Ca^{2+} sensors such as GCaMP6, have enabled ultra-large scale Ca^{2+}imaging of thousands of individual neurons in the brain using wide-field microscopy [71]. Studies using GCaMP6 and earlier generations of genetically encoded Ca^{2+} sensors have consistently demonstrated that transient, sub-second changes of intracellular Ca^{2+} levels are closely correlated with neuronal spiking in many brain regions [71], [74], [86], [102]–[104]. In the hippocampal CA1 region, patterns of sub-second Ca^{2+} transients recorded in individual neurons closely paralleled the spiking patterns reported in electrophysiological studies, demonstrating that sub-second Ca^{2+} transients can be used to estimate neural activities [20], [78], [105], [106]. While a single spike can produce detectable changes in GCaMP6 fluorescence, most of the sub-second time scale GCaMP6 fluorescence transients observed in living brains are likely associated with bursts of spikes [71]. We previously demonstrated that wide-field Ca^{2+} imaging with GCaMP6 allows the ability to simultaneously image the activity of hundreds to thousands of individual hippocampal neurons in awake behaving mice [20]. Because of the simple instrumentation of wide-field Ca^{2+} imaging, this imaging modality can be easily adopted by many researchers to study acute changes in neuronal function following exposure to mild blasts. This study highlights the utility of this technique for studying mTBI, and reports some initial results using this technique in animals that experience a blast injury over two consecutive days.

3.3 Results

3.3.1 Wide field imaging of hippocampal CA1 neurons in awake mice upon mild traumatic blast injury (mTBI)

To examine the acute effects of mTBI on individual hippocampal neurons, we performed Ca^{2+} imaging using wide-field fluorescence microscopy (Figure 6A) in awake, head-fixed mice [20], before and immediately after a mild cranial blast injury. The mTBI was produced with a Cranium Only Blast Injury Apparatus (COBIA) that directs blast waves onto the freely moving head of a mouse (Figure 6B), adapted from that of Kuehn et al [101]. We note that although the mouse bodies were restrained in the COBIA, their heads moved freely to ensure the success of the blast injury model.

We calibrated our COBIA device using a sensor that had a 500 kHz resonant frequency (100 kHz maximum sampling frequency). With our calibration setup, the blast peak overpressure reached 1,399 ± 252 kPa (mean ± std, n=5 tests) at a single time point (~2 μs) (Figure 6C). To compare to the measurements reported in Kuehn et al. (2011), we filtered the pressure trace at 12 kHz and obtained a transient overpressure of 322 ± 92 kPa (mean ± std), which was slightly below the maximum overpressure they reported [101]. To compare to the shock tube device reported by Goldstein et al. (2012), we filtered the blast pressure trace at 2 KHz, and detected a peak pressure of 178 ± 26 kPa, which is above the 77 kPa they reported [98]. The severity of blast injury is typically attributed to the magnitude of the pressure produced (peak blast overpressure), and the duration of peak overpressure [93], [100], [101], [107]. Because none of our blasted animals lost consciousness or exhibited noticeable abnormal behavior immediately following blast or the week after, and the general agreement of the blast overpressure of our experiment with prior studies, we consider our COBIA model to be mTBI [98], [101].

Several weeks prior to testing, mice were surgically injected with AAV9-syn-GCaMP6f virus encoding the genetically encoded Ca^{2+} sensor GCaMP6f into the CA1, and implanted with a custom imaging window over the injection site. Upon complete recovery from the surgeries, mice were blasted and imaged each day on two consecutive days (Figure 6D). Prior to each blast, we first imaged spontaneous Ca^{2+} dynamics for 100 seconds in mice that were awake and head-fixed under the imaging setup. We then transferred the mice to the COBIA, where they received a single cranial blast with free head movement. Immediately after the blast, we transferred the animals back to the imaging setup, and imaged awake and head-fixed for 100 seconds every 10-20 minutes until about one hour after the blast (Figure 6E). Because the COBIA also produced a transient loud noise, we performed a sham study in mice that were prepared in an identical fashion, but positioned next to the COBIA during the blast portion of the protocol. Sham-exposed mice were also allowed free head movement, and thus they experienced the blast related noise without being exposed to any blast pressure waves. Each mouse was blasted and imaged each day on two consecutive days (n=4 blasted mice) or sham-exposed on each of the two consecutive days (n=5 sham-exposed mice).

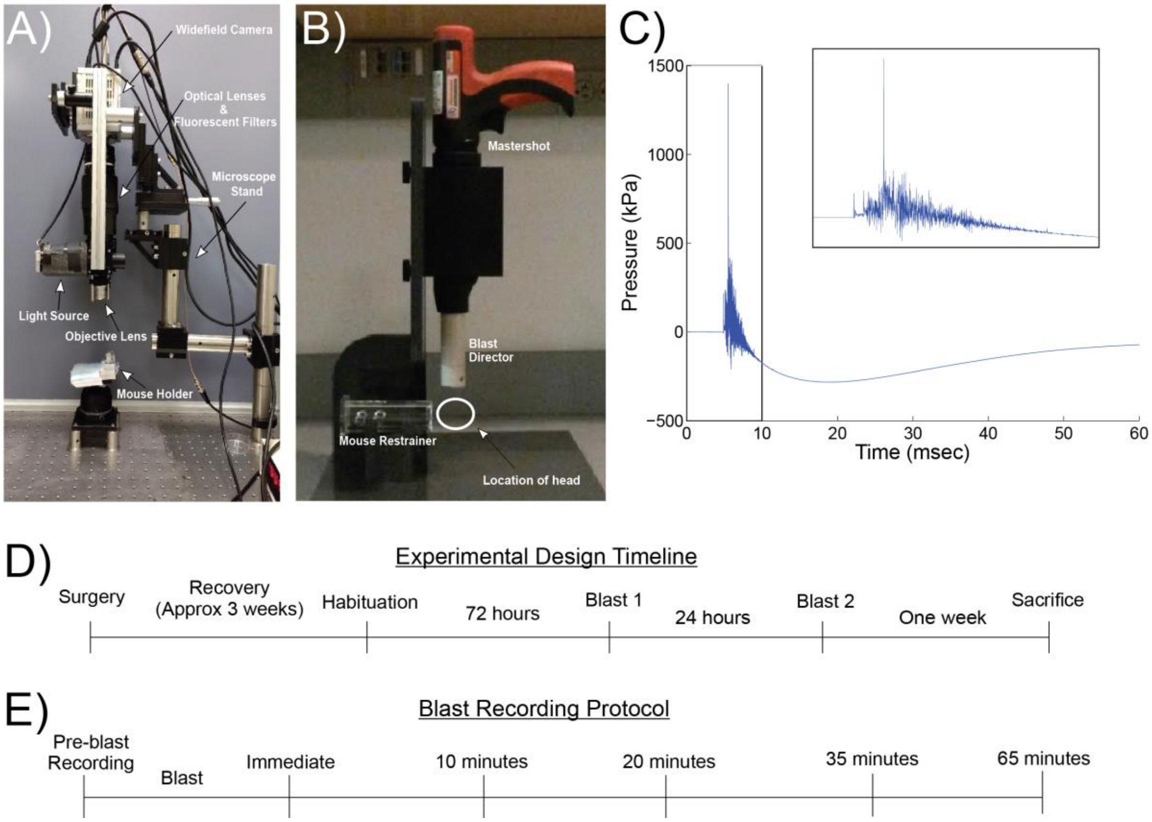

Figure 6. Experimental design for wide-field Ca^{2+} imaging of hippocampal neurons in mice exposed to a cranial blast

(A) A wide-field fluorescence microscope coupled to a sCMOS camera was used to image neurons expressing a genetically encoded Ca^{2+} sensor (GCaMP6f) *in vivo*. **(B)** The Cranium Only Blast Injury Apparatus (COBIA) consisted of a modified nail gun coupled to a blast director to direct the blast wave vertically onto the freely moving head of un-anesthetized mice. The distance from the animal's head to the opening of the blast director was 2 cm. **(C)** Waveform of average overpressures (n=5 tests) generated from the COBIA. Inset shows the zoom in of the waveform over 10ms. **(D)** Experimental timeline. **(E)** Ca^{2+} imaging protocol during each blast session.

3.3.2 Blast exposure induced both sustained and transient intracellular Ca^{2+} changes in a large number of individual neurons

The wide-field imaging system, equipped with a sCMOS camera and a 10X objective lens, allowed us to image over a 1.343 x 1.343 mm^2 brain area containing hundreds of individual neurons in each mouse (Figure 7A). In one representative session, we recorded 554 neurons before blast, and 467 neurons after blast (Figure 7B). The difference in the number of neurons identified between the pre- and post- blast sessions in the same mice was due to the fact that the blast procedure was conducted in mice whose heads were not restrained. Thus, the same neurons often could not be easily registered before and after the blast. However, because we imaged the same brain area from the same imaging window, a majority of cells recorded before and after the blast were expected to come from the same neuronal population.

Before the blast, most neurons exhibited transient and dynamic GCaMP6f signals on a sub-second time scale, consistent with Ca^{2+} changes associated with neural activities [71], [74], [85], [86], [102]–[104], [108], [109]. These Ca^{2+} transients, on the sub-second time scale, were sparse over time, and were present in cells across the entire imaging field (Supplemental Video 1). The overall dynamics of these patterns were consistent with those reported previously for spontaneous CA1 Ca^{2+} transients associated with spiking [20], [78], [105], [106]. Immediately after blast, we observed a drastic change in the pattern of GCaMP6f signals (Figure 7A). A substantial fraction of cells exhibited a sustained reduction in their sustained basal intracellular Ca^{2+} levels, as well as a reduction in the frequency of sub-second Ca^{2+} transients.

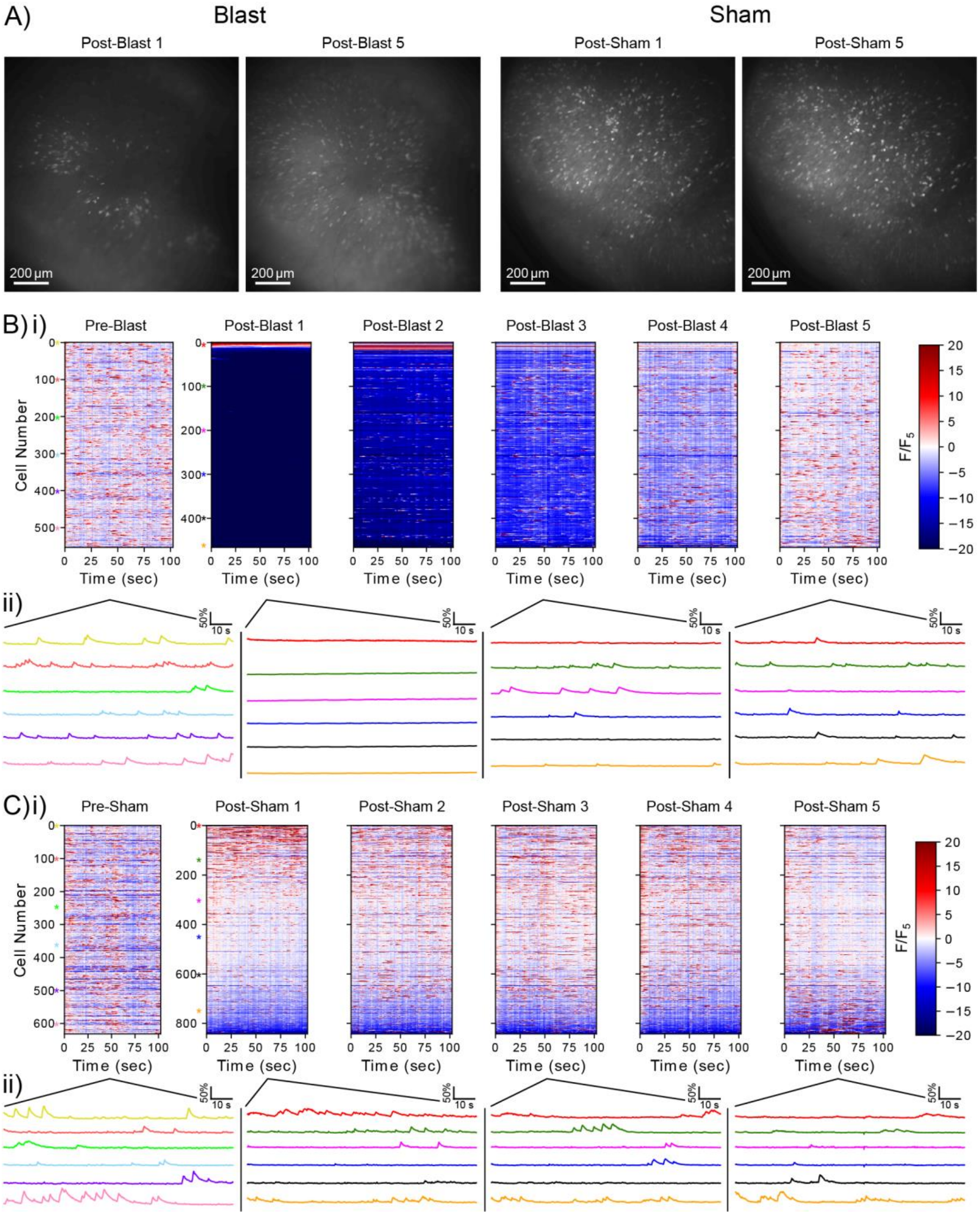

Figure 7. Blast altered intracellular Ca^{2+} dynamics in individual hippocampal neurons

(A) Maximum projection of GCaMP6 fluorescence intensity across all imaging frames during a 100 seconds long recording period for a representative blasted mouse (left) and a representative sham noise-exposed mouse (right). Post-Blast/Sham period 1 was immediately after the blast, and Post-Blast/Sham period 5 was about 65 minutes after the blast. Images were contrast enhanced using the same contrast scaling factor for both periods 1 and 5. **(B, C)** Ca^{2+} traces (normalized by the mean fluorescence in period 5) of individual neurons identified in a representative blasted mouse (B) and in a representative sham noise-exposed mouse (C), before and after blast. (i) Traces were sorted by the mean fluorescence in the pre-blast or post-blast period 1 respectively. Sorting order of a given neuron from period 1 was maintained across the remaining blast periods. (ii) Representative Ca^{2+} traces of specific representative neurons with different levels of intracellular Ca^{2+}, as indicated by the colored asterisks in (i).

In addition, we found a very small fraction of cells that exhibited sustained elevation of basal intracellular Ca^{2+} levels after blast, which appeared constantly bright in the imaging field (Supplemental Video 1). Changes in both the sub-second Ca^{2+} transients and the slow sustained basal intracellular Ca^{2+} levels slowly recovered over time. In most blast sessions, patterns of Ca^{2+} dynamics observed at the end of the recording session, about one hour after the blast, were visually indistinguishable from that observed during the pre-blast baseline period. However, there was one blast session on the second day (out of total of eight sessions in four animals), where Ca^{2+} dynamics remained attenuated and sparse one hour after blast.

In sham mice, we did not detect noticeable changes in either the sub-second Ca^{2+} transients or the slow sustained basal intracellular Ca^{2+} levels (Figure 7C & Supplemental Video 2). Since it took about five minutes to transfer animals from the COBIA blast device back to the imaging setup, we could not determine the precise time when the changes in Ca^{2+} dynamics were first initiated by the blast.

3.3.3 Mild blast injury reduced basal intracellular Ca^{2+} *levels in most neurons*

Because we could not easily register a one-to-one match among imaged neurons before and after blast, we first examined population neural activity observed ~65 minutes after blast (Period-5) versus that observed during pre-blast period as those seemed qualitatively similar. We compared the histogram distributions of mean basal Ca^{2+} levels across all neurons for each mouse between the Pre-Blast period and Period-5, and found no statistically difference (Wilcoxon Rank Sum Test, $p>0.05$), consistent with our visual evaluation (Supplemental Video 1). Then to examine the immediate effects of blast at the individual neuron level, we compared the first 100-second long imaging session immediately after blast (Period-1) and the last 100-second imaging session ~65 minutes after the blast (Period-5) when activity largely recovered to that of pre-blast period in most cases.

To estimate the slow, sustained, basal intracellular Ca^{2+} changes induced by blast, we constructed a probability density estimate (PDE) for each neuron's fluorescence intensity in Period-1 and Period-5 (Figure 8). The fluorescence intensity of a given neuron sampled at each image frame was used to calculate the PDE. The mean of the PDE represents the overall basal intracellular Ca^{2+} levels averaged over the given 100-second long imaging period, and the distribution of the PDE estimates the temporal variation within the imaging period.

In the blast group, the PDEs of most neurons during Period-1 were drastically shifted towards smaller intensity values when compared to that during Period-5 (Figure 8Aii), suggesting that blast reduced basal intracellular Ca^{2+} levels in most neurons. Interestingly, the PDEs of a small portion of neurons (a representative one is shown in Figure 8Ai) were shifted to higher intensity values, suggesting that blast increased the intracellular Ca^{2+} levels of these neurons. For the few cells that showed little change in the overall mean intensity, they exhibited a small shift in the distribution, suggesting that these neurons exhibit more variable changes in intracellular Ca^{2+} levels than sham-blasted mice (Figure 8Aiii compared to Figure 8B).

We then calculated the mean of the PDEs of all neurons recorded in this blast session, and compared between Period-1 and Period-5 (Figure 8C). As a population, basal intracellular Ca^{2+} levels of most neurons in blasted mice were above the unity line, demonstrating that blast reduced the intracellular Ca^{2+} levels in most neurons. A few neurons were below the unity line, representing the neurons whose intracellular Ca^{2+} levels were elevated by the blast. This phenomenon was consistent across most blast sessions (Figure 8D). Our estimation of blast-induced effects represent a conservative measure, as it is possible that blast-induced changes may remain at some level during Period-5 that is still different from the pre-blast period, though not statistically significant. In addition, the comparison between Period-1 and Period-5 allows us to assess how individual neurons recover over time after each blast. Across sham-exposure sessions, the mean basal Ca^{2+} levels remained on the unity line, which confirmed that sham-exposure did not alter intracellular basal Ca^{2+} levels (n=10 sessions in 5 mice).

To further quantify the changes in individual neurons, we estimated the variation of the PDEs across all neurons recorded in the sham group where blast did not alter the mean basal calcium levels. We then used the 95% confidence interval of the width of this distribution as a threshold to determine significance along the unity line. If a neuron's mean fluorescence intensity during Period-1 was significantly smaller than its intensity during Period-5, we classified this neuron as significantly suppressed by the blast. If a neuron's mean fluorescent intensity during Period-1 was significantly larger during Period-5, we classified this neuron as significantly elevated by the blast. If a neuron's mean fluorescence intensity was within a 95% confidence interval between Period-1 and Period-5, it was considered to have a consistent basal calcium level. For the blasted mice, 55.5 ± 24.8% of cells were suppressed, while for sham mice only 5.83 ± 9.26% of cells were suppressed for the second blast day (Wilcoxon Rank-Sum $W = 15$, $n_b = 4$ $n_s = 5$ mice, $p = 0.016$, two-tailed). It is interesting to note that the percentage of cells in this population that were suppressed doubled between the blasts, going from 20% of the cells on day 1 to 55% of the cells on day 2 of blasting (Figure 8E).

Together, these results suggest that mild blast caused wide spread, sustained reductions in basal intracellular Ca^{2+} levels in a large fraction of individual hippocampal neurons. A larger fraction of hippocampal neurons was impacted during the second blast compared to the first blast. While the intracellular Ca^{2+} levels in most neurons were reduced following blast, a small fraction of cells exhibited long lasting increase in intracellular Ca^{2+}. These changes in intracellular Ca^{2+} recovered on a timescale of minutes, and returned to similar patterns as that observed before blast. Considering the importance of intracellular Ca^{2+} in cell signaling pathways and gene expression, such a shift in basal intracellular Ca^{2+} levels over a time course of minutes could lead to longer term changes in membrane excitability, synaptic remodeling and structural plasticity.

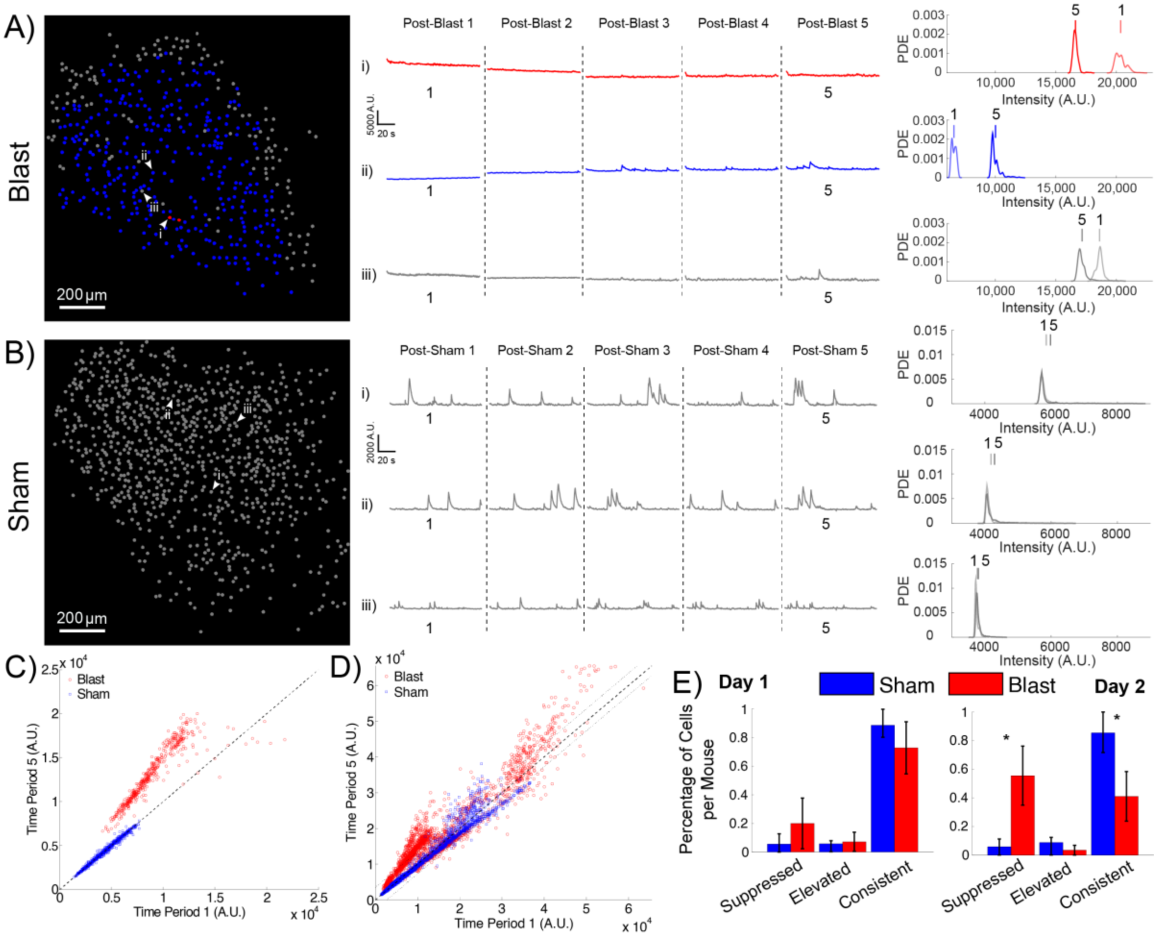

Figure 8. Blast reduced intracellular basal Ca^{2+} levels

(A) Left: spatial distribution of cells whose intracellular Ca^{2+} levels were elevated (red), suppressed (blue), or non-modulated (gray) in a representative blasted mouse. Middle: Ca^{2+} traces for the three representative neurons indicated in the spatial map. Right: the probability density estimates (PDE) of the neurons (shown in the middle) for imaging period-1 and period-5. The short vertical lines above the density distributions correspond to the mean of each respective density and highlight the shift in intracellular calcium levels between the imaging sessions. A.U.: arbitrary units, as measured by 16-bit pixel intensities. **(B)** Spatial distribution map, Ca^{2+} traces, and probability density estimates for a representative sham noise-exposed mouse. **(C)** The mean fluorescence intensity of all cells during period-1 plotted against the mean fluorescence intensity during period-5 for the representative blasted mouse (red) and the representative sham-blasted mouse (blue) shown in A and B respectively. Dotted black line is the unity line. **(D)** All neurons recorded in all blast sessions (red, 2781 neurons) and all sham sessions (blue, 3259 neurons) during period-1 plotted against period-5. Dotted black line is the unity line, and dotted gray lines indicate 95% confidence interval used to classify elevated and suppressed cells. **(F)** The fraction of cells that were suppressed, elevated or non-modulated, averaged across mice, for the first blast (day 1) and the second blast (day 2). More neurons were suppressed after the second blast (*: $p<0.05$, Wilcoxon Rank-Sum). Error bars represent the quartile range.

3.3.4 Mild blast injury reduces individual neuronal activity measured as Ca^{2+} transients

In addition to altering slow basal intracellular Ca^{2+} levels, blast also impacted the faster, sub-second time scale Ca^{2+} transients, known to be correlated with neural activity [71], [74], [85], [86], [102]–[104], [108], [109]. Immediately after blast, many neurons were largely inactive and exhibited few Ca^{2+} transients for an extended period of time (Figure 7B & Figure 9A-Post-Blast 1-2 and Supplemental Video 1). Ca^{2+} transients recovered gradually, and in most blast sessions by the last recording session (approximately one hour after blast), they were similar to the pre-blast state. In the sham group, Ca^{2+} transients showed little change following exposure to the sound of the blast thus confirming that noise alone did not cause the changes in Ca^{2+} transient events recorded in the blast group.

To quantify the effect of blast on Ca^{2+} transients for individual neurons, we calculated the frequency of the sub-second long Ca^{2+} transients. To dissociate the sub-second timescale of Ca^{2+} transients from the sustained long-lasting basal Ca^{2+} level shifts, we first calculated the changes in fluorescence from the mean fluorescence (ΔF) for each neuron within a given 100s long imaging period. We then normalized ΔF to the mean of the last imaging period (F_5) to highlight any change in the frequency of Ca^{2+} transients (Figure 9A-B). This normalization allowed optimal detection of changes in transient Ca^{2+} events, without any bias from effects of the basal Ca^{2+} level changes. To calculate the rate of Ca^{2+} transient events, we first converted normalized Ca^{2+} traces to binary traces to identify the rising phase of GCaMP6 signals (ones), and counted the number of Ca^{2+} events occurred for each 100 second recording time period, before and after each blast.

We found that mean Ca^{2+} event rates of all neurons simultaneously recorded in each imaging session before blast were comparable between the blasted and the sham groups (blast: 2.20 ± 0.19 events, mean ± s.d, n=4 mice; sham: 2.28 ± 0.42 events, mean ± s.d., n=5 mice). Ca^{2+} event rate dropped significantly to 0.47 ± 0.3 events per 100 seconds for the blast group, compared to 1.45 ± 0.47 events for the sham group (Wilcoxon Rank-Sum W=35, n_b = 4 n_s = 5 mice, p = 0.016, two-tailed). Ca^{2+} events rates then quickly recovered over the subsequent tens of minutes following blast (Figure 9C, p>0.05). On the second day, the average calcium event rate returned to ~2 events per 100 seconds for both sham and blast groups before blast. Following the second blast, the event rate again dropped sharply and recovered slower on the second day compared to the first day, although this pronounced decline was not statistically significant.

To determine the fraction of cells in each mouse that exhibited a change in Ca^{2+} event rates, we compared the event rate in Period-1 to that in Period-5 for each cell. A bootstrapping method was used to determine whether the frequency of Ca^{2+} transients for each neuron were significantly different between Period-1 and Period-5, to classify neurons as significantly increased, decreased or non-modulated. We found that following the first blast, 58.5 ± 20.3% (mean ± s.d.) of cells showed a decrease in response to blast, significantly different from the 26.5 ± 6.3% of cells upon sham exposure (Wilcoxon Rank-Sum W = 16, n_b = 4 n_s = 5 mice, p = 0.032, two-tailed). In addition, we found that 44.6 ± 11.3% of neurons in sham mice showed an increase in the frequency of Ca^{2+} transients over time, but only 13.6 ± 11.8% of neurons in the blasted mice exhibited such increase (Wilcoxon Rank-Sum W = 35, n_b = 4 n_s = 5 mice, p = 0.0159, two-tailed). These proportions were different for the second day of blasting, with the number of calcium events being more comparable to the sham mice (Figure 9D).

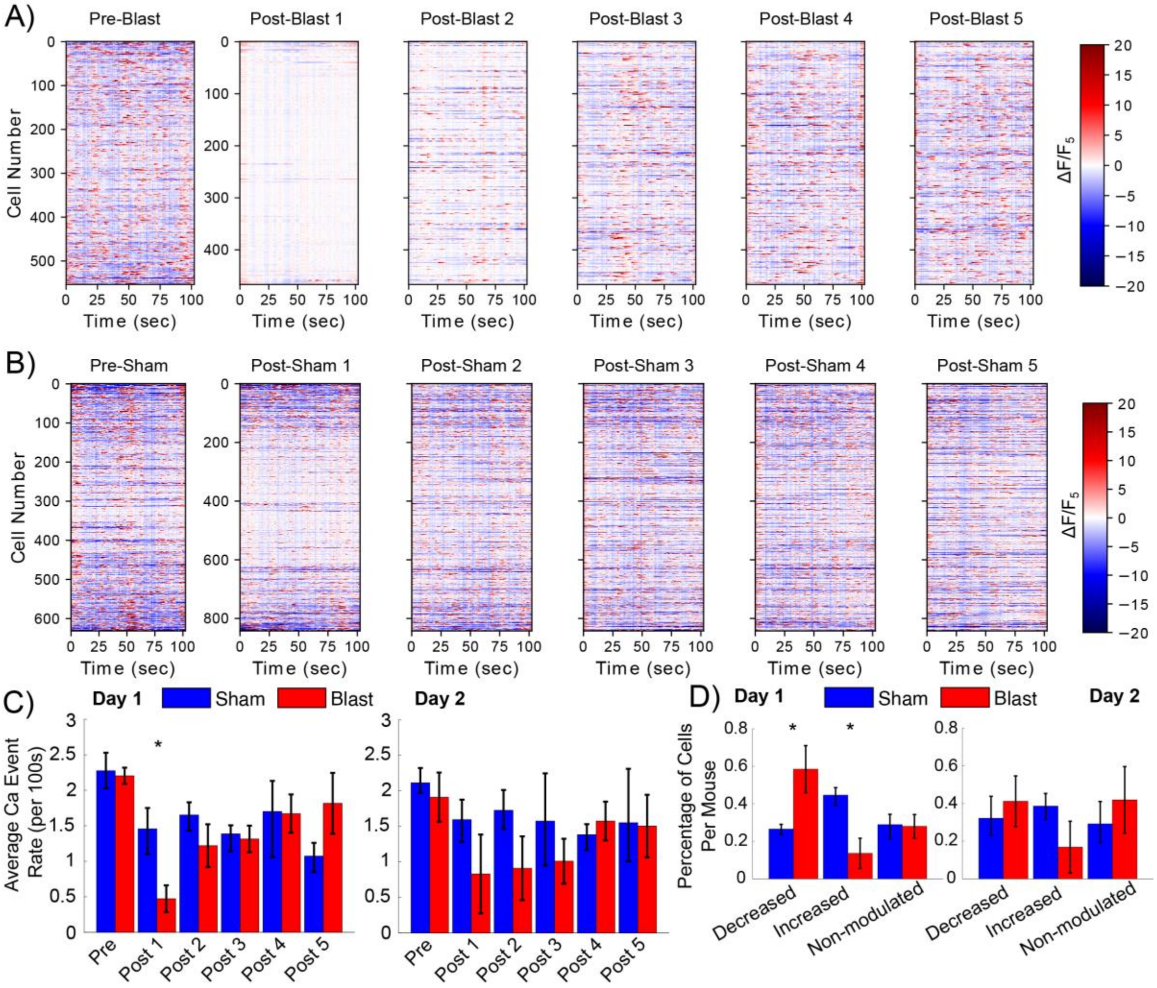

Figure 9. Blast decreased calcium transient event rates in individual neurons

(A, B) Sub-second Ca^{2+} transients, events closely related to neural activity, plotted for individual neurons for different time periods after blast in a blasted mouse (A), and a sham noise-exposed mouse (B). Cells were sorted using the same order as shown in Figure 7. Transient Ca^{2+} events were calculated using $\Delta F/F_5$ rather than F/F_5 to highlight transient events occurring on top of the slower basal changes in intracellular Ca^{2+} levels. (C) The average number of calcium events before and after the first blast (day 1) and the second blast (day 2), plotted for the 6 recording periods each day. (*: $p<0.05$, Wilcoxon Rank-Sum). Error bars represent the quartile range. **(D)** The fraction of neurons exhibiting decreased, increased and non-modulated Ca^{2+} event rates. (*: $p<0.05$, Wilcoxon Rank-Sum). Error bars represent the quartile range. (n=4 blast mice, and 5 sham mice).

3.3.5 Heterogeneous effects of blast on intracellular Ca^{2+} dynamics at different time scales

Interestingly, when comparing changes between basal intracellular Ca^{2+} levels and the frequency of Ca^{2+} transients, we failed to find a clear relationship (Figure 10). When plotting the full population of neurons comparing the difference in the average number of Ca^{2+} events with the difference in the basal Ca^{2+} levels, we found no linear relationship between the two for either blasting days (blast: R^2=0.1141 and 0.0031 for the first and second blast respectively; sham: R^2=0.0371 and 0.0206 for the first and second sham exposure respectively). Sham mice had a tighter distribution of the average basal Ca^{2+} levels, while blast mice showed a broader distribution of differences in basal Ca^{2+} levels. Interestingly, a few neurons in the sham group exhibited changes throughout the full range of basal Ca^{2+} level changes and the frequency of Ca^{2+} transient changes, suggesting blast-induced changes are physiologically achievable. These results demonstrate heterogeneous effects of blast on both basal and transient Ca^{2+} changes, which could involve different cellular mechanisms, and also confirmed that our imaging technique and analysis methods can independently detect changes in transient sub-second Ca^{2+} events and sustained basal shift in intracellular Ca^{2+} levels.

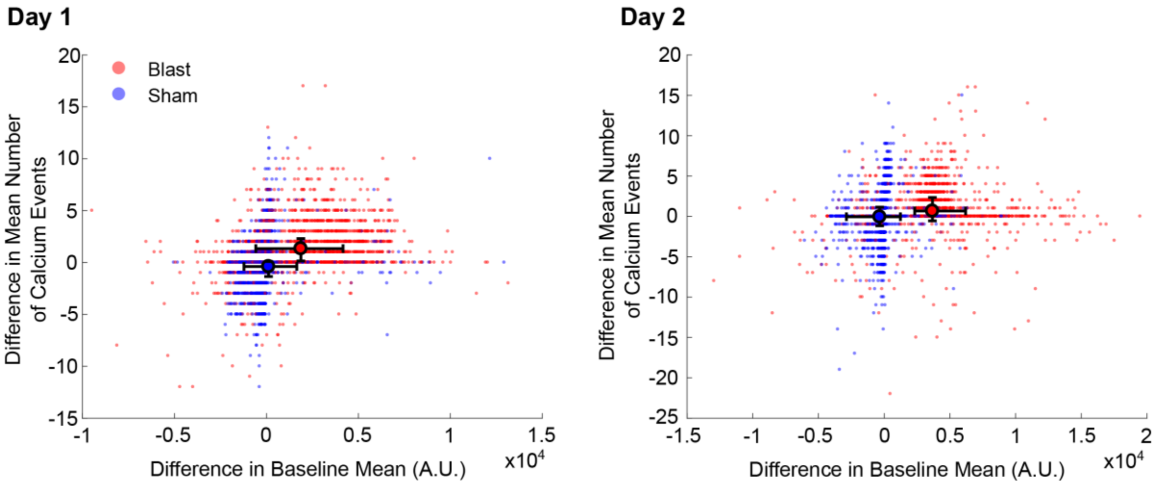

Figure 10. Blast induced changes in baseline calcium levels are independent of the changes in Ca^{2+} event rates

Each dot representing a single cell is plotted comparing the change in the mean baseline Ca^{2+} level with the change in the number of Ca^{2+} events over the 100 second recording period immediately after blast. Day 2 showed a greater divergence in the baseline mean, although both days showed similar cellular responses in the change in Ca^{2+} events. While the range of values was observed in both blast and sham conditions was similar, the fraction of cells exhibiting stronger deviations from the center was much larger in the blast condition than the sham condition. Large colored dots represent the mean of each value across mice for either the sham or the blast group, and error bars represent the quantile range spanning 95% of the data.

3.3.6 No significant differences in glia immunoreactivity one week following repetitive blasts

Immunocytochemistry was performed one week after the second blast to identify morphological changes in cytoarchitecture and to evaluate the status of glia (Figure 11). We found no significant differences in the percent area occupied by GFAP labeled astrocytes between sham and blasted groups, either in the ipsilateral area directly underneath the imaging window (t=-0.404, df=10, p=0.695), or in the contralateral intact hemisphere (t=-0.876, df=6.698, p=0.411). We observed a slight increase in the area occupied by GFAP in the ipsilateral side underneath the imaging window, compared to the contralateral intact hemisphere in both blast and sham groups (sham: n=5 t=2.167, df=4, p=0.096; blast: n=6, t=1.580, df=6, p=0.165), consistent with local immune responses to imaging implants.

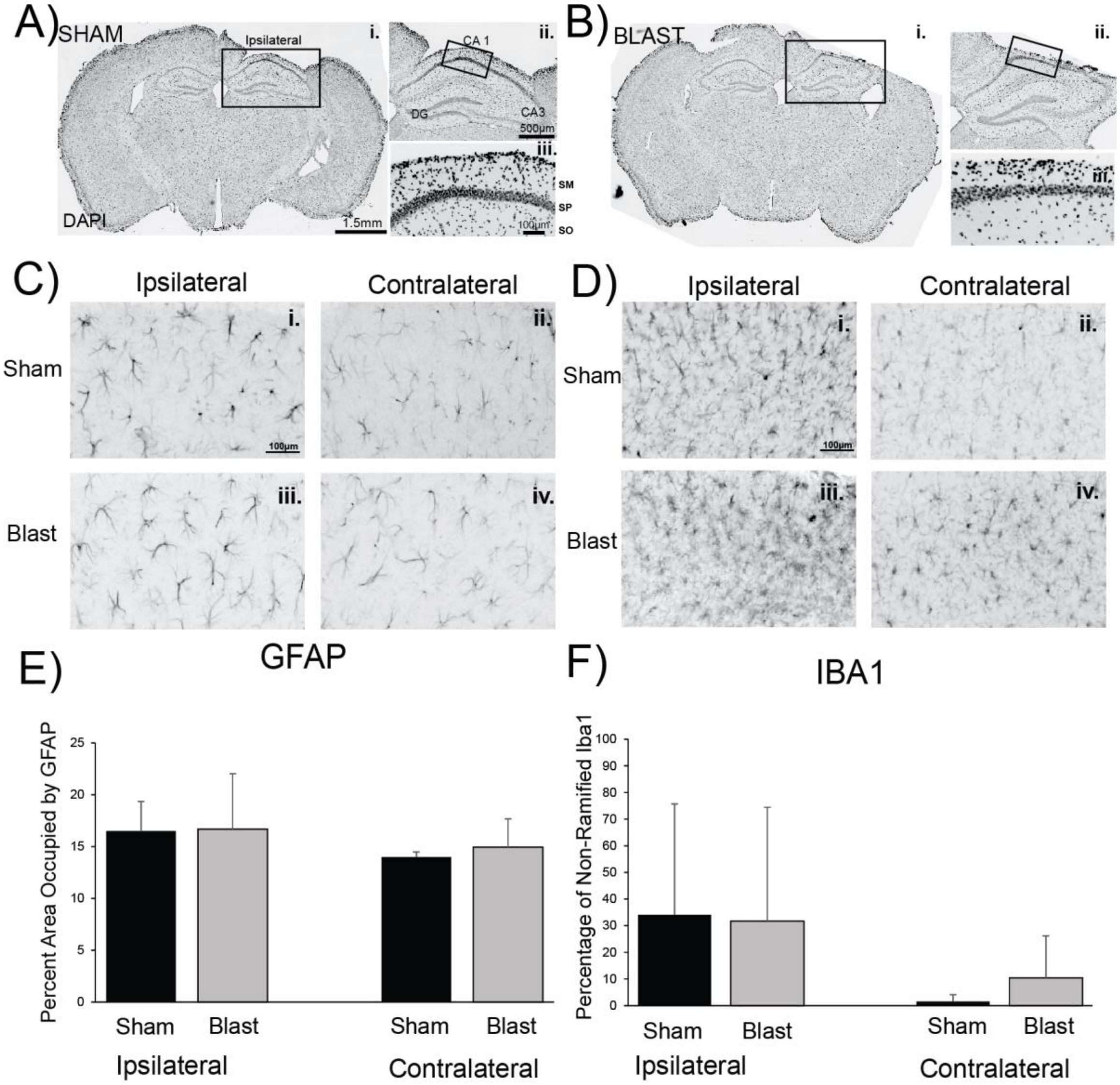

Figure 11. No significant differences in GFAP and Iba1 immunoreactivity following blasts

(A, B) DAPI labeled coronal sections from a representative sham-exposed mouse (Ai.-iii.) and a representative blasted mouse (Bi.-iii.). DAPI = 4’,6-Diamidino-2-Phenylindole. GFAP = glial fibrillary acidic protein. IBA1 = ionized Ca^{2+} binding adaptor molecule 1. CA1 = Cornu ammonis 1. SM = Stratum moleculare. SP = Stratum pyramidale. SO = Stratum oriens. **(C,D)** GFAP (Glial fibrillary acidic protein) immunofluorescence (C) and Iba1 (ionized Ca^{2+} binding adaptor molecule 1) immunofluorescence (D) from a sham mouse (top) and a blast exposed mouse (bottom), ipsilateral (i., iii.) and contralateral to the imaging window (ii., iv.). **E)** No significant difference in the percent area of GFAP immunofluorescence was observed between sham and blast exposed animals, either ipsilateral or contralateral to the imaging window. **(F)** No significant difference in the percentage non-ramified cells positive for Iba1 was observed between sham and blast exposed animals ipsilateral or contralateral to the imaging window.

In addition, no significant difference was observed in Iba1 phenotypes between sham and blasted groups under the imaging window (t=-0.329, df=9, p=0.749), as well as in the contralateral hemisphere (t=-1.299, df=6.475, p=0.238). Similar to GFAP labeled astrocytes, we observed a greater percentage of non-ramified Iba1 positive microglia in the ipsilateral area directly underneath the imaging window compared to the contralateral hemisphere, in both sham and blasted animals, though the difference was not significant (sham: n=5 t=1.693, df=4, p=0.166; blast: n=6, t=1.829, df=5, p=0.127).

3.4 Discussion

To examine the immediate functional effect of mild blast, we integrated a recently developed *in vivo* wide-field imaging technique to monitor intracellular Ca^{2+} changes in large numbers of individual hippocampal neurons in un-anesthetized mice, with an mTBI COBIA model that produced no drastic anatomical pathology. We found a significant effect on neural function after exposure to a single blast or repeated blasts. Blast produced heterogeneous effects on different neuron populations, across different time scales. Basal Ca^{2+} levels, on the time scale of minutes, were reduced in most neurons, suggesting that biochemical signaling may be affected. Transient Ca^{2+} events, on the sub-second time scale, were reduced in a large fraction of neurons, suggesting an impact on neural activity, likely due to changes in membrane excitability and/or synaptic signaling. Blast-induced transient Ca^{2+} activity changes showed little correlation with the shift of basal intracellular

Ca^{2+} levels, suggesting different modes of impact on membrane biophysics and synaptic processing versus biochemical pathophysiology of the blast. The observed functional changes over the time course of tens of minutes in the absence of anatomical pathology may be directly relevant to the immediate cognitive impact of blast and may contribute to the long lasting cellular changes. In addition, this study also highlights a novel technology platform that enables simultaneous analysis of a large number of individual neurons immediately after blast injury.

3.4.1 Blast Model

The severity of primary blast injury is typically attributed to the peak blast overpressure, the duration of peak overpressure, extent of head movement, distance from the blast, and the mortality rate [93], [100], [101], [107], [110], [111]. However, major differences in the construction of the devices used to generate the blasts [112]–[114], administration of anesthetics [68]–[70], types of animals used [115], their orientation with respect to blast [116], [117], and their recovery post blast can significantly affect injury outcome. A consensus to calibrate blast intensity based on the sampling frequency analyzed has not been reported to our knowledge, and the reported pressure measurements vary widely depending on the experimental setups. Kuehn et al. (2011) used a sensor with a 60 kHz resonant frequency and collected data at 333 kHz to obtain the peak pressure of 517 kPa using the same experimental setup that we adapted for the present study. Whereas Goldstein et al. (2012) reported the peak pressure of only 77 kPa using a shock tube. While our calibration results are in general agreement with these studies reporting mild blast injuries, future studies focused on standardizing calibration pressures would be beneficial for cross-study comparisons of blast-related injuries. Although we had a very high blast overpressure (1,399 ± 252 kPa), it's very short duration (~2 μs) probably contributed to the mild nature of the blast.

3.4.2 Evaluation of Astrocytes and Microglia Immunoreactivity

Although morphological changes used to infer the status of glial activation resulting from blasts have been reported, particularly following moderate and severe injuries, it is known that functional impairments can exist in the absence of morphological changes [46]. For example, Pun et al. (2011) reported acute microglial activation 24 hours following exposure to mild blast, which was then absent 4 and 7 days post blast, likely due to compensatory upregulation of reparative genes following blast exposure [118]. Consistent with Pun et al., we did not observe significant differences in astrocytes or microglia immunoreactivity one week following the final blast exposure. However, we cannot rule out the possibility that transient changes in glial morphology occurred prior to the sub-acute time point examined. Future studies are warranted to assess the temporal characteristics of glia morphologies and how the dynamic nature of glia may contribute to the functional responses following blast. Using the same experimental technique reported here, the acute changes of intracellular calcium in glia could also be studied in response to blast, as *in vivo* calcium imaging in glia has been performed previously [119].

3.4.3 Neuronal Functional Changes

To our knowledge, we report the first *in vivo* evidence of how neurons in un-anesthetized brains responded to blasts within minutes (~5 mins) after blast exposure.

While *in vivo* imaging has been utilized to examine a variety of neural networks involved in various behaviors [73], [74], [119]–[124], recent improvements in wide-field optical imaging allow simultaneous recording of cellular responses from hundreds to thousands of individual neurons, over relatively large brain areas, providing the opportunity to obtain finer details regarding the dynamic features of large neural networks [20], [125]. Using *in vivo* imaging in a blast injury rodent model, we identified acute changes in a large fraction of neurons within tens of seconds, and the extended effects over the time course of minutes, which recovered after about one hour. Even though the activity of most neurons were drastically reduced, a small number of neurons exhibited striking elevations in intracellular calcium. While the functional relationship between the intracellular Ca^{2+} changes at both the modulatory and synaptic time scales is unclear, future studies using Ca^{2+} imaging will likely establish their role in the manifestation of blast pathology.

At a population level, we found an overall loss of Ca^{2+} activation events in the hippocampus after blast, suggesting that blast led to a network state where the neurons are less active. This reduced activity may be related to the temporary loss of memory or confusion often observed in patients experiencing head trauma [126]. Future Ca^{2+} imaging studies may provide important links to the mechanisms underlying memory deficits related to head injuries.

3.4.4 Potential causes of the mTBI induced changes in intracellular Ca^{2+} levels

Blast-induced changes in sustained basal intracellular Ca^{2+} levels on the order of minutes to tens of minutes are indicative of modulation of biochemical, cellular signaling cascades, whereas the change in the frequency of sub-second Ca^{2+} transients is suggestive of altered spiking patterns that are likely associated with changes in membrane biophysics or synaptic mechanisms. While the sub-second transient Ca^{2+} changes can be explained by changes in neuronal activity patterns, it is still unclear how blast induces sustained shifts in basal intracellular Ca^{2+} level. It is possible that the reduction in basal intracellular Ca^{2+} levels could arise from spreading depression [127]. However, this does not seem likely in that a small number of cells with increased Ca^{2+} levels were interspersed with those with decreased Ca^{2+} levels.

While many studies indicated that blast induces a long-term increase in intracellular Ca^{2+} levels over the course of days [128]–[131], a recent study also showed immediate suppression of neuronal activity lasting for 5 to 20 minutes followed by increased cortical activity by two hours post injury upon sustained cortical compression in barrel cortex[132]. Our results showed an overall suppression in a large fraction of the neuronal population immediately after the blast within an hour, indicating blast injuries could cause a dramatic shift in the Ca^{2+} level on various time-scales. The suppression and the increase in Ca^{2+} levels are likely due to distinct cellular mechanisms. For example, it has been suggested that there can be a switch in AMPA receptor composition from Ca^{2+} impermeable glutamate receptors (GluRs) to Ca^{2+} permeable GluR receptors lacking GluR2 following mechanical injury in cortical neurons *in vitro* [133], [134], which could explain the long-term increase in basal levels of intracellular Ca^{2+}. In contrast, it has also been suggested that there is a decrease in GluR1 expression in the cortex 15 minutes after closed head injury [135], that could lead to the acute suppression of intracellular Ca^{2+} observed here. Furthermore, long-lasting loss of Ca^{2+} permeable glutamate NMDA receptor function, following short-lived (<1 hour) hyper-activation may also contribute to the reduction in intracellular Ca^{2+} [136]. In a lateral fluid percussion model in the hippocampus there was decreased net synaptic efficacy and reduced excitatory postsynaptic potentials in CA1 while both evoked and spontaneous miniature inhibitory potentials were larger in injured brains [137]. These results suggest that increased activation of NMDA receptors and Ca^{2+} permeable AMPA receptors may be responsible for the long-term increased basal Ca^{2+} levels that has been reported previously, while enhanced spontaneous inhibitory activity in area CA1 following blast may cause the immediate reduced levels of Ca^{2+} as we observed. It is also possible that direct alterations in $GABA_A$ receptors may contribute to inhibitory dysfunction after trauma [138].

Interestingly, a recent *in vitro* study has shown that simulated blast primarily affects calcium signaling in human astrocytes, in contrast to neurons, producing calcium waves that propagate through astrocytic networks via purinergic signaling [139]. This suggests that astrocytes may also play a significant role in modulating Ca^{2+} levels in response to blast. It also raises the possibility that astrocytes may be involved in our present results even though we found no pathological changes in astrocytes. The imaging methods and reagents employed in the present study could easily be adapted to study blast induced changes in Ca^{2+} in astrocytes.

In addition to these potential synaptically-based mechanisms, it is also possible that changes in the homeostatic regulation of Ca^{2+} may be involved in the changes in basal Ca^{2+} levels. Homeostatic regulation of Ca^{2+} in response to TBI has been shown to occur by a wide variety of mechanisms including: voltage and receptor activated Ca^{2+} channels; Ca^{2+}

transporters; release and sequestration of Ca^{2+} from intracellular stores in the nucleus, mitochondria and endoplasmic reticulum; intracellular Ca^{2+} binding proteins; and changes in the permeability of neuronal membranes to Ca^{2+} [140]. Changes in any of these homeostatic mechanisms could influence both the basal and sub-second transient Ca^{2+} changes in response to blast.

Quantitative analysis indicated that there was a complex relationship between the slower modulatory changes in basal Ca^{2+} levels and the sub-second scale Ca^{2+} dynamics. For example, cells with increased modulatory cytoplasmic levels of Ca^{2+} could have either increased, decreased or unaltered levels of presumptive synaptic Ca^{2+} activity at the millisecond time scale. These different responses indicate there are multiple neuronal types and synaptic circuits being influenced by blast and that several different signal transduction pathways are involved. Given that only a small population of hippocampal neurons had increased cytoplasmic levels of Ca^{2+} in response to blast, it will be important for future studies to determine why these neurons are unique. Further characterization of the specific cell types involved, their synaptic properties, and the signal transduction pathways being affected could form the basis for future treatments to prevent or treat neuronal blast injury. Given that synaptic processing requires a precise functional balance of inhibition and excitation, the increased and decreased levels of basal Ca^{2+} we see in response to blast may produce overall changes in network functionality. These changes in intracellular Ca^{2+} and their related signaling pathways may underlie the immediate cognitive effects of blast exposure, and contribute to longer term anatomical pathologies.

3.5 Methods

3.5.1 Blast model

The blast injury model used was adapted from the previously developed Cranium Only Blast Injury Apparatus (COBIA) [101]. The central component of the COBIA was a Mastershot (a 22 caliber, single-shot, powder-actuated tool, Ramset RS22; ITW Ramset, Glendale Heights, IL) mounted vertically on a custom-fabricated stand. The Mastershot was modified by removing the piston that normally drove the fastener, making it function like a firearm allowing the blast wave to propagate undampened through the barrel (Figure 6B). The muzzle of the Mastershot was snugly fit into a custom blast director, constructed from polyvinyl chloride pipe (10 cm long with an inner diameter of 2cm), (Figure 6B). The blast wave was generated by firing a 22-caliber crimped brass blank cartridge (power hammer loads power level 4, yellow color coding, with 179 ± 5mg of smokeless powder, Ramset 42CW, Ramset, Glendale Heights, IL).

3.5.2 Blast wave measurement and calibration

A precision dynamic high frequency piezoelectric pressure transducer (Model: 113B21 High Frequency ICP® pressure sensor, PCB Piezotronics, Inc., Depew, New York), powered by a power supply (Model 5421, Columbia Research Laboratories, Inc., Woodlyn, PA), was used to measure the pressure of the blast waves produced by the COBIA (Figure 6C). The sensor was positioned approximately 2 cm from the dissipation chamber, where the head of the mouse was positioned. Transducer outputs were digitized using a NADAQ data acquisition system (National Instruments, NI-USB-6259) at 350 kHz, and analyzed offline.

We calibrated our COBIA device using this sensor which had a 500 kHz resonant frequency (100 kHz maximum sampling frequency). To compare to the pressure measurements reported in Kuehn et al. (2011), we filtered the pressure trace at 12 kHz to measure a comparable transient overpressure [101]. To compare to the shock tube device reported by Goldstein et al. (2012), we filtered the blast pressure trace at 2 KHz [98]. While the severity of blast injury is typically attributed to the magnitude of the pressure produced (peak blast overpressure), and the duration of peak overpressure [93], [100], [101], [107], none of the animals exposed to blast lost consciousness or exhibited noticeable abnormal behavior immediately following blast nor the week after. In addition, upon dissection, the brains were unremarkable with no contusions. Due to the similarities of the blast overpressure in this study with prior studies, we consider results of this study most relevant to mild blast injury [98], [101].

3.5.3 Wide-field imaging and blast procedure

All animal procedures were approved by the Boston University Institutional Animal Care and Use Committee. Nine adult female C57BL/6 mice (Taconic; Hudson, NY) 2-12 months old at the start of the experiments were imaged as described previously [20]. Briefly, under isoflurane anesthesia, mice were stereotaxically injected in CA1 (AP: –2 mm, ML:1.4 mm, DV: –1.6 mm) with 0.25µL of AAV9-Syn-GCaMP6f.WPRE.SV40 virus (titer~6e12 GC/ml, University of Pennsylvania Vector Core) using a microsyringe pump (UltraMicroPump3-4; World Precision Instruments, Sarasota, FL) at a speed of 40nl/min. Upon complete recovery (at least 5 days), animals were then surgically implanted over the CA1 viral injection site with a custom imaging window constructed using a stainless steel cannula (OD: 0.317 mm, ID: 0.236 mm, height, 2 mm) adhered to a coverslip (size 0; OD: 3mm), and a custom aluminum headplate to allow awake head fixed imaging. Upon complete recovery from implant surgery (approximately 2 weeks), mice were accustomed to head fixation before imaging sessions began (Figure 6D).

Awake, head-fixed animals were imaged using a custom-built fluorescence microscope as previously described (Figure 6A) [20]. Briefly, the imaging setup consisted of standard optics for GCaMP6 imaging and a scientific CMOS (sCMOS) camera (ORCA-Flash4.0 LT Digital CMOS camera C11440-42U; Hamamatsu, Boston, MA). Imaging data (1024x1024 pixels, 16bit) was collected at 20 Hz and analyzed offline. No anesthetics or analgesics were used for any of the blast or imaging protocols.

Mice were first imaged for 100 seconds to obtain baseline activity prior to blast, and then removed from the imaging setup and inserted into a mouse restrainer (Stoelting Co. Wood Dale, IL) that permitted full mobility of the head (Figure 6B). For the blast group (n=4 mice), restrained mice were placed 2 cm under the blast dissipation chamber and positioned so that the blast was directed dorsally between Bregma and Lambda. For the sham group (n=5 mice), restrained mice were positioned adjacent to the COBIA, so that mice experienced the sound of the blast but not the blast pressure. Prior to blasts, tape was placed over the imaging cannula and a wetted custom paper cone was fitted to cover the head to allow reproducible positioning of the head, to allow free movement of the head, and to prevent potential quaternary damage from gun powder during blasts. Immediately following blasts, animals were removed from the restrainer and quickly repositioned and head-fixed in the imaging setup. This transfer process typically took less than 5 minutes. Calcium imaging was then performed for 100 seconds for all mice in each of the following intervals: immediately following head-fixation after blast (0 minutes), and at approximately 10 minutes (Range: 6-15m, Mean: 10m 45s), 20 minutes (R: 16-26 min, Mean: 21m 19s), 35 minutes (R: 29-46 min, Mean: 35m 32s), and 65 minutes (R: 57-76 min, Mean: 65m 28s) after blast/sham (Figure 6E). Each animal underwent these procedures once a day for two consecutive days.

3.5.4 Calcium imaging data analysis

For each imaging session, the 100-second videos for the five time points following the blast/sham-exposure (0, 10, 20, 35, and 65 minutes after blast/sham-exposure and head re-fixation) were first concatenated, and then processed as one video (500-second total duration) to provide a continuous registration of regions of interest (ROIs) across all time points. Each of the 100-second baseline videos taken immediately prior to blast or sham-exposure was processed separately, because it was difficult to accurately align the ROIs between the videos taken before and after the blast, when the mice were transferred from the imaging setup to the COBIA device. Ca^{2+} imaging videos were first filtered with a homomorphic filter to enhance contrast, and then motion corrected using a rigid correction as previously described [20]. Circular ROIs with a radius of 6 pixels (corresponding to 7.8 microns) were manually selected as being centered on the cell body on a maximum projection image across all video frames using a code we developed (https://github.com/HanLabBU/mTBI_Ca_Hippocampus).

Raw calcium traces were extracted for each identified ROI as the mean intensity of all pixels within a given ROI, where the absolute value of each pixel intensity was determined from the motion corrected videos without the homomorphic filter. The raw calcium intensity for each cell was used to determine whether a cell was elevated or suppressed. A probability density estimate (PDE) of raw pixel intensities was calculated using MATLAB 8.1 (MathWorks Inc., Natick, MA, 2013) for each cell for the imaging periods immediately after blast (Period-1) and 65 minutes (Period-5) after blast. The difference in mean pixel intensity between Period-5 and Period-1 for each cell was calculated. To establish a confidence interval, pixel intensity differences were pooled across all sham mice for all imaging sessions. A 95% confidence interval was determined from the 0.025 and 0.975 quantiles of these pooled differences. The width of this confidence interval was applied to the unity line, which would suggest no difference between Period-1 and Period-5. Differences in mean pixel intensity that fell outside of this confidence interval for both blasted and sham-exposed mice were classified as elevated (Period-1 > Period-5) or suppressed (Period-1 < Period-5).

For additional analyses, we also calculated normalized Ca^{2+} traces as $\frac{\Delta F}{F_5} = \frac{F-F_0}{F_5}$, where F is the linearly detrended instantaneous fluorescence intensity, F_0 is the linearly detrended mean fluorescence for a given imaging period, and F_5 is the mean fluorescence for the final imaging period (Period-5, ~65 minutes after blast). Binarized traces were then created from the normalized traces by setting the rising phase of calcium activation events to 1s, with 0s elsewhere along the binary trace. Specifically, normalized Ca^{2+} traces ($\frac{\Delta F}{F_5}$) were low-pass filtered with a 6th order Butterworth filter at a cutoff of 2 Hz. A global standard deviation was calculated across all concatenated videos (SD_{all}) for each trace.

Calcium activation events were identified as peak values that were at least $3*SD_{all}$ above the mean for each imaging period. Each of these peaks was counted to determine an integer value of the calcium event rate. From each peak point, the data points prior to the peak with a positive derivative were set to a binary 1, with all other data points were assigned as 0s. To determine if a cell showed a significant decrease or increase in dynamic activity after blast, a bootstrapping method was used. The percentage of time a cell was active was measured during a 10 second window that was randomly permuted 1000 times from the trace over the course of each period to determine how active the cell was for that time period. These bootstrapped samples for period-1 and period-5 were compared for each cell using a two-tailed Wilcoxon Rank Sum test. Cells that were statistically different ($p<0.05$) between the two time periods were classified as showing increased activity or decreased activity, where decreased cells were those with less activity in period-1 than period-5, and increased cells were those with more activity in period-1 than period-5.

Each cell was determined to be either suppressed, elevated, or consistent in its basal levels, as well as determining whether the calcium event rate was increased, decreased, or non-modulated by comparison of time period 1 to time period 5 for each cell. Each of these classifications was quantified as the fraction of total neurons within each mouse, and those values were used for population analyses between sham and blasted mice.

3.5.5 Immunocytochemistry

One week following the second blast, mice were perfused with 0.9% NaCl heparinized saline followed with 4% paraformaldehyde in 0.1M phosphate buffer (PB) pH 7.4 (containing sodium phosphate monobasic (Sigma, Cat# S0751), and sodium phosphate dibasic (Sigma, Cat# S3264). Brains were post-fixed overnight at 4˚C, and then cryoprotected in 30% sucrose in PB overnight at 4˚C. Brains were then blocked from Bregma -0.94mm to -2.92mm using an adult mouse brain slicer matrix (BSMAS001-1, Zivic Instruments, Pittsburgh, PA), and sectioned at 40µm using a freezing sliding microtome (Reichert Jung Inc. Depew, NY). Brain slices were stored at -20˚C in cryoprotectant ((containing 30% sucrose (Sigma, Cat#S0389), 30% ethylene glycol (Fisher Scientific, Cat#BP230-1), 1% polyvinylpyrrolidone (Fisher Scientific, Cat#BP431-500)) in Tris-buffered saline pH 7.6 ((0.4M Trizma HCl, (Sigma, Cat# T-3253), 0.01M Trizma base, (Sigma T-1503), 0.15M sodium chloride, (Fisher Scientific, Cat# BP358-212)) for subsequent immunostaining.

Free floating sections were first mounted and dried onto Colorfrost Plus slides (Fisher Scientific, Waltham, MA). Mounted slices were rehydrated in PB prior to incubation with 5% normal donkey serum (Jackson ImmunoResearch Laboratory, Inc. West Grove, PA) in PB containing 0.3% TritonX100 (PBTx). Slices from each animal were immunostained overnight at 4°C using either mouse monoclonal anti-glial fibrillary acidic protein (GFAP 1:250, Clone No. N206 A/8, UC Davis/NIH NeuroMab Facility Cat# 75-240, RRID:AB_10672299), or rabbit anti-Iba1 (1:1000, Wako, Catalog No. 019-19741), followed by the appropriate fluorescently conjugated secondary antibodies, donkey anti-mouse Cy3 (1:500, Jackson Immuno Research, Catalog No. 715-165-150) or donkey anti-rabbit 647 (1: 500, Jackson Immuno Research, catalog No. 711-605-152), for two hours at room temperature. These primary antibodies have been previously characterized in mouse brain [141], [142]. Slices were then coverslipped in Gelvatol ((10% polyvinyl alcohol, (Sigma, Cat#P8136), 20% glycerol, Sigma G-9012, 0.02% sodium azide, (Fisher Scientific, Cat#-227-100), 0.2M Tris (Amresco, Cat#0497), pH 8.5)) or Vectashield with DAPI (4'6-diamindino-2-phenylindole) (Vector Labs, Burlingame, CA) to visualize nuclei.

Sections were imaged using a Nikon Eclipse motorized microscope (Nikon Instruments, Inc.) at 10x. ImageJ software (National Institutes of Health, Bethesda, Maryland, USA) was used to analyze the stained slices.

3.5.6 Immunocytochemistry quantification

The percent area occupied by GFAP was analyzed using ImageJ software. Immunostained images were first inverted so that signal appeared black and then binarized using the isodata algorithm in ImageJ. Five randomly selected cells per slice, and three slices per hemisphere with visible somata were analyzed for each mouse. An area large enough to enclose a single cell was used for all analyses. The area fraction, defined as the percent coverage (percent area) of immunoreactivity within each area, was obtained for each binary image using the area fraction selection from the ImageJ Measure plugin. It was expected that evidence of glial activation would be reflected by a greater percent area because the cells would be larger in size and therefore occupy a greater percentage of the area. Values for percent area were obtained for individual cells (n=5 cells per hemisphere). To account for any differences due to the presence of the imaging window (ipsilateral), the hemisphere opposite to the window (contralateral) was analyzed separately as an internal control.

Two broad classifications of Iba1 phenotypes were chosen for evaluation: ramified and non-ramified. Manual counts of Iba1 positive cells identified as ramified or non-ramified were performed within the same ROI applied to the hemisphere ipsilateral to the imaging window as well as the contralateral hemisphere.

GFAP and Iba1 immunoreactivity were first evaluated using a paired t-test ($p<0.05$) for the ipsilateral and contralateral hemispheres for sham ($n=5$) and blast exposed ($n=6$) animals. A two-tailed unpaired t-test ($p<0.05$) was then performed to compare the results from sham and blasted animals. Data are presented as mean ± standard deviation. Statistical analysis of immunocytochemistry was performed using SPSS (IBM Corp. Released 2016. IBM SPSS Statistics for Windows, Version 24.0. Armonk, NY: IBM Corp.)

3.6 Supporting Information

3.6.1 Supplemental Videos

Supplemental Video 1. Blast led to acute changes in basal intracellular Ca^{2+} levels and transient Ca^{2+} event rates in individual hippocampal neurons, and the changes slowly recovered after about one hour.

Raw microscopy video data is shown for one example blast session. The appropriate time period with respect to the blast is shown in the bottom left corner, with blank black frames artificially inserted to demarcate the time between imaging sessions. A dramatic change was observed immediately following the blast that seemed to slowly recover within one hour. For display purposes, only the first 25 seconds of each session is shown and the video is sped up by 4-times its original speed. All frames are scaled to the same contrast intensity for all videos.

Supplemental Video 1 can be accessed at:

https://www.liebertpub.com/doi/suppl/10.1089/neu.2017.5029/suppl_file/Supp_Video1.zip

Supplemental Video 2. Sham, noise-exposure did not alter intracellular Ca^{2+}dynamics in the hippocampus.

Raw microscopy video data is shown for one example sham-blast session. Noise-exposure produced little changes in intracellular calcium dynamics. Videos were processed identically as in supplemental video 1, with only the magnitude of the contrast scaling factor being adjusted for the inherent fluorescent differences observed between mice.

Supplemental Video 2 can be accessed at:

https://www.liebertpub.com/doi/suppl/10.1089/neu.2017.5029/suppl_file/Supp_Video2.zip

CHAPTER 4 – DISTINCT NEURONAL POPULATIONS CONTRIBUTE TO TRACE CONDITIONING AND EXTINCTION LEARNING IN THE HIPPOCAMPUS

4.1 Abstract

Trace conditioning and extinction learning are two learning processes that depend on the hippocampus. Previous studies have suggested that distinct neuronal populations contribute to fear conditioning and extinction in both the hippocampus and amygdala. In this study, we present the first evidence that two populations of cells in CA1 of the hippocampus contribute to trace eye-blink conditioned learning and extinction of that conditioning, and that neuronal extinction responses can be observed in the hippocampus in less than 6 consecutive extinction presentations.

Using trial-averaged neuronal responses, we observed neurons that consistently, but sparsely responded to a conditioned stimulus (CS) over multiple days of learning a trace conditioning task, and a different population of cells that responded to the CS during extinction learning. The ability of individual cells to encode CS presentations on a sparse number of trials suggests that network or population responses are critical for the encoding of learning and memory in CA1. To this end we developed a method to quantify network responses of co-active neurons, and found that subpopulations of neurons responded on significantly more trials with the correct behavioral response than with the incorrect behavioral response for both the last trace eye-blink conditioning session and extinction session. These results suggest an important role for distinct populations of neurons that encode information about the CS within the hippocampus.

4.2 Introduction

Many studies have revealed that the hippocampus is critical for learning and memory in animals and humans. Early surgical lesions of the hippocampus in human patients, designed to alleviate intractable epilepsy, resulted in severe memory loss and an inability to form new declarative or episodic memories [33], [34]. Hippocampal atrophy is also associated with diseases related to memory loss and cognitive decline including dementia and Alzheimer's disease [35]–[39]. Many subsequent studies have highlighted that the hippocampus is specifically important for spatial, contextual, and associative learning in a variety of animal models [143], [144].

Various experimental paradigms have been devised to probe hippocampal specific forms of learning and memory. One such well-established paradigm is trace eye-blink conditioning which requires an intact hippocampus [50], [51]. In this experimental design, subjects are presented with a conditioned stimulus (CS) such as a tone or light that reliably predicts an unconditioned stimulus (US), such as a puff of air delivered to the subject's eye. In trace eye-blink conditioning, the CS and US are separated temporally by a memory trace interval. Over time, subjects learn to associate the CS with the US [52]–[56]. Both nicotinic and muscarinic acetylcholine receptors (AChRs) are critical for the acquisition of trace eye-blink conditioning [145]–[147], and NMDA mediated plasticity is required for trace eye-blink conditioned learning [148].

Another type of learning that requires the hippocampus is context dependent extinction learning [50]. Extinction learning is traditionally considered new-learning that overrides a previously learned relationship. In the example of trace eye-blink conditioned extinction learning, this would correspond to the association that a previously established CS is no longer predictive of a subsequent US. Extinction learning can be tested after trace eye-blink conditioning by removing the US after CS presentations, and monitoring the strength or presence of a behavioral or conditioned response (CR). As new learning occurs, animals will suppress the CR to the previously predictive tone or light. Extinction learning has also been shown to be NMDA receptor dependent for operant learning [57], and requires the involvement of hippocampal inhibitory neurons for context-related extinction [149] and adult neurogenesis for fear extinction [150].

While the hippocampus and NMDA dependent plasticity have been implicated in both trace conditioning and extinction learning, it remains largely unknown how individual hippocampal neurons selectively participate in trace eye-blink conditioning and extinction learning. Two distinct functional populations tied to fear conditioning and extinction have been reported in the amygdala [151], supporting the idea that trace conditioning and extinction learning involve distinct learning processes which likely involve different mechanisms supported by different neurons. While segregated populations of hippocampal neurons upregulate different genes for both fear conditioning and context dependent fear extinction [152], it remains unknown how ongoing neuronal activity changes for individual neurons during trace eye-blink conditioning and extinction learning, and how these two types of learning processes might engage specific factors at the neuronal population level.

In order to address these questions, we performed calcium imaging of individual CA1 neurons over multiple days during the course of trace eye-blink conditioning, followed by extinction learning for that eye-blink task. Calcium imaging using genetically encoded calcium sensors allows us to measure hundreds to thousands of neurons simultaneously with single-cell resolution [20], [153]. We chose eye-blink trace conditioning because it allows us to track the development of neuronal responses recorded in CA1 of the hippocampus across multiple days and multiple sessions [20], [153], unlike fear trace conditioning, where the learning often occurs in a small number of trials. We found that a significant fraction of CA1 neurons showed task related responses for both trace eye-blink conditioning and extinction learning. However, the identities of the cells that contributed to each type of learning differed between eye-blink conditioning and extinction, suggesting two functionally distinct subpopulations of cells within the hippocampus. To further understand how the neuronal populations reflect learning, we developed a classification method that allowed for reliable identification of task related neuron populations. Additionally, we show that neurons that are co-active during the correct behavioral context are significantly more active than they are in the incorrect behavioral context. This discretization and quantification method is particularly useful for data sets where responses evolve rapidly, like learning, and are not conducive to averaging an analog signal across a large number of trials for applying correlation analysis.

4.3 Results

4.3.1 Conditioned responses increase across training days in a classical eye-blink task

Trace conditioning experiments were performed in head-fixed mice (n=5 mice) that were positioned under a custom-built wide-field microscope (Figure 12A) as previously described [20]. Neuronal activity was monitored using GCaMP6f to closely track neuronal spiking events [71], [74], [86], [102]–[104], in combination with a scientific (sCMOS) camera for wield-field imaging of hundreds of neurons simultaneously.

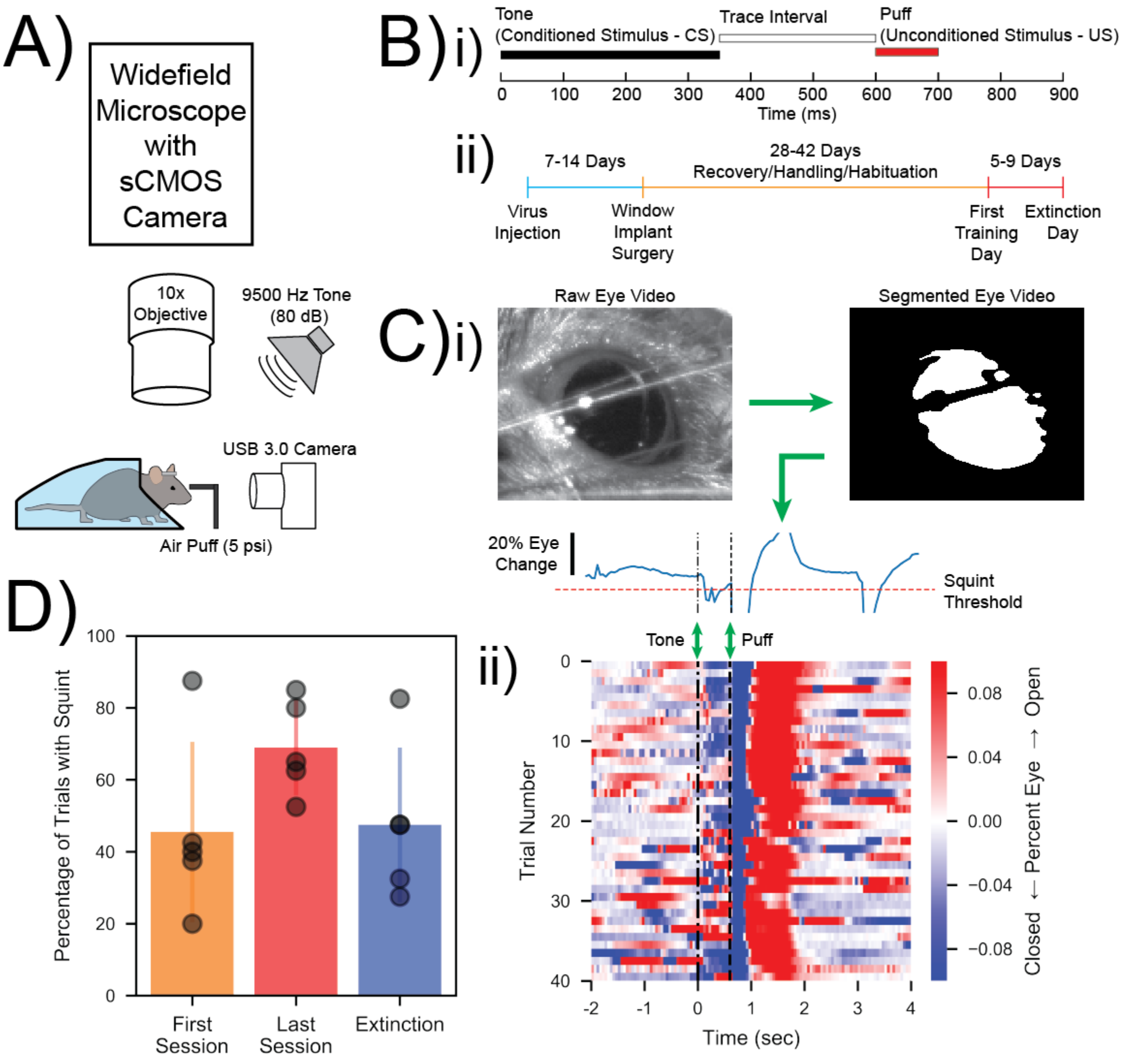

Figure 12. Experimental design and measurement of animal behavior for trace conditioning task

(A) Imaging and behavioral setup. The imaging setup consisted of a microscope with a sCMOS camera, standard wide-field fluorescence optics, and a 10x long working distance objective to image a head-fixed mouse. For the behavioral paradigm, a speaker was positioned near the mouse and a cannula for directing an air puff was placed in front of the right eye. Eye responses were monitored using a USB 3.0 Camera. **(Bi)** Within trial design. Trials consisted of a 350 ms tone as the conditioned stimulus (CS) followed by a 250 ms trace interval with no sound, after which a 100 ms puff of air was delivered to the eye of the animal as the unconditioned stimulus (US). **(Bii)** Experimental timeline. Each animal was injected with GCaMP6f virus, allowed 1-2 weeks for virus expression before surgical window implantation above CA1 in the hippocampus. The first training session was 4-6 weeks after the surgery, and animals were recorded for 5-9 days before the extinction recording session. **(Ci)** Video eye monitoring and behavioral assessment. Raw eye monitoring videos were segmented using Fiji [154] and MorphoLibJ [155] to measure eye traces over time. Eye movement thresholds were calculated for each recording and used to classify whether the mouse eyelid moved or not between the CS and the US. **(Cii)** Extracted eye traces and movement intensity. Eye trace for all 40 trials of one last training session from one example mouse. Red corresponds to eye opening, while blue corresponds to eye closure. A clear blue band is seen after the puff on each trial, while some trials show squinting after the tone, but before the puff. **(D)** Quantification of behavioral responding for all subjects. The last session of training had the highest level of eye movement behavior on average across mice, while behavioral responding after extinction was reduced again to levels comparable to the first session of training.

Prior to imaging, mice were injected with GCaMP6f virus and implanted with a custom window cannula that allowed imaging of dorsal CA1. Following surgery, mice were given 4-6 weeks for recovery from surgery that included a period of experimenter handling and exposure to the head fixation. Following head-fixed habituation, mice were trained on a classic trace-eye conditioning paradigm for 5-9 days (Figure 12Bii). The paradigm consisted of a predictive 9500 Hz tone as a conditioned stimulus (CS) followed by a gentle 100 ms long puff of air to one eye as an unconditioned stimulus (US). The 350 ms long CS was separated from the US by a 250ms trace interval (Figure 12Bi). Eye behavior was monitored with a USB 3.0 Camera. On the first day of recording, animals were given 20 tone presentations alone as a measure of responsivity of calcium activity and the strength of eye blink conditioned responding (CR) to the sound alone. Animals were subsequently given 60-80 tone-puff trials per day with individual trials separated by 35 ± 5 seconds. On the final session of conditioning, animals were given 20-40 CS-US conditioning trials followed by 40 sound alone extinction trials where the CS was not followed by the US (Figure 12Bii).

The strength of the behavioral response was quantified by segmenting the eye videos and averaging each frame to calculate eyelid movement (Figure 12Ci). A movement threshold was calculated for each eye trace, assuming a constant average eye size (see methods). This thresholding method provided a consistent calculation of eye closure for each session across mice. Each trial was classified as a "correct trial" if the eye-trace conditioned response went below the calculated threshold, termed a squint, after the tone and prior to the puff. The same classification was used for extinction trials except in this context a conditioned response would be considered an "incorrect trial". The strength of squint response to the CS and the subsequent full blink response to the US on each trial could be clearly delineated and quantified using this method (Figure 12Cii). Compared to the first day and extinction sessions, the squint response to the CS after several days of training was much larger (Figure 16). Behavior was measured and scored according to this metric across mice, with animals consistently showing more conditioned squint responses on the last session of training (69 ± 13%, mean ± s.d.) compared to the first session (46 ± 25%, mean ± s.d.) or the extinction session (48 ± 22%, mean ± s.d.) (Figure 12D). There is a clear trend of behavioral improvement over days of training, that decreases on the extinction day, though the differences between these behavior scores were not significant when corrected for multiple comparisons (one-tailed paired t-test, alpha=0.025 after Bonferroni correction, p-values=0.033 & 0.077).

4.3.2 Trial-averaged calcium dynamics in CA1 reflect the strength of behavioral responses during trace conditioning

Imaging the hippocampus during trace conditioning allowed us to understand how large neuron populations (409 ± 243 cells, mean ± s.d.) are altered across multiple days of learning. Further we could identify the proportion of neurons recruited by each aspect of learning and test whether conditioning and extinction recruit unique cell populations or repurpose the same neuronal population. Videos were motion corrected, a projection image was generated across each video, and cells were segmented using a semi-automated software to extract temporal traces across imaging sessions (Figure 13A). Identified cells underwent processing steps to remove cross-contamination between neighboring cells and were normalized with their baseline fluorescence at zero.

A distinct pattern of hippocampal neuronal responses emerged after multiple days of trace conditioning. From a behavior standpoint, the percentage of trials with conditioned squint responses increased between the first and last session of training and animals tended to string together more consecutive response trials on the last training session than the first training session (Figure 13Bi). Additionally, when looking at the trial averaged neuronal responses sorted by average response intensity between the tone and puff, multiple days of training resulted in more neurons showing a calcium increase between the tone and puff than on the first session of training (Figure 13Bii). When quantified as an average increase in calcium between the tone and puff, 12.5 ± 5.6% (mean ± s.d.) of cells responded on the last training session, which was significantly more than the 3.6 ± 1.4% (mean ± s.d.) of neurons responded on the first session of training ($p<0.05$, one-tailed paired t-test, Figure 13Di). This percentage of cells for first session was also not significantly different than the chance value of 4.0 ± 0.8% (bootstrapped estimation: $N=1000$, $p=0.311$, one-tailed bootstrap, $alpha=0.05$), while the last session was significantly different from the chance value of 7.0 ± 1.4% (Figure 13Dii, $N=1000$, $p=0.001$, one-tailed bootstrap, $alpha=0.05$).

These findings suggest that the number of neurons encoding the conditioned stimulus gradually increase over time after multiple days of training (Figure 13Biii).

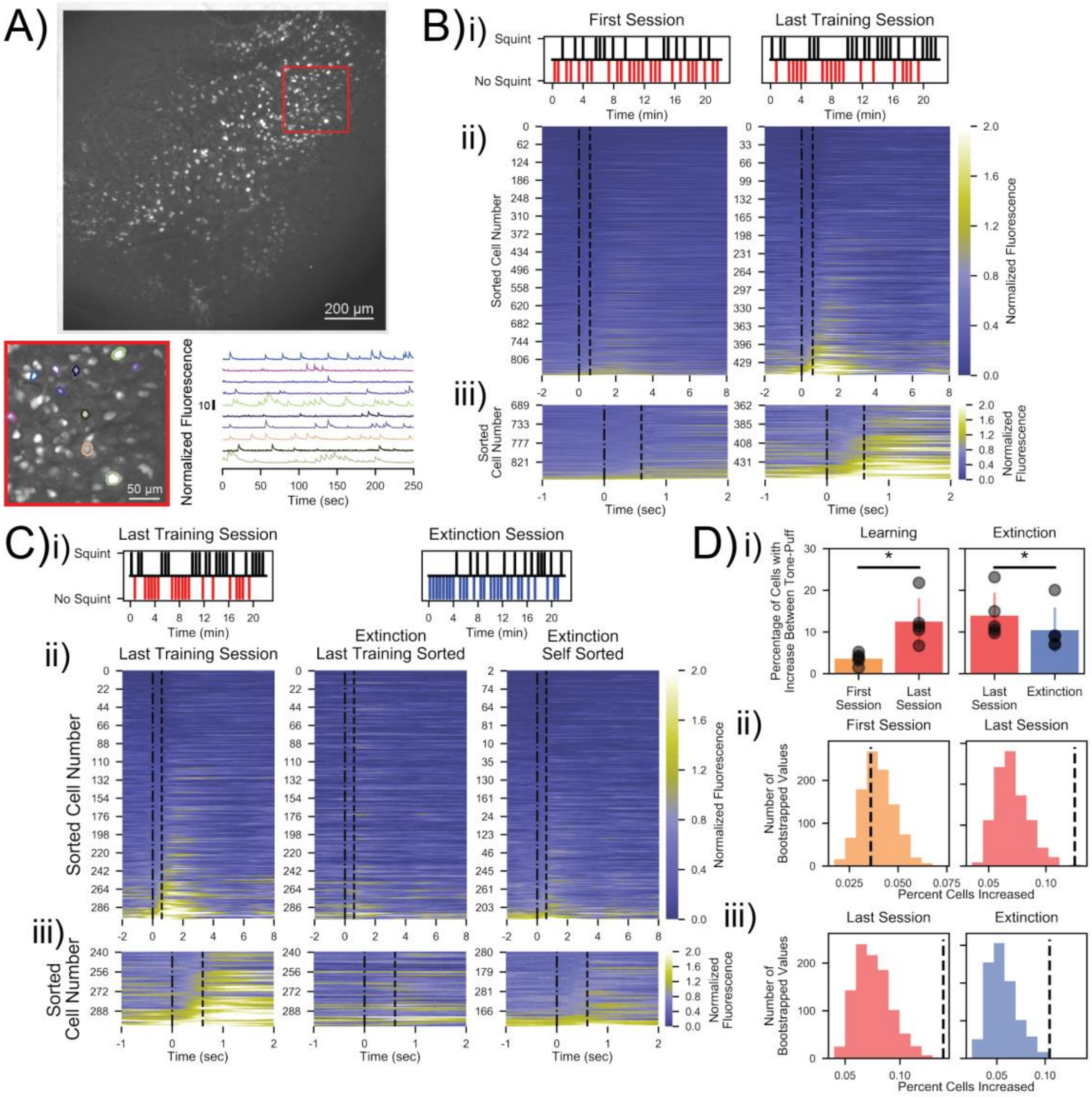

Figure 13. Calcium imaging responses track behaviorally relevant environmental stimuli following learning

(A) Full-field calcium activity and extracted traces. Maximum-minus-minimum projection for one motion corrected video to show example field of view over several hundred cells. Inset show several selected cells and their corresponding normalized fluorescence trace recordings for a subset of a recording session. **(Bi)** Measures of behavioral responding across training sessions. Behavior responses were classified as squint or no squint for the first and last recording sessions from a representative mouse. **(Bii)** Trial-averaged recordings sorted by average fluorescence between the tone and puff from the first and final CS-US conditioning training session. The dash-dot line represents tone onset, while the dashed line represents puff onset. **(Biii)** Zoomed inset of bottom 20% of cells for each recording session. More cells showed a consistent trial-averaged response for the last recording session than during the first recording session, as seen by the yellow bands between tone and puff on the last training session. **(Ci)** Behavior responses from final conditioning session and extinction sessions. Note animals show fewer squint events during extinction sessions. **(Cii)** Trial-averaged recordings of the last training session and extinction session, sorted by the average fluorescence between tone and puff. After sorting the cells for the last training session, that sorting was maintained to look at the spatially matched cells during the extinction session, revealing a reduction in tone-puff responses from CS responding neurons. Resorting for the extinction session alone shows a new population of cells responsive to the extinction session. Dash-dot line represents tone onset, while dashed line represents puff onset. **(Ciii)** Zoomed inset of bottom 20% of cells for each session. **(Di)** Quantification of the proportion of cells responsive to the CS from the first session (orange), the final CS-US training session (red), and the extinction day (blue), $^*p<0.05$, paired one-sided t-test. **(Dii)** Bootstrapped distributions of the percentage of cells with an increase between the tone and puff after circularly shuffling the tone-puff locations 1000 times. Dashed black line shows percentage measured with the non-shuffled tone-puff locations. **(Diii)** Bootstrapped distributions comparing the matched last session and extinction session recordings.

4.3.3 Extinction learning rapidly recruits a new population of neurons for memory encoding in CA1 of the hippocampus

Cells imaged during the last training session included both CS-US training and extinction, allowing all cell identities to be matched between sessions. Behavioral analysis revealed that conditioned squint responses were substantially reduced as a result of extinction training (Figure 13Ci). Interestingly, when we compared the responses of individual cells to the tone after matching cell identities between conditioned trials and extinction trials, we discovered that the majority of neurons most responsive to the tone did not consist of the same populations (Figure 13Cii). Resorting the population for extinction revealed that tone responsive neurons from extinction trials largely reflected a novel population of cells that were not responsive to the tone previously (Figure 13Ciii). Extinction neurons represented 10.5 ± 5.5% (mean ± s.d.) of cells, which was a statistically smaller proportion of the population relative to the 14.0 ± 5.5% (mean ± s.d.) of neurons that were CS positive responding cells from the final CS-US training session ($p<0.05$, one-tailed paired t-test, Figure 13Di). However, both populations were greater than would be expected to respond by chance, with values of 7.6 ± 1.6% for the last conditioning session and 5.6 ± 1.6% for the extinction session (Figure 13Diii, both: N=1000, one-tailed bootstrap, alpha=0.05, Last Session p=0.001 | Extinction p=0.005). Of the conditioned stimulus (CS) cells that were strongly responsive to the CS on the final training session prior to extinction, 70.4 ± 11.7% (mean ± s.d.) lost their strong responsiveness after extinction training began. In contrast, 60.9 ± 9.8% (mean ± s.d.) of extinction (EX) cells did not respond during trace conditioning, and were only responsive to the tone presentation during extinction.

4.3.4 Memory coding for both trace conditioning and extinction arises from both spatially and temporally distributed populations of neurons

We next considered the reliability of individual cell activation with regards to the tone and their anatomical relationship to one another. CS cells individually responded to only 13.2 ± 5.6% (mean ± s.d.) of trials (Figure 14A), while EX cells only responded to 11.6 ± 2.3% (mean ± s.d.) of CS presentations during extinction training (Figure 14C). Interestingly, the maximum number of trials that a CS single neuron responded to ranged from 20-78% of trials across all mice (46.5 ± 22.9%, mean ± s.d., n=5 mice). For extinction, the maximum number of trials that a single cell responded to ranged from 18-63% of trials (34.5 ± 17.6%, mean ± s.d.). Additionally, both CS responsive cells (Figure 14B) and EX responsive cells (Figure 14D) were both heterogeneously distributed across CA1 without any strong anatomical spatial clustering.

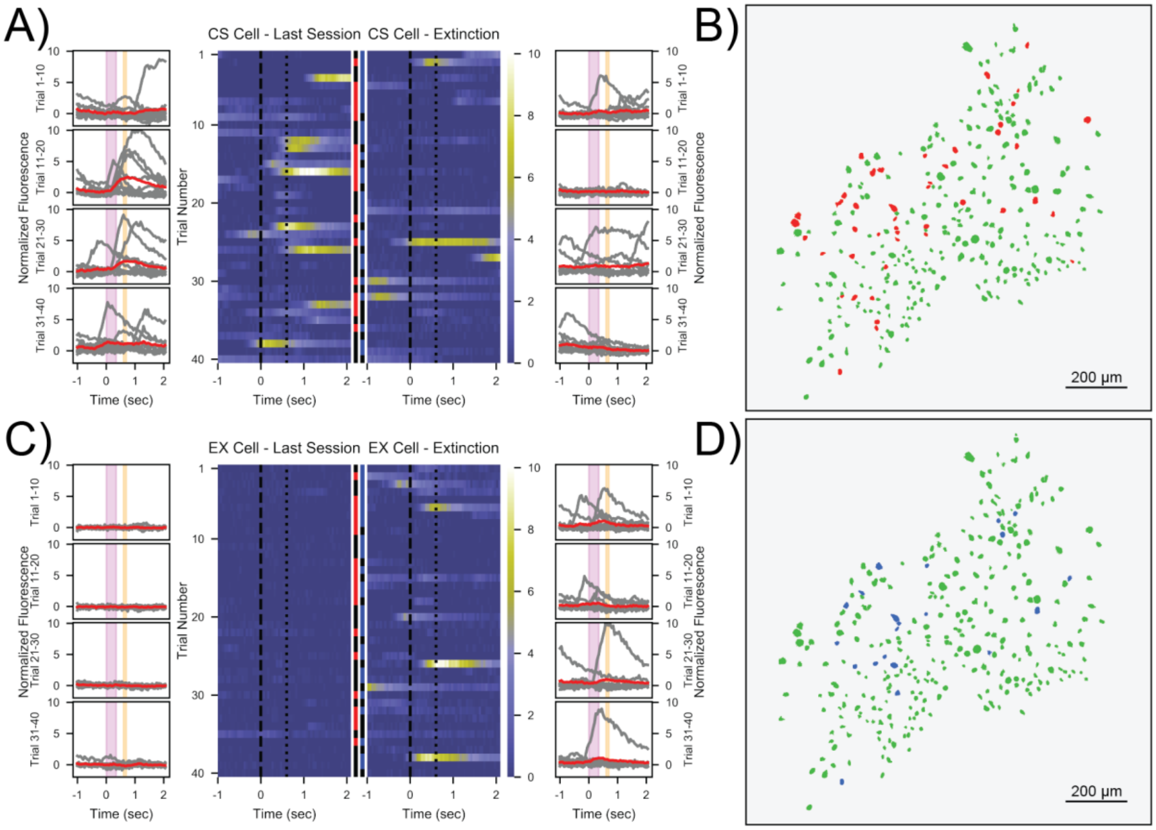

Figure 14. Tone responsive neurons in conditioning trials represent uniquely different populations of cells than tone responsive cells during extinction trials

(A) Individual single trial responses for one neuron that shows a high level of responding on the last training session, termed a CS Cell. Outer columns have individual trials shown in gray, with the 10-trial average shown in red. The pink box corresponds to the tone interval, and the orange box corresponds to the puff. Center heat-maps show each trial for the window surrounding the tone-puff time. Central color bars correspond to behavioral label for each trial, with black representing squint, red representing no squint on the last session, and blue representing no squint for extinction. **(B)** Spatial map of all neuron masks, with red neurons representing CS Cells neurons and green as all other cells. **(C)** Similar plot as in (A), but for a cell that showed high tone sensitivity only on extinction training trials. Note that both the CS and EX cells do not respond on every trial, but show reliable predictability across the full session. **(D)** Spatial map with blue neurons representing EX Cells, with green cells representing all other cells.

4.3.5 Network analysis reveals dynamic encoding connected to the correct behavioral response for both conditioned and extinction learning

As most CS and EX neurons classified from trial averaged responses consistently responded on a relatively small percentage of trials, we developed a method to quantify network responses on a trial-by-trial basis. Development of this method was additionally motivated by the observation of cells that were activated in response to the CS a small proportion for either the last session, extinction session, or both (Figure 15A), but were not coded as either a CS or EX cell from trial averaged responses. The ability of individual cells to encode CS presentations on a sparse number of trials suggests that network or population responses are critical for the encoding of learning and memory in CA1. While pairwise correlation can give reliable measures over many averaged trials, this analysis method provides a read-out of coincident population activity in a single trial. We generated a co-occurrence matrix by comparing the calcium responses over the brief time period between the tone and puff to an equal time period before the tone for every trial. For each calcium trace, it was assigned a binary response variable, with 1 being increase in activity, and 0 being no increase in activity (Figure 15Bi). Taking the outer product of this response vector yielded a co-occurrence matrix based on the response values tied to the tone-puff window for each individual trial (Figure 15Bii). Individual trial co-occurrence matrices can be combined to look at functional network responses on specific subsets of trials and clustered using spectral bi-clustering to compare neurons that were important for those trials.

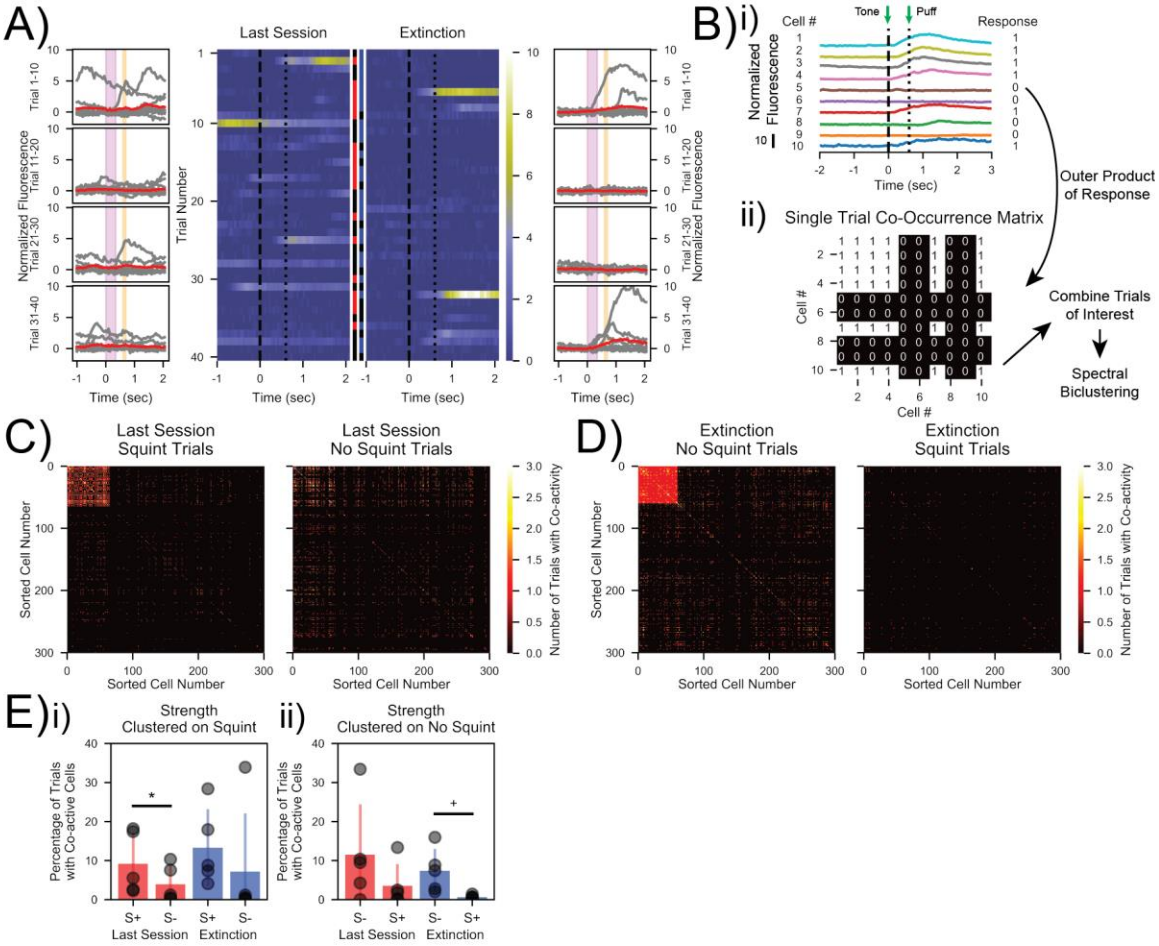

Figure 15. Co-occurrence matrix as a measure of network activity across specific trials

(A) Non-classified cell (neither CS or EX) that highlights heterogeneity that is representative of the general population of cells. Neuron is plotted similar to Figure 3A and Figure 3C. **(B)** Schematic of method for constructing single-trial networks. **(Bi**) A sub-population of cells for one trial that highlights the how the response pattern was determined. If cells showed an increase between the tone-puff compared to the pre-tone period, they were determined as a responsive cell. **(Bii)** The outer product was taken of the response vector with itself across the full population to generate a single trial co-occurrence matrix. This is a binary matrix with a 1 corresponding to the ith and jth cells both increasing between the tone-puff, but is a 0 otherwise. These individual trials can be combined as specific trials of interest, and clustered with spectral biclustering to observe network behaviors. **(C)** Co-occurrence matrices summed and clustered across all squint or no squint trials for the last training session. When first clustered for the correct behavioral response of squinting, neurons in the highly responsive cluster were co-activated on significantly more trials then they were for the incorrect behavior. This did not hold true for neurons in the highly active cluster for the incorrect behavior (not shown). **(D)** Extinction session co-occurrence matrices summed and clustered across behavioral responses. Neurons in the highly active cluster for the correct behavioral response of no squinting were co-active on a significantly higher percentage of trials than for the squint trials. As with C, this was not the case for neurons in the cluster corresponding to the incorrect behavior (not shown). **(E)** Quantification of the percentage of trials cells were co-active for in the highly co-firing cluster. **(Ei)** When clustered based on the squint trials (S+), neurons were co-active on a higher percentage of trials on the squint trials than for the no squint trials (S-) on the last trace conditioning session. This was not consistently true for the extinction session. *p<0.05, paired two-sided t-test. **(Eii)** When first clustered based on the no squint trials (S-), neurons were co-active for a higher percentage of trials with no squint than trials with a squint. This was not consistent for the last training session. +p=0.05, paired two-sided t-test.

Combining co-occurrence matrices across squint trial type showed that significantly more cells in the network were co-active in the “correct” behavior context for that session. Trials for the last trace conditioning session were group by squint and no squint trials. Clustering was performed on the squint trials, and that same clustering was maintained to look at the responses of those same neurons for the no squint trials (Figure 15C). For the cluster that was highly active between the tone and puff, cells were co-activated on 9.2 ± 8.0% (mean ± s.d.) of squint trials, which was significantly more than the 3.9 ± 4.7% (mean ± s.d.) of trials that neurons in this cluster were co-active for on no squint trials (Figure 15Ei: red bars, p<0.05, two-tailed paired t-test). To ensure that it was the identities of the cells for the “correct” context that was important to have co-active, neurons were also first clustered for the no squint context and the percentage of trials with co-active cells were then compared for these cells in the squint context, with no significant difference existing between the groups (Figure 15Eii: red bars). Additionally, when first clustered for the “correct” behavioral context of not squinting for the extinction session, the same effect was observed (Figure 15D). For the highly active cluster on no squint trials, neurons were co-activated between the CS and US on 7.4 ± 5.6% (mean ± s.d.) of trials, which was significantly more than the 0.7 ± 0.5% (mean ± s.d.) of trials when the animal squinted and the cells were co-activated (Figure 15Eii: blue bars, p=0.05, two-tailed paired t-test). Again, when first clustered for the “incorrect” behavioral response of squinting for the extinction session, this same effect was not observed consistently across all mice (Figure 15Ei: blue bars).

4.4 Discussion

In this study we provide the first detailed evidence that distinct populations of neurons within the hippocampus that consistently respond to a trace conditioned stimulus (CS Cells) represent a different population than cells that respond to the same cue during extinction (EX Cells). It was previously reported that two functionally distinct neuron populations are activated by conditioning and extinction for fear conditioning in the amygdala [151]. A subsequent study looking at the CA1 region of the hippocampus in a contextual fear paradigm, revealed distinct changes in phosphorylation states in fear conditioning and fear extinction in largely non-overlapping neural populations [152]. However, this study used pERK immuno-activity as a marker of extinction and was measured after 5 days of extinction. This delay makes it difficult to assess if changes in extinction neuron populations occur rapidly or evolve gradually, perhaps relying on new protein synthesis and long-term plasticity.

In order to better understand the relationship between conditioning and extinction learning in the hippocampus, and whether distinct populations encode these learning events, we used calcium imaging as a tool to monitor the activity of individual cells through conditioning and extinction learning paradigms. We also applied trace eye-blink conditioning which has the advantage of a singular defined stimulus where neural activity can be easily aligned, measured between the two different paradigms, and allows training under both conditions to occur in the same session. Interestingly we found that new conditioning evolved slowing in the trace task, reflected both in the response rate of individual animals and the proportion of neurons that were active during the tone or trace interval. Our results support that conditioned learning gradually evolves over many days as new neurons are recruited to encode the stimulus and reflect previous electrophysiology studies in rabbits and rats where the time course of learning is slow and evolves through many CS-US pairings [156], [157]. In contrast extinction learning was rapid and involved the emergence of a new population of neurons that responded to the now extinguished tone in less than 6 consecutive presentations. Previous work has implicated PFC and septal cholinergic input as being critical to the process of extinction, suggesting that the influence of these pathways may play a pivotal role in the rapidity with which EX neurons in emerge [158]–[160]. More work will need to be done on this front to determine if reducing or silencing these inputs could delay or block the emergence of EX neurons. In addition, it is possible that extinction learning can occur rapidly because a meaningful memory schema already exists. Studies probing updates in location encoding in familiar places suggest memory encoding can occur rapidly [161], [162] for spatial information and our observation for extinction learning may reflect a manifestation of this principle. A second important feature is that these neurons were almost entirely non-responsive to the CS prior to it being unpaired with the US. It is unlikely that these neurons are different simply because they are inhibitory neurons, as previous studies have shown that inhibitory cells have distinctive calcium waveforms in cortical and subcortical regions [72], [163] suggesting that EX neurons are most likely excitatory principal cells. This interpretation is consistent with the description of EX neurons in the amygdala and p-ERK+ cells in the hippocampus being excitatory neurons.

The use of calcium imaging is a powerful tool to understand how large populations of neurons function at the network level. However, when network changes occur rapidly, as in response to extinction learning, it can be difficult to decode the information present in the population code. Single trial analytics can suffer from the ability to find meaningful correlations with limited data. In our case, we were trying to determine correlations across hundreds of neurons with only 12 time-points between the tone and puff. As a result, we had low confidence in the pairwise correlation values measured on a trial-by-trial basis. Our development of a co-occurrence matrix developed provides an intuitive way to measure and observe the evolution of the network while factoring in the contributions of neurons that responded between the tone and puff on a smaller number of trials. Additionally, it can be used to break down and compare trials by specific behaviors (blink/no blink) or other variables that may change with trials over time. This is a useful technique for monitoring the evolution of these neuronal networks over time with high-dimensional calcium imaging datasets.

4.5 Materials and Methods

4.5.1 Animal Surgery and Recovery

All animal procedures were approved by the Boston University Institutional Animal Care and Use Committee. A total of 5 female C57BL/6 mice, 8–12 week old at the start of the experiments, were used in these studies (Taconic; Hudson, NY). Following arrival from the vendor, mice were allowed to habituate to the vivarium for 2+ weeks prior to surgery. Animals were group housed during this time. Animals first underwent viral injection surgery targeting the hippocampus under stereotaxic conditions (AP: -2.0 mm, ML:+1.5 mm, DV: -1.6 mm). Mice were injected with 250 nL of AAV9-Syn-GCaMP6f.WPRE.SV40 virus obtained from the University of Pennsylvania Vector Core (titer ~6e12 GC/ml). All injections were made via pulled glass pipettes (diameter: 1.2 mm) pulled to a sharp point and then broken at the tip to a final inner diameter of ~20 µm. Virus was delivered via slow pressure ejection (10-15 psi, 15-20 ms pulses delivered at 0.5 Hz). The pipette was lowered over 3 min and allowed to remain in place for 3 min before infusion began. The rate of the infusion was 100 nL/min. At the conclusion of the infusion, the pipette remained in place for 10 min before slowly being withdrawn over 2-3 minutes. Upon complete recovery (7+ days after virus injection, mice underwent a second procedure for the implantation of a sterilized custom imaging cannula (OD: 0.317 cm, ID: 0.236 cm, height, 2 mm diameter), fitted with a circular coverslip (size 0; OD: 3mm) adhered using a UV-curable optical adhesive (Norland Products). To access dorsal CA1, the cortical tissue overlying the hippocampus was carefully aspirated away to expose the corpus callosum. The white matter was then thinned until the underlying tissue could be visualized through the surgical microscope. The window was then placed and centered above the hippocampus. During the same surgery, a custom aluminum head-plate was attached to the skull, anterior to the imaging cannula.

4.5.2 Animal Training and Trace Conditioning Behavioral Paradigm

Mice were trained on a trace eye-blink conditioning task similar to what was described previously [20]. Animals were allowed at least 2 weeks to recover from surgeries, followed with an additional 2-4 weeks of handling and habituation to being head-fixed underneath the microscope (Figure 12Bii). Each animal received at least 3 habituation sessions prior to the first recording day. Habituation was performed in the dark with the imaging LED illuminated to the same intensity as it would be for recording sessions.

Following habituation, training for the eye-blink conditioning task began. Each trial consisted of a 350 ms long 9500 Hz tone (conditioned stimulus - CS) at 78-84 dB followed by a 250 ms trace interval, followed by a 100 ms puff to the eye (unconditioned stimulus – US) at 4.2-6 psi (Figure 12Bi). The ambient noise level ranged between 55-60 dB. Inter-trial intervals for each presentation were pseudo-randomized within a recording session with an inter-trial interval of 35 ± 5 seconds. The first 20 recording trials consisted of tone only presentation without the puff. Animals were then presented with either 60 tone-puff trials per day for 8 days, or 80 tone-puff trials per day for 4 days. The final recording session consisted of 20-40 tone-puff trials as the last learning session, followed by 40 extinction trials, where the puff was removed but the tone continued for those trials. Behavioral stimuli were generated using a custom MATLAB script that delivered TTL pulses for the tone and puff via an I/O interface (USB-6259; National Instruments, Austin, TX). Behavioral TTL pulses and imaging frame timing were digitized and recorded (Digidata 1440A; Axon CNS Molecular Devices, San Jose, CA or RZ5D Bioamp

Processor; Tucker Davis Technologies, Alachua, FL) to align behavioral data and imaging frames.

Mouse eye positioning was captured using a Flea3 USB 3.0 camera (FL3-U3-13S2C-CS; Richmond, BC, Canada) and the Point Grey FlyCapture 2 software, after illuminating the eye and surrounding area with an infrared (IR) lamp positioned approximately 0.05-0.5 meters away from the mouse.

4.5.3 Wide-field imaging

A custom-built wide-field microscope was used to record neuronal calcium responses during animal learning and behavior as previously described [20]. Briefly, the animal was head-fixed below the microscope on an articulating base (SL20 Articulating Base Ball Stage; Thorlabs Inc, Morganville, NJ) and a custom-machined attachment for the headbar, with the animal being covered by an elastic self-adherent wrap to reduce movement during recording. The microscope consisted of a scientific CMOS (sCMOS) camera (ORCA-Flash4.0 LT Digital CMOS camera C11440-42U; Hamamatsu, Boston, MA) was used in conjunction with standard optics for imaging GCaMP6 and a 10x magnification objective (Leica N Plan 10 X 0.25 PH1 or Mitutoyo Plan Apo Long WD Objective 10 X 0.28). Images yielded a field of view 1.343 mm by 1.343 mm (1024x1024 pixels) and were acquired at a 20 Hz sampling rate and stored for offline for analysis.

4.5.4 Behavior Eye-blink Segmentation and Analysis

First, each raw video was segmented using Fiji [154] and the MorphoLibJ plugin [155] to generate a binary mask video corresponding to the animal's eye. To do so, each frame of this binary video was summed and normalized by the average eye size to generate a trace corresponding to the percentage of eye closure over time. First, image stacks were loaded as grayscale images, Gaussian filtered with a radius of 2, and thresholded to include only the eye range. Videos were converted to binary, holes were filled, and the Particle Analyzer feature was used to exclude all ROIs on the edges of the videos above the thresholded value. The MorphoLibJ plugin [155], was used to label connected components with a connectivity of 26. A custom Jython script (StepIntegers.py) was used to determine the connected components that existed across all image frames, which were merged into one connected component. Lastly, to capture any additional smaller connected components that commonly were created at or around the time of blinks, another custom Jython script (FindModalValues.py) was used to capture these remaining components which were then merged into the final connected component. All other connected components not a part of this singular merged component were dropped from the binary mask stack which was saved for eye-blink trace generation.

Eye-blink traces over time were generated by summing the binary pixels corresponding to the segmented eye in each video frame and dividing by the average eye size across the whole video. An eye squint was classified by calculating a threshold of deviation from the standard eye sizing. The threshold was calculated by fitting a line to the central 95 percentile of the full eye-blink trace, and a deviation of eye size below 2% from this line was classified as a squint. This is equivalent to when the residuals deviated by 2% from a uniform distribution. This distribution was chosen based on the assumption that the eye trace that was equal to a constant equivalent to the average eye size. Each time the eye-trace showed a decrease below this threshold after the tone but before the puff, that trial was classified as a squint trial.

4.5.5 Movement Correction

Motion correction of videos was done using *ptmc*, an open-source, parallel Python version (github.com/HanLabBU/ptmc) of an image stabilization process published previously [20]. Briefly, each frame was motion corrected by median filtering each image to remove noise, homomorphic filtering the image for edge detection, and comparing the frame with a reference image to determine how many pixels to shift that specific frame. This process was run in parallel by first motion correcting the first multi-page tiff stack (2047 frames) with to an average projection image of the noisy, non-corrected video. This corrected video stack was used to generate a new reference image that was sent out in parallel with every frame across the whole video, including the first tiff stack used to generate the reference.

4.5.6 Neuronal Trace Extraction

After motion correction, regions-of-interest (ROIs) corresponding to cells were selected using a semi-automated custom written MATLAB software called *SemiSeg* (github.com/HanLabBU/SemiSeg). First, a projection image (Max-minus-Min) across the whole video stack was calculated for selecting ROIs. This static frame was loaded into SemiSeg and the full boundary of the ROIs was selected by a user selecting a sub-region of the image that was thresholded to determine the corresponding pixels within that region that correspond to a cell. After all cells were selected from the projection image, pixels corresponding to these ROIs were averaged together spatially to calculate a temporal trace for each neuron.

For sessions where ROIs were matched to one another, spatial ROI maps were co-registered using frame-wise cross-correlation. ROIs were then matched using a greedy method that required the centroid of cells to be within 50 pixels of one another and had to have at least 50% of their pixels overlap, as was published previously [90]. Cells that did not meet both of those criteria were removed from the matched dataset for comparison.

4.5.7 Fluorescence Trace Normalization

Each neuron’s fluorescence trace was normalized after a local background subtraction calculated for each trace. A local background trace was calculated by finding the centroid for each ROI, and measuring a circle approximately 10 cell widths in radius (100 pixels) and subtracting the area for the ROI from that circle. The pixels in this local background were averaged together spatially to measure a temporal background trace. Background traces were subtracted from each cell’s measured trace to remove local fluctuations from scattering in wide-field imaging. The baseline calcium level was calculated for each cell by fitting a normal distribution to the lowest 50 percentile of the data and using the mean of this distribution as the baseline calcium level. This baseline was subtracted from each locally corrected trace, and data was scaled by 5% of the maximum range of the full calcium trace.

4.5.8 Determination of Increased Activity Cells

Fluorescence for the 12 data-points (600 ms) within the tone-puff interval was compared to the 12 data-points prior to the tone. A cell was classified as having increased if the average fluorescence during the tone-puff window was larger than the average fluorescence for the pre-tone window by 0.15, a value that is equivalent to crossing a threshold of 1 on at least 6 trials. This was the threshold used for all statistics and for comparison with the network measure.

4.5.9 Bootstrapping Procedure

Trial averaged bootstraps were calculated for each mouse to determine what percentages of cells would be expected to increase in random recordings not tied to the tone-puff learning paradigm. Timing between each pseudo-randomized tone-puff was maintained to account for any periodicity effects during the recording, and bootstraps were calculated by circularly permuting the tone-puff timing across all traces. The number of shuffled permutations performed was 1000 for each mouse. The timing of each new randomized tone puff was averaged together across all shuffled trials, and the percentage of cells that increased between the tone and puff was measured. The percentage of cells increased for each mouse was averaged together to get a population estimation of the mean number of cells expected to increase within the population, which could be compared to the measured percentage of the population that increased between the actual tone-puff across all trials.

4.5.10 Co-occurrence Network Creation

Individual trial co-occurrence matrices were created for each pair of cells across every trial. For each tone-puff interval, the mean value of the 600 milliseconds (12 data-points) between the tone and puff was compared to the 600 milliseconds before the tone. If this value was greater than 1 on a normalized trace, corresponding to 5% the maximum peak value of a trace, then the neuron was labelled as responding. The result was a binary vector of 0s and 1s of length N, where N is the number of cells recorded in the population. The outer product of this vector was taken with itself for the whole population to yield an NxN co-occurrence matrix. This matrix is 1 if both the ith and jth cells were activated between the tone-puff, and 0 otherwise.

Once a co-occurrence network was generated for each trial, they could be combined for further analyses by either summing (Figure 15C & Figure 15D) or averaging (Figure 4E quantification) over all trials or certain trials (Figure 15C & Figure 15D) of interest. Once a trial combination map was created, spectral biclustering was performed for a 2x2 cluster pattern using the Python machine learning package scikit-learn [164]. A cluster size of 2 was chosen because it resulted in the maximal silhouette score (also implemented in scikit-learn) for the clustering across mice.

4.6 Supplemental Information

4.6.1 Supplemental Figures

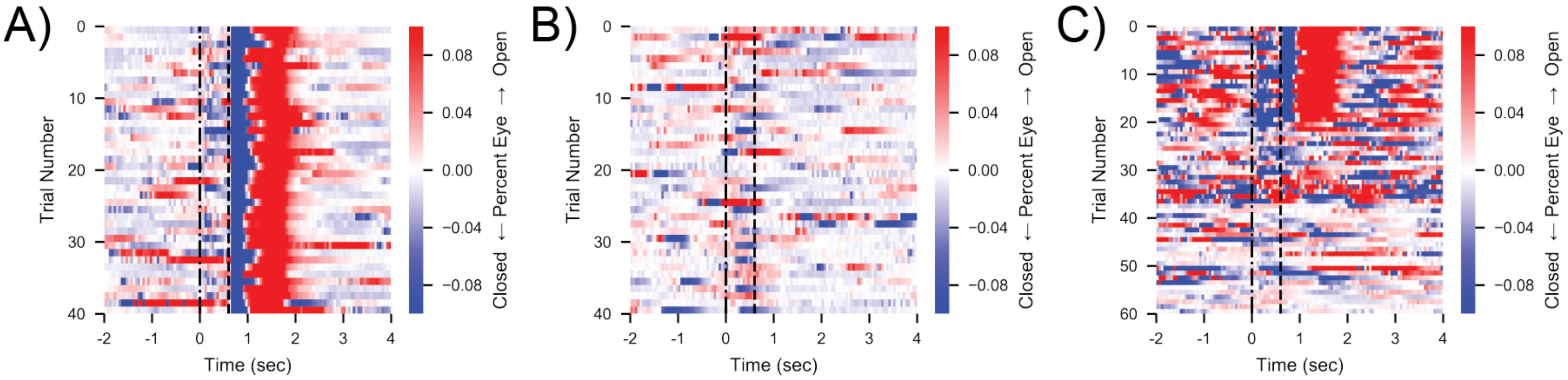

Figure 16. Behavioral responses across different stages of learning

Extracted eye traces and movement intensity. Red corresponds to eye opening, while blue corresponds to eye closure. **(A)** Eye trace for all 40 trials of the first training session from the same example mouse in Figure 12 Cii. Note the fewer blue values corresponding to eye closure between the tone and puff. **(B)** Eye trace for all 40 trials of the extinction session of the same example mouse in A. Note that the hard eye closure at the time of the puff is no longer there, as the puff has been removed for extinction. **(C)** Last training session on extinction day for another example mouse. The first 20 trials have the CS-US presentation separated by the trace period, and the final 40 trials are the extinction trials. Note how clearly the behavioral difference can be observed after trial 20, both in the tone-puff interval as well as after the puff once the puff is removed for extinction.

CHAPTER 5 - CONCLUSION

5.1 Summary and Significance

The work in this dissertation established methods for the analysis of large scale calcium imaging data, and used these methods to develop novel insights about mTBI and learning. While the primary design criterion was analyzing large scale calcium imaging datasets, many of the computational tools and techniques are applicable for other large scale video data, time series, or discrete trial-based data. Additionally, all these methods have been provided in an open-source manner to enable neuroscientists to move the field forward at a more rapid pace. As neuroscience moves into the big data age, scientists need to work together in developing more unified methods that can allow rapid feedback, more accurate comparisons between datasets, and enable the design of future experiments.

The pre-processing tools and techniques developed can address the challenges that arise using large scale calcium imaging datasets. A published motion correction algorithm was parallelized for a 10% decrease in processing time. Additionally, the framework established with this method is both modular and user friendly, which allows individual researchers to more easily apply this pipeline to their own data. The semi-automated segmentation toolbox described herein allows researchers to segment ROIs from large datasets with high confidence. Again, user flexibility is provided to determine how much information to integrate for the segmentation, with trade-offs in the time it takes a user to segment a dataset. Importantly, these methods provide high-quality data and complete code transparency provides researchers with a high level of confidence in the quality of the first level of their processing pipeline.

Applying these tools to a study of calcium dynamics for mTBI yielded new insights about how both basal and transient calcium dynamics in the hippocampus were impacted from blast injury. A new normalization technique to enable comparison across multiple recording sessions highlighted a basal calcium change that slowly recovered over minutes. If using calcium deconvolution methods [79], [81], [85], [165] to estimate neuronal spiking traces, this important biological effect from blast injury would have been completely missed, as well as its lack of connection to the transient calcium dynamics more commonly related to neuronal spiking events. Additionally, we reported that these calcium dynamics were impacted differently by subsequent blasts. These insights are important avenues to further study the mechanisms of neuronal damage from blast injuries. Finally, this study established calcium imaging as an important and useful tool for understanding both acute and longitudinal effects of blast injuries which can build upon the literature of histological analysis for brain injury.

Additional insights were gained using these tools to study the short-term temporal connection between trace conditioning and extinction learning. Large scale calcium imaging methods enabled the tracking of the same neuronal population in CA1 to determine the neurons that respond to the CS after many days of training are mostly distinct from neurons that respond to the CS during extinction. This dynamically and rapidly captured functional dynamics that were reported in previous fear conditioning and extinction studies in the amygdala [151] and in gene expression in the hippocampus [152]. A method to investigate neuronal responses on a trial-by-trial basis was also developed for analyses with few data points in time and used to show that neurons that consistently respond for the “correct” behavior in both learning contexts respond for significantly more trials in those contexts than the neurons that responded to the incorrect behavior. These contributions provide a method to further probe specific subsets of trials in multi-trial behavioral paradigms while also confirming previous scientific findings using functional neuronal responses.

Altogether, the efforts described in this dissertation help make large scale calcium imaging more easily adoptable by other researchers as well as highlight future insights that can be gained and developed with these methods.

5.2 Future Directions

The tools and findings established in this body of work highlight several potential new directions that can be explored and improved upon. For the preprocessing motion correction pipeline, the established framework could be easily further parallelized for a cluster environment to further improve runtime by a factor of 13 to 20. This can be accomplished as the major remaining bottleneck in processing comes from loading the multi-page tiffs into memory and saving them after processing. Sending each multi-page tiff with a copy of the reference image to a different machine in a cluster environment would help accomplish this improvement. The Matlab image segmentation toolbox could also be converted to a Python version to be more amenable for the open-source community and be less likely to run into backwards compatibility issues in subsequent versions. Calcium imaging should be employed more regularly to study both the acute and longitudinal effects of blast injury for both single and multiple blast paradigms, as this can provide a wealth of unique insights for blast related injuries that are not possible with conventional histological methods. Additional studies should also be conducted to determine how neuronal responses for extinction learning over multiple days as well as reinstatement relate to the populations that emerge for trace conditioning and the first extinction session to better understand how the hippocampus processes different aspects of learning and memory.

Future studies built upon this work will enable large scale calcium imaging to further develop and enable researchers to bridge our understanding of networks at both the micro- and macro-scales. Developing this knowledge and improving our understanding across scales will provide important insights into the function of healthy brains and allow for better and more intelligent design of treatments of neurological disease.

BIBLIOGRAPHY

[1] GBD 2015 Neurological Disorders Collaborator Group, “Global, regional, and national burden of neurological disorders during 1990-2015: a systematic analysis for the Global Burden of Disease Study 2015.,” *The Lancet. Neurology*, vol. 16, no. 11, pp. 877–897, 2017.

[2] C. L. Gooch, E. Pracht, and A. R. Borenstein, “The burden of neurological disease in the United States: A summary report and call to action.,” *Annals of Neurology*, vol. 81, no. 4, pp. 479–484, Apr. 2017.

[3] T. Pringsheim, K. Fiest, and N. Jette, “The international incidence and prevalence of neurologic conditions: how common are they?,” *Neurology*, vol. 83, no. 18, pp. 1661–4, Oct. 2014.

[4] E. R. Kandel, J. H. Schwartz, and T. M. Jessell, *Principles of Neural Science*, 4th ed. New York: McGraw-Hill, Health Professions Division, 2000.

[5] C. Sotelo, “Viewing the brain through the master hand of Ramón y Cajal.,” *Nature Reviews. Neuroscience*, vol. 4, no. 1, pp. 71–77, 2003.

[6] S. W. Oh *et al.*, “A mesoscale connectome of the mouse brain.,” *Nature*, vol. 508, no. 7495, pp. 207–14, Apr. 2014.

[7] M. N. Economo *et al.*, “A platform for brain-wide imaging and reconstruction of individual neurons.,” *eLife*, vol. 5, p. e10566, Jan. 2016.

[8] R. Perin and H. Markram, “A Computer-assisted Multi-electrode Patch-clamp System,” *Journal of Visualized Experiments: JoVE*, no. 80, pp. 1–13, 2013.

[9] K. G. Klemic, J. F. Klemic, M. A. Reed, and F. J. Sigworth, “Micromolded PDMS planar electrode allows patch clamp electrical recordings from cells,” *Biosensors and Bioelectronics*, vol. 17, no. 6–7, pp. 597–604, 2002.

[10] A. C. Snyder, M. J. Morais, C. M. Willis, and M. A. Smith, “Global network influences on local functional connectivity,” *Nature Neuroscience*, vol. 18, no. 5, pp. 736–743, 2015.

[11] J. Viventi *et al.*, “Flexible, foldable, actively multiplexed, high-density electrode array for mapping brain activity in vivo.,” *Nature Neuroscience*, vol. 14, no. 12, pp. 1599–605, 2011.

[12] J. C. Chang, G. J. Brewer, and B. C. Wheeler, “Modulation of neural network activity by patterning.,” *Biosensors & Bioelectronics*, vol. 16, no. 7–8, pp. 527–33, 2001.

[13] H. Lison *et al.*, “Disrupted cross-laminar cortical processing in β amyloid pathology precedes cell death,” *Neurobiology of Disease*, vol. 63, pp. 62–73, 2014.

[14] D. Sullivan, K. Mizuseki, A. Sorgi, and G. Buzsaki, “Comparison of sleep spindles and theta oscillations in the hippocampus,” *The Journal of Neuroscience*, vol. 34, no. 2, pp. 662–674, 2014.

[15] S. Haegens *et al.*, “Laminar Profile and Physiology of the α Rhythm in Primary Visual, Auditory, and Somatosensory Regions of Neocortex.,” *The Journal of Neuroscience*, vol. 35, no. 42, pp. 14341–52, 2015.

[16] Y. Gong *et al.*, “High-speed recording of neural spikes in awake mice and flies with a fluorescent voltage sensor,” *Science*, vol. 350, no. 6266, pp. 1361–1366, 2015.

[17] D. R. Hochbaum *et al.*, “All-optical electrophysiology in mammalian neurons using engineered microbial rhodopsins.,” *Nature Methods*, vol. 11, no. 8, pp. 825–33, 2014.

[18] A. S. Marcos and C. D. Harvey, “History-dependent variability in population dynamics during evidence accumulation in cortex,” *Nature Neuroscience*, vol. 19, no. 12, pp. 1672–1680, 2016.

[19] M. N. Economo, K. R. Hansen, and M. Wachowiak, “Control of Mitral/Tufted Cell Output by Selective Inhibition among Olfactory Bulb Glomeruli,” *Neuron*, vol. 91, no. 2, pp. 397–411, 2016.

[20] A. I. Mohammed, H. J. Gritton, H.-A. Tseng, M. E. Bucklin, Z. Yao, and X. Han, “An integrative approach for analyzing hundreds of neurons in task performing mice using wide-field calcium imaging.,” *Scientific Reports*, vol. 6, no. Feb 8, p. 20986, 2016.

[21] P. Broca, “Remarques sur le siège de la faculté du langage articulé, suivies d’une observation d’aphémie (perte de la parole).,” *Bulletin de la Société Anatomique*, vol. 6.343, p. 57, 1861.

[22] C. Wernicke, “The Aphasic Symptom-Complex:A Psychological Study on an Anatomical Basis,” *Archives of Neurology*, vol. 22, no. 3, pp. 280–282, 1970.

[23] F. Seitelberger, “Theodor Meynert (1833-1892), pioneer and visionary of brain research.,” *Journal of the History of the Neurosciences*, vol. 6, no. 3, pp. 264–74, 1997.

[24] M. Loukas, C. Pennell, C. Groat, R. S. Tubbs, and A. A. Cohen-Gadol, “Korbinian Brodmann (1868-1918) and his contributions to mapping the cerebral cortex,” *Neurosurgery*, vol. 68, no. 1, pp. 6–11, 2011.

[25] E. Bullmore and O. Sporns, “Complex brain networks: graph theoretical analysis of structural and functional systems,” *Nature Reviews. Neuroscience*, vol. 10, no. 3, pp. 186–198, 2009.

[26] C. J. Stam, “Modern network science of neurological disorders,” *Nature Reviews Neuroscience*, vol. 15, no. 10, pp. 683–695, 2014.

[27] R. C. Mesquita, M. A. Franceschini, and D. A. Boas, “Resting state functional connectivity of the whole head with near-infrared spectroscopy.,” *Biomedical Optics Express*, vol. 1, no. 1, pp. 324–336, 2010.

[28] T. Fekete, F. D. C. C. Beacher, J. Cha, D. Rubin, and L. R. Mujica-Parodi, “Small-world network properties in prefrontal cortex correlate with predictors of psychopathology risk in young children: A NIRS study,” *NeuroImage*, vol. 85, pp. 345–353, 2014.

[29] S. Sasai, F. Homae, H. Watanabe, and G. Taga, “Frequency-specific functional connectivity in the brain during resting state revealed by NIRS,” *NeuroImage*, vol. 56, no. 1, pp. 252–257, 2011.

[30] M. P. van den Heuvel and H. E. Hulshoff Pol, “Exploring the brain network: A review on resting-state fMRI functional connectivity,” *European Neuropsychopharmacology*, vol. 20, no. 8, pp. 519–534, 2010.

[31] J. Richiardi *et al.*, “Correlated gene expression supports synchronous activity in brain networks,” *Science*, vol. 348, no. 6240, pp. 1241–1244, Jun. 2015.

[32] G. Barbera *et al.*, “Spatially Compact Neural Clusters in the Dorsal Striatum Encode Locomotion Relevant Information,” *Neuron*, vol. 92, no. 1, pp. 202–213, 2016.

[33] W. B. Scoville, “The Limbic Lobe in Man,” *Journal of Neurosurgery*, vol. 11, no. 1, pp. 64–66, 1954.

[34] W. B. Scoville and B. Milner, “Loss of recent memory after bilateral hippocampal lesions.,” *Journal of Neurology, Neurosurgery, and Psychiatry*, vol. 20, no. 1, pp. 11–21, Feb. 1957.

[35] G. Fein *et al.*, “Hippocampal and cortical atrophy predict dementia in subcortical ischemic vascular disease.,” *Neurology*, vol. 55, no. 11, pp. 1626–35, Dec. 2000.

[36] L. G. Apostolova *et al.*, "Subregional hippocampal atrophy predicts Alzheimer's dementia in the cognitively normal.," *Neurobiology of Aging*, vol. 31, no. 7, pp. 1077–88, Jul. 2010.

[37] N. Chow *et al.*, "Comparing Hippocampal Atrophy in Alzheimer's Dementia and Dementia with Lewy Bodies," *Dementia and Geriatric Cognitive Disorders*, vol. 34, no. 1, pp. 44–50, 2012.

[38] W. J. P. Henneman *et al.*, "Hippocampal atrophy rates in Alzheimer disease: Added value over whole brain volume measures," *Neurology*, vol. 72, no. 11, pp. 999–1007, 2009.

[39] R. Camicioli, M. M. Moore, A. Kinney, E. Corbridge, K. Glassberg, and J. A. Kaye, "Parkinson's disease is associated with hippocampal atrophy," *Movement Disorders*, vol. 18, no. 7, pp. 784–790, 2003.

[40] K. R. Walker and G. Tesco, "Molecular mechanisms of cognitive dysfunction following traumatic brain injury.," *Frontiers in Aging Neuroscience*, vol. 5, p. 29, 2013.

[41] A. I. R. Maas, "Traumatic brain injury: simple data collection will improve the outcome.," *Wiener Klinische Wochenschrift*, vol. 119, no. 1–2, pp. 20–2, Feb. 2007.

[42] S. K. Kovacs, F. Leonessa, and G. S. F. Ling, "Blast TBI Models, Neuropathology, and Implications for Seizure Risk.," *Frontiers in Neurology*, vol. 5, p. 47, 2014.

[43] V. S. S. S. Sajja, W. B. Hubbard, C. S. Hall, F. Ghoddoussi, M. P. Galloway, and P. J. VandeVord, "Enduring deficits in memory and neuronal pathology after blast-induced traumatic brain injury.," *Scientific Reports*, vol. 5, p. 15075, Nov. 2015.

[44] D. M. Geddes, M. C. LaPlaca, and R. S. Cargill, "Susceptibility of hippocampal neurons to mechanically induced injury.," *Experimental Neurology*, vol. 184, no. 1, pp. 420–7, Nov. 2003.

[45] C. M. Atkins, "Decoding hippocampal signaling deficits after traumatic brain injury.," *Translational Stroke Research*, vol. 2, no. 4, pp. 546–55, Dec. 2011.

[46] F. Girgis, J. Pace, J. Sweet, and J. P. Miller, "Hippocampal Neurophysiologic Changes after Mild Traumatic Brain Injury and Potential Neuromodulation Treatment Approaches.," *Frontiers in Systems Neuroscience*, vol. 10, p. 8, 2016.

[47] C. P. Almeida-Suhett *et al.*, "GABAergic interneuronal loss and reduced inhibitory synaptic transmission in the hippocampal CA1 region after mild traumatic brain injury.," *Experimental Neurology*, vol. 273, pp. 11–23, Nov. 2015.

[48] E. Schwarzbach, D. P. Bonislawski, G. Xiong, and A. S. Cohen, “Mechanisms underlying the inability to induce area CA1 LTP in the mouse after traumatic brain injury.,” *Hippocampus*, vol. 16, no. 6, pp. 541–50, 2006.

[49] M. D. McEchron, H. Bouwmeester, W. Tseng, C. Weiss, and J. F. Disterhoft, “Hippocampectomy disrupts auditory trace fear conditioning and contextual fear conditioning in the rat,” *Hippocampus*, vol. 8, no. 6, pp. 638–646, 1998.

[50] J. R. Moyer, R. A. Deyo, and J. F. Disterhoft, “Hippocampectomy disrupts trace eye-blink conditioning in rabbits,” *Behavioral Neuroscience*, vol. 129, no. 4, pp. 523–532, 2015.

[51] W. Tseng, R. Guan, J. F. Disterhoft, and C. Weiss, “Trace eyeblink conditioning is hippocampally dependent in mice,” *Hippocampus*, vol. 14, no. 1, pp. 58–65, 2004.

[52] A. Gruart and J. M. Delgado-García, “Activity-dependent changes of the hippocampal CA3-CA1 synapse during the acquisition of associative learning in conscious mice,” *Genes, Brain and Behavior*, vol. 6, no. Jun, pp. 24–31, 2007.

[53] J. McLaughlin, H. Skaggs, J. Churchwell, and D. A. Powell, “Medial prefrontal cortex and Pavlovian conditioning: Trace versus delay conditioning,” *Behavioral Neuroscience*, vol. 116, no. 1, pp. 37–47, 2002.

[54] Y. Kishimoto, M. Suzuki, S. Kawahara, and Y. Kirino, “Age-dependent impairment of delay and trace eyeblink conditioning in mice,” *NeuroReport*, vol. 12, no. 15, pp. 3349–3352, 2001.

[55] M. A. Kronforst-Collins and J. F. Disterhoft, “Lesions of the caudal area of rabbit medial prefrontal cortex impair trace eyeblink conditioning,” *Neurobiology of Learning and Memory*, vol. 69, no. 2, pp. 147–162, 1998.

[56] K. Takehara-nishiuchi and B. L. McNaughton, “Spontaneous changes of neocortical code for associative memory during consolidation.,” *Science*, vol. 322, no. 5903, pp. 960–963, 2008.

[57] G. M. Dillon, X. Qu, J. N. Marcus, and J. C. Dodart, “Excitotoxic lesions restricted to the dorsal CA1 field of the hippocampus impair spatial memory and extinction learning in C57BL/6 mice,” *Neurobiology of Learning and Memory*, vol. 90, no. 2, pp. 426–433, 2008.

[58] L. A. Jorgenson *et al.*, “The BRAIN Initiative: developing technology to catalyse neuroscience discovery.,” *Philosophical Transactions of the Royal Society of London. Series B, Biological Sciences*, vol. 370, no. 1668, May 2015.

[59] K. D. Piatkevich *et al.*, “A robotic multidimensional directed evolution approach applied to fluorescent voltage reporters.,” *Nature Chemical Biology*, vol. 14, no. 4, pp. 352–360, Apr. 2018.

[60] N. Vladimirov *et al.*, “Light-sheet functional imaging in fictively behaving zebrafish,” *Nature Methods*, vol. 11, no. 9, pp. 883–884, 2014.

[61] R. M. Power and J. Huisken, “A guide to light-sheet fluorescence microscopy for multiscale imaging.,” *Nature Methods*, vol. 14, no. 4, pp. 360–373, Mar. 2017.

[62] J. Freeman, “Open source tools for large-scale neuroscience.,” *Current Opinion in Neurobiology*, vol. 32, pp. 156–63, Jun. 2015.

[63] J. M. Perkel, “A toolkit for data transparency takes shape,” *Nature*, vol. 560, no. 7719, pp. 513–515, Aug. 2018.

[64] J. Freeman *et al.*, “Mapping brain activity at scale with cluster computing,” *Nature Methods*, vol. 11, no. 9, pp. 941–950, 2014.

[65] P. Berens *et al.*, “Community-based benchmarking improves spike rate inference from two-photon calcium imaging data.,” *PLOS Computational Biology*, vol. 14, no. 5, p. e1006157, 2018.

[66] J. Freeman, “CodeNeuro: Neurofinder,” 2017. [Online]. Available: https://github.com/codeneuro/neurofinder.

[67] M. Dipoppa, A. Ranson, M. Krumin, M. Pachitariu, M. Carandini, and K. D. Harris, “Vision and Locomotion Shape the Interactions between Neuron Types in Mouse Visual Cortex.,” *Neuron*, vol. 98, no. 3, p. 602–615.e8, May 2018.

[68] M. Kawaguchi, H. Furuya, and P. M. Patel, “Neuroprotective effects of anesthetic agents.,” *Journal of Anesthesia*, vol. 19, no. 2, pp. 150–6, 2005.

[69] R. K. Rowe, J. L. Harrison, T. C. Thomas, J. R. Pauly, P. D. Adelson, and J. Lifshitz, “Using anesthetics and analgesics in experimental traumatic brain injury.,” *Lab Animal*, vol. 42, no. 8, pp. 286–91, Aug. 2013.

[70] K. D. Statler *et al.*, “Comparison of seven anesthetic agents on outcome after experimental traumatic brain injury in adult, male rats.,” *Journal of Neurotrauma*, vol. 23, no. 1, pp. 97–108, Jan. 2006.

[71] T.-W. Chen *et al.*, “Ultrasensitive fluorescent proteins for imaging neuronal activity.,” *Nature*, vol. 499, no. 7458, pp. 295–300, 2013.

[72] L. Pinto and Y. Dan, “Cell-Type-Specific Activity in Prefrontal Cortex during Goal-Directed Behavior,” *Neuron*, vol. 87, no. 2, pp. 437–451, 2015.

[73] J. Poort *et al.*, “Learning Enhances Sensory and Multiple Non-sensory Representations in Primary Visual Cortex.,” *Neuron*, vol. 86, no. 6, pp. 1478–90, Jun. 2015.

[74] M. Wachowiak *et al.*, “Optical dissection of odor information processing in vivo using GCaMPs expressed in specified cell types of the olfactory bulb,” *Annals of Internal Medicine*, vol. 158, no. 6, pp. 5285–8300, 2013.

[75] M. N. Economo, K. R. Hansen, M. N. Economo, K. R. Hansen, and M. Wachowiak, “Control of Mitral / Tufted Cell Output by Selective Inhibition among Olfactory Bulb Glomeruli Article Control of Mitral / Tufted Cell Output by Selective Inhibition among Olfactory Bulb Glomeruli,” *Neuron*, vol. 91, no. 2, pp. 397–411, 2016.

[76] K. K. Ghosh *et al.*, “Miniaturized integration of a fluorescence microscope.,” *Nature Methods*, vol. 8, no. 10, pp. 871–8, Sep. 2011.

[77] B. A. Flusberg *et al.*, “High-speed, miniaturized fluorescence microscopy in freely moving mice.,” *Nature Methods*, vol. 5, no. 11, pp. 935–8, Nov. 2008.

[78] Y. Ziv *et al.*, “Long-term dynamics of CA1 hippocampal place codes.,” *Nature Neuroscience*, vol. 16, no. 3, pp. 264–6, Mar. 2013.

[79] E. A. Pnevmatikakis *et al.*, “Simultaneous Denoising , Deconvolution , and Demixing of Calcium Imaging Data,” *Neuron*, vol. 89, no. 2, pp. 285–299, 2016.

[80] E. A. Mukamel, A. Nimmerjahn, and M. J. Schnitzer, “Automated Analysis of Cellular Signals from Large-Scale Calcium Imaging Data,” *Neuron*, vol. 63, no. 6, pp. 747–760, 2009.

[81] P. Zhou *et al.*, “Efficient and accurate extraction of in vivo calcium signals from microendoscopic video data.,” *eLife*, vol. 7, Feb. 2018.

[82] W. Mau, D. W. Sullivan, N. R. Kinsky, M. E. Hasselmo, M. W. Howard, and H. Eichenbaum, “The Same Hippocampal CA1 Population Simultaneously Codes Temporal Information over Multiple Timescales.,” *Current Biology*, vol. 28, no. 10, p. 1499–1508.e4, May 2018.

[83] J. P. Cunningham and B. M. Yu, “Dimensionality reduction for large-scale neural recordings,” *Nature Neuroscience*, vol. 17, no. 11, pp. 1500–1509, 2014.

[84] R. C. Williamson *et al.*, “Scaling Properties of Dimensionality Reduction for Neural Populations and Network Models.,” *PLoS Computational Biology*, vol. 12, no. 12, p. e1005141, 2016.

[85] J. T. Vogelstein *et al.*, “Fast Nonnegative Deconvolution for Spike Train Inference From Population Calcium Imaging,” *Journal of Neurophysiology*, vol. 104, no. June 2010, pp. 3691–3704, 2012.

[86] J. Akerboom *et al.*, “Optimization of a GCaMP Calcium Indicator for Neural Activity Imaging,” *The Journal of Neuroscience*, vol. 32, no. 40, pp. 13819–13840, 2012.

[87] C. Lüscher and R. C. Malenka, “NMDA receptor-dependent long-term potentiation and long-term depression (LTP/LTD),” *Cold Spring Harbor Perspectives in Biology*, vol. 4, no. 6, pp. 1–15, 2012.

[88] L. P. E. Austdal, G. H. Mathisen, E. M. Løberg, and R. E. Paulsen, “Calcium-induced apoptosis of developing cerebellar granule neurons depends causally on NGFI-B,” *International Journal of Developmental Neuroscience*, vol. 55, pp. 82–90, 2016.

[89] R. Bonavia, A. Bajetto, S. Barbero, A. Albini, D. M. Noonan, and G. Schettini, “HIV-1 Tat causes apoptotic death and calcium homeostasis alterations in rat neurons.,” *Biochemical and Biophysical Research Communications*, vol. 288, no. 2, pp. 301–308, 2001.

[90] S. P. Shen *et al.*, “Automatic Cell Segmentation by Adaptive Thresholding (ACSAT) for Large-Scale Calcium Imaging Datasets.,” *eNeuro*, vol. 5, no. 5, p. ENEURO.0056-18.2018, 2018.

[91] M. C. Morganti-Kossmann, E. Yan, and N. Bye, “Animal models of traumatic brain injury: is there an optimal model to reproduce human brain injury in the laboratory?,” *Injury*, vol. 41 Suppl 1, pp. S10-3, Jul. 2010.

[92] P. Burgess, E. E Sullivent, S. M Sasser, M. M Wald, E. Ossmann, and V. Kapil, “Managing traumatic brain injury secondary to explosions.,” *Journal of Emergencies, Trauma, and Shock*, vol. 3, no. 2, pp. 164–72, Apr. 2010.

[93] J. V Rosenfeld, A. C. McFarlane, P. Bragge, R. A. Armonda, J. B. Grimes, and G. S. Ling, “Blast-related traumatic brain injury.,” *The Lancet. Neurology*, vol. 12, no. 9, pp. 882–893, Sep. 2013.

[94] J. H. Stuhmiller, “Biological response to blast overpressure: a summary of modeling.,” *Toxicology*, vol. 121, no. 1, pp. 91–103, Jul. 1997.

[95] M. A. Mayorga, “The pathology of primary blast overpressure injury.,” *Toxicology*, vol. 121, no. 1, pp. 17–28, Jul. 1997.

[96] B. G. Lyeth *et al.*, “Prolonged memory impairment in the absence of hippocampal cell death following traumatic brain injury in the rat.,” *Brain Research*, vol. 526, no. 2, pp. 249–58, Sep. 1990.

[97] J. L. Gerberding and S. Binder, “Report to Congress on Mild Traumatic Brain Injury in the United States: Steps to Prevent a Serious Public Health Problem,” Atlanta, GA: Centers for Disease Control and Prevention; 2003. Available at: https://www.cdc.gov/traumaticbraininjury/pdf/mtbireport-a.pdf

[98] L. E. Goldstein *et al.*, “Chronic traumatic encephalopathy in blast-exposed military veterans and a blast neurotrauma mouse model.,” *Science Translational Medicine*, vol. 4, no. 134, p. 134ra60, May 2012.

[99] R. C. W. Hall, R. C. W. Hall, and M. J. Chapman, “Definition, diagnosis, and forensic implications of postconcussional syndrome.,” *Psychosomatics*, vol. 46, no. 3, pp. 195–202, 2005.

[100] S. I. Svetlov, S. F. Larner, D. R. Kirk, J. Atkinson, R. L. Hayes, and K. K. W. Wang, “Biomarkers of blast-induced neurotrauma: profiling molecular and cellular mechanisms of blast brain injury.,” *Journal of Neurotrauma*, vol. 26, no. 6, pp. 913–21, Jun. 2009.

[101] R. Kuehn *et al.*, “Rodent Model of Direct Cranial Blast Injury,” *Journal of Neurotrauma*, vol. 28, no. 10, pp. 2155–2169, 2011.

[102] T. Deneux *et al.*, “Accurate spike estimation from noisy calcium signals for ultrafast three-dimensional imaging of large neuronal populations in vivo,” *Nature Communications*, vol. 7, p. 12190, 2016.

[103] A. Badura, X. R. Sun, A. Giovannucci, L. A. Lynch, and S. S.-H. Wang, “Fast calcium sensor proteins for monitoring neural activity.,” *Neurophotonics*, vol. 1, no. 2, p. 025008, 2014.

[104] S. Berlin *et al.*, “Photoactivatable genetically encoded calcium indicators for targeted neuronal imaging.,” *Nature Methods*, vol. 12, no. 9, pp. 852–858, 2015.

[105] D. A. Dombeck, C. D. Harvey, L. Tian, L. L. Looger, and D. W. Tank, “Functional imaging of hippocampal place cells at cellular resolution during virtual navigation.,” *Nature Neuroscience*, vol. 13, no. 11, pp. 1433–40, Nov. 2010.

[106] J. D. Zaremba *et al.*, “Impaired hippocampal place cell dynamics in a mouse model of the 22q11.2 deletion.,” *Nature Neuroscience*, vol. 20, no. 11, pp. 1612–1623, Nov. 2017.

[107] V. Mishra, M. Skotak, H. Schuetz, A. Heller, J. Haorah, and N. Chandra, “Primary blast causes mild, moderate, severe and lethal TBI with increasing blast overpressures: Experimental rat injury model.,” *Scientific Reports*, vol. 6, p. 26992, 2016.

[108] B. F. Grewe, D. Langer, H. Kasper, B. M. Kampa, and F. Helmchen, “High-speed in vivo calcium imaging reveals neuronal network activity with near-millisecond precision.,” *Nature Methods*, vol. 7, no. 5, pp. 399–405, 2010.

[109] K. Svoboda, W. Denk, D. Kleinfeld, and D. W. Tank, “In vivo dendritic calcium dynamics in neocortical pyramidal neurons.,” *Nature*, vol. 385, no. 6612. pp. 161–5, 1997.

[110] D. F. Meaney and D. H. Smith, “Biomechanics of concussion.,” *Clinics in Sports Medicine*, vol. 30, no. 1, p. 19–31, vii, Jan. 2011.

[111] K. D. Browne, X.-H. Chen, D. F. Meaney, and D. H. Smith, “Mild traumatic brain injury and diffuse axonal injury in swine.,” *Journal of Neurotrauma*, vol. 28, no. 9, pp. 1747–55, Sep. 2011.

[112] J. Hines-Beard, J. Marchetta, S. Gordon, E. Chaum, E. E. Geisert, and T. S. Rex, “A mouse model of ocular blast injury that induces closed globe anterior and posterior pole damage.,” *Experimental Eye Research*, vol. 99, pp. 63–70, Jun. 2012.

[113] S. A. Heldt *et al.*, “A novel closed-head model of mild traumatic brain injury caused by primary overpressure blast to the cranium produces sustained emotional deficits in mice.,” *Frontiers in Neurology*, vol. 5, p. 2, 2014.

[114] V. E. Koliatsos *et al.*, “A mouse model of blast injury to brain: initial pathological, neuropathological, and behavioral characterization.,” *Journal of Neuropathology and Experimental Neurology*, vol. 70, no. 5, pp. 399–416, May 2011.

[115] Y. Xiong, A. Mahmood, and M. Chopp, “Animal models of traumatic brain injury.,” *Nature Reviews. Neuroscience*, vol. 14, no. 2, pp. 128–42, Feb. 2013.

[116] N. H. Guley *et al.*, “A Novel Closed-Head Model of Mild Traumatic Brain Injury Using Focal Primary Overpressure Blast to the Cranium in Mice.,” *Journal of Neurotrauma*, vol. 33, no. 4, pp. 403–22, Feb. 2016.

[117] J. DeMar, K. Sharrow, M. Hill, J. Berman, T. Oliver, and J. Long, “Effects of Primary Blast Overpressure on Retina and Optic Tract in Rats.,” *Frontiers in Neurology*, vol. 7, p. 59, 2016.

[118] P. B. L. Pun *et al.*, “Low level primary blast injury in rodent brain.,” *Frontiers in Neurology*, vol. 2, p. 19, 2011.

[119] J. M. Gee *et al.*, “Imaging activity in neurons and glia with a Polr2a-based and cre-dependent GCaMP5G-IRES-tdTomato reporter mouse.,” *Neuron*, vol. 83, no. 5, pp. 1058–72, Sep. 2014.

[120] W. E. Allen *et al.*, “Global Representations of Goal-Directed Behavior in Distinct Cell Types of Mouse Neocortex.,” *Neuron*, vol. 94, no. 4, p. 891–907.e6, May 2017.

[121] G. Cui *et al.*, “Concurrent activation of striatal direct and indirect pathways during action initiation.,” *Nature*, vol. 494, no. 7436, pp. 238–42, Feb. 2013.

[122] S. B. Hofer *et al.*, “Differential connectivity and response dynamics of excitatory and inhibitory neurons in visual cortex.,” *Nature Neuroscience*, vol. 14, no. 8, pp. 1045–52, Jul. 2011.

[123] J. B. Issa, B. D. Haeffele, A. Agarwal, D. E. Bergles, E. D. Young, and D. T. Yue, “Multiscale optical Ca2+ imaging of tonal organization in mouse auditory cortex.,” *Neuron*, vol. 83, no. 4, pp. 944–59, Aug. 2014.

[124] B. B. Scott, C. D. Brody, and D. W. Tank, “Cellular resolution functional imaging in behaving rats using voluntary head restraint.,” *Neuron*, vol. 80, no. 2, pp. 371–84, Oct. 2013.

[125] R. Homma *et al.*, “Wide-field and two-photon imaging of brain activity with voltage- and calcium-sensitive dyes.,” *Methods in Molecular Biology*, vol. 489, pp. 43–79, 2009.

[126] H. Yan, Y. Feng, and Q. Wang, “Altered Effective Connectivity of Hippocampus-Dependent Episodic Memory Network in mTBI Survivors.,” *Neural Plasticity*, vol. 2016, p. 6353845, 2016.

[127] J. A. Hartings *et al.*, “Spreading depolarizations and late secondary insults after traumatic brain injury.,” *Journal of Neurotrauma*, vol. 26, no. 11, pp. 1857–66, Nov. 2009.

[128] L. S. Deshpande *et al.*, “Alterations in neuronal calcium levels are associated with cognitive deficits after traumatic brain injury.,” *Neuroscience Letters*, vol. 441, no. 1, pp. 115–9, Aug. 2008.

[129] D. A. Sun *et al.*, “Traumatic brain injury causes a long-lasting calcium (Ca2+)-plateau of elevated intracellular Ca levels and altered Ca2+ homeostatic mechanisms in hippocampal neurons surviving brain injury.,” *The European Journal of Neuroscience*, vol. 27, no. 7, pp. 1659–72, Apr. 2008.

[130] M. Hemphill, T. Shanti, and D. Meaney, “In vivo calcium imaging of hippocampal ca1 neurons reveals a functional injury signature of primary blast neurotrauma.,” in *35th Annual National Neurotrauma Symposium*, 2017, vol. 34, no. 13, pp. T01-05.

[131] K. Sam, T. Srnak, and P. Sengupta, “Low-force mechanical perturbations altered calcium dynamics in networks of GCaMP6s expressing cortical neurons.,” *Biophysical Journal*, vol. 112, no. 3, p. 159a, 2017.

[132] M.-C. Ding, Q. Wang, E. H. Lo, and G. B. Stanley, “Cortical excitation and inhibition following focal traumatic brain injury.,” *The Journal of Neuroscience*, vol. 31, no. 40, pp. 14085–94, Oct. 2011.

[133] J. D. Bell, E. Park, J. Ai, and A. J. Baker, “PICK1-mediated GluR2 endocytosis contributes to cellular injury after neuronal trauma.,” *Cell Death and Differentiation*, vol. 16, no. 12, pp. 1665–80, Dec. 2009.

[134] J. M. Spaethling, D. M. Klein, P. Singh, and D. F. Meaney, “Calcium-permeable AMPA receptors appear in cortical neurons after traumatic mechanical injury and contribute to neuronal fate.,” *Journal of Neurotrauma*, vol. 25, no. 10, pp. 1207–16, Oct. 2008.

[135] J. Schumann, G. A. Alexandrovich, A. Biegon, and R. Yaka, “Inhibition of NR2B phosphorylation restores alterations in NMDA receptor expression and improves functional recovery following traumatic brain injury in mice.,” *Journal of Neurotrauma*, vol. 25, no. 8, pp. 945–57, Aug. 2008.

[136] A. Biegon, P. A. Fry, C. M. Paden, A. Alexandrovich, J. Tsenter, and E. Shohami, “Dynamic changes in N-methyl-D-aspartate receptors after closed head injury in mice: Implications for treatment of neurological and cognitive deficits.,” *Proceedings of the National Academy of Sciences of the United States of America*, vol. 101, no. 14, pp. 5117–22, Apr. 2004.

[137] B. M. Witgen *et al.*, “Regional hippocampal alteration associated with cognitive deficit following experimental brain injury: a systems, network and cellular evaluation.,” *Neuroscience*, vol. 133, no. 1, pp. 1–15, 2005.

[138] C.-Q. Kao, P. B. Goforth, E. F. Ellis, and L. S. Satin, “Potentiation of GABA(A) currents after mechanical injury of cortical neurons.,” *Journal of Neurotrauma*, vol. 21, no. 3, pp. 259–70, Mar. 2004.

[139] R. Ravin *et al.*, “Blast shockwaves propagate Ca(2+) activity via purinergic astrocyte networks in human central nervous system cells.,” *Scientific Reports*, vol. 6, p. 25713, 2016.

[140] J. T. Weber, “Altered calcium signaling following traumatic brain injury.,” *Frontiers in Pharmacology*, vol. 3, p. 60, 2012.

[141] L. Wang, T. L. Hagemann, H. Kalwa, T. Michel, A. Messing, and M. B. Feany, “Nitric oxide mediates glial-induced neurodegeneration in Alexander disease.,” *Nature Communications*, vol. 6, p. 8966, Nov. 2015.

[142] M. T. Huuskonen *et al.*, “The Copper bis(thiosemicarbazone) Complex CuII(atsm) Is Protective Against Cerebral Ischemia Through Modulation of the Inflammatory Milieu.,” *Neurotherapeutics*, vol. 14, no. 2, pp. 519–532, 2017.

[143] C. C. Chiu *et al.*, “Trial Outcome and Associative Learning Signals in the Monkey Hippocampus,” *Neuron*, vol. 61, no. 6, pp. 930–940, 2009.

[144] L. E. Jarrard, “On the role of the hippocampus in learning and memory in the rat.,” *Behavioral and Neural Biology*, vol. 60, no. 1, pp. 9–26, Jul. 1993.

[145] K. L. Brown, D. M. Comalli, M. De Biasi, and D. S. Woodruff-Pak, “Trace Eyeblink Conditioning is Impaired in α7 but not in β2 Nicotinic Acetylcholine Receptor Knockout Mice,” *Frontiers in Behavioral Neuroscience*, vol. 4, no. October, p. 166, 2010.

[146] J. F. Disterhoft, M. Kronforst-Collins, M. M. Oh, J. M. Power, A. R. Preston, and C. Weiss, “Cholinergic Facilitation of Trace Eyeblink Conditioning in Aging Rabbits,” *Life Sciences*, vol. 64, no. 6–7, pp. 541–548, 1999.

[147] Á. Fontán-Lozano, J. Troncoso, A. Múnera, Á. M. Carrión, and J. M. Delgado-García, “Cholinergic septo-hippocampal innervation is required for trace eyeblink classical conditioning,” *Learning and Memory*, vol. 12, no. 6, pp. 557–563, 2005.

[148] S. Kawahara, M. Mishina, Y. Kirino, T. Sakamoto, K. Takatsuki, and H. Niki, “Role of hippocampal NMDA receptors in trace eyeblink conditioning,” *Brain Research*, vol. 1039, no. 1–2, pp. 130–136, 2005.

[149] S. Lissek, A. Golisch, B. Glaubitz, and M. Tegenthoff, “The GABAergic system in prefrontal cortex and hippocampus modulates context-related extinction learning and renewal in humans,” *Brain Imaging and Behavior*, vol. 11, no. 6, pp. 1885–1900, 2017.

[150] B. J. Catlow, S. Song, D. A. Paredes, C. L. Kirstein, and J. Sanchez-Ramos, "Effects of psilocybin on hippocampal neurogenesis and extinction of trace fear conditioning," *Experimental Brain Research*, vol. 228, no. 4, pp. 481–491, 2013.

[151] C. Herry, S. Ciocchi, V. Senn, L. Demmou, C. Müller, and A. Lüthi, "Switching on and off fear by distinct neuronal circuits.," *Nature*, vol. 454, no. 7204, pp. 600–6, Jul. 2008.

[152] N. C. Tronson *et al.*, "Segregated populations of hippocampal principal CA1 neurons mediating conditioning and extinction of contextual fear.," *The Journal of Neuroscience*, vol. 29, no. 11, pp. 3387–94, Mar. 2009.

[153] K. R. Hansen *et al.*, "Mild Blast Injury Produces Acute Changes in Basal Intracellular Calcium Levels and Activity Patterns in Mouse Hippocampal Neurons," *Journal of Neurotrauma*, vol. 35, no. 13, pp. 1523–1536, 2018.

[154] J. Schindelin *et al.*, "Fiji: an open-source platform for biological-image analysis.," *Nature Methods*, vol. 9, no. 7, pp. 676–82, Jun. 2012.

[155] D. Legland, I. Arganda-Carreras, and P. Andrey, "MorphoLibJ: integrated library and plugins for mathematical morphology with ImageJ.," *Bioinformatics*, vol. 32, no. 22, pp. 3532–3534, 2016.

[156] T. W. Berger, P. C. Rinaldi, D. J. Weisz, and R. F. Thompson, "Single-unit analysis of different hippocampal cell types during classical conditioning of rabbit nictitating membrane response.," *Journal of Neurophysiology*, vol. 50, no. 5, pp. 1197–219, Nov. 1983.

[157] J. T. Green and J. D. Arenos, "Hippocampal and cerebellar single-unit activity during delay and trace eyeblink conditioning in the rat.," *Neurobiology of Learning and Memory*, vol. 87, no. 2, pp. 269–84, Feb. 2007.

[158] E. Acquas, C. Wilson, and H. C. Fibiger, "Conditioned and unconditioned stimuli increase frontal cortical and hippocampal acetylcholine release: effects of novelty, habituation, and fear.," *The Journal of Neuroscience*, vol. 16, no. 9, pp. 3089–96, May 1996.

[159] C. Chang, J. D. Berke, and S. Maren, "Single-unit activity in the medial prefrontal cortex during immediate and delayed extinction of fear in rats.," *PLoS One*, vol. 5, no. 8, p. e11971, Aug. 2010.

[160] D. R. Euston, A. J. Gruber, and B. L. McNaughton, "The role of medial prefrontal cortex in memory and decision making.," *Neuron*, vol. 76, no. 6, pp. 1057–70, Dec. 2012.

[161] D. Tse *et al.*, “Schemas and memory consolidation.,” *Science*, vol. 316, no. 5821, pp. 76–82, Apr. 2007.

[162] S. McKenzie, N. T. M. Robinson, L. Herrera, J. C. Churchill, and H. Eichenbaum, “Learning causes reorganization of neuronal firing patterns to represent related experiences within a hippocampal schema.,” *The Journal of Neuroscience*, vol. 33, no. 25, pp. 10243–56, Jun. 2013.

[163] H. J. Gritton *et al.*, “Unique contributions of parvalbumin and cholinergic interneurons in organizing striatal networks during movement.,” *Nature Neuroscience*, Feb. 2019.

[164] F. Pedregosa *et al.*, “Scikit-learn: Machine Learning in Python,” *Journal of Machine Learning Research*, vol. 12, pp. 2825–2830, 2011.

[165] J. T. Vogelstein, B. O. Watson, A. M. Packer, R. Yuste, B. Jedynak, and L. Paninskik, “Spike inference from calcium imaging using sequential Monte Carlo methods,” *Biophysical Journal*, vol. 97, no. 2, pp. 636–655, 2009.

CURRICULUM VITAE

[redacted]

[redacted]

[redacted]

[redacted]